Evaluation of Radiation Induced Segregation in Fe-Ni-Cr Alloys

by

Carlos D. Flores
Ensign, USN

B.S., Electrical Engineering
United States Naval Academy, 1992

Submitted to the Department of Nuclear Engineering and
the Department of Materials Science and Engineering
in Partial Fulfillment of the Requirements for the Degrees of

Master of Science in Nuclear Engineering
and
Master of Science in Materials Science

at the
Massachusetts Institute of Technology
May 1994

Signature of Author _____
Department of Nuclear Engineering
Department of Materials Science and Engineering
May , 1994

Certified by _____
Ronald G. Ballinger, Sc.D.
Professor of Nuclear Engineering and Materials Science and Engineering
Thesis Supervisor

Certified by _____
Otto K. Harling, Ph.D.
Director, Nuclear Reactor Laboratory
Thesis Reader.

Accepted by _____
Allan F Henry, Ph.D.
Chair, Nuclear Engineering Departmental Committee on Graduate Students

Accepted by _____
Carl V. Thompson II
Professor of Electronic Materials
Chair, Departmental Committee on Graduate Students

Evaluation of Radiation Induced Segregation in Fe-Ni-Cr Alloys

by

Carlos D. Flores

Submitted to the Department of Nuclear Engineering and the Department of Materials Science and Engineering on May 6, 1994 in partial fulfillment of the requirements for the Degrees of Master of Science in Nuclear Engineering and Master of Science in Materials Science

Abstract

Irradiation assisted stress corrosion cracking (IASCC) is a relatively recent phenomenon causing great concern in the nulear community. Due to the effects that it could have in nuclear power plants already in operation, this complicated phenomenon has been the subject of research since speculation of its existence in the 1960's . Field data already shows that exposure of austenitic stainless steels to fast neutron and gamma radiation in light water reactors (LWR's) causes increased occurrences of intergranular cracking. Mechanisms that IASCC operates by such as radiation induced segregation (RIS) are still not completely understood, but much research is being done to quantify them in hopes of finding a way to prevent occurrences of IASCC.

Several experimental Fe-Ni-Cr austenitic alloys with varying compositions of nickel and chromium have been irradiated at the MIT Nuclear Reactor Laboratory for the purpose of studying radiation induced segregation. Through STEM-EDX analysis, compositional profiles of grain boundaries in these model alloys were compiled and contrasted. It is apparent that alloys with high nickel concentrations and high chromium concentrations have both enhanced nickel enrichment and enhanced chromium depletion. Alloy N9 (50Ni-26Cr-Fe bal. in wt%) irradiated to 0.8dpa had an average of 13wt% nickel enrichment and a 7wt% chromium depletion at the grain boundary.

These model alloy grain boundary profiles were also compared to a theoretical model for neutron-irradiation induced segregation. This model was adjusted through the use of a parameter which accounts for grain boundary structure. In this fashion matching profiles of the experimental data were obtained, and the RIS computer code was validated. Through these comparisons, the dominance of grain boundary orientation was postulated.

Electrochemical potentiokinetic reactivation (EPR) testing was also performed on both irradiated and unirradiated versions of the model alloys. Comparison of results leads one to the conclusion of enhanced chromium depletion with increasing nickel concentration.

Thesis Supervisor: Dr. Ronald G. Ballinger
Title: Professor of Nuclear Engineering and Materials Science and Engineering

Acknowledgments

As a native TEXAN, and proud of it, I have the tendency to think BIG. In this respect, I extend a big, "**THANK YA'LL!**" to everyone involved in the completion of my two year stay here in the Boston area. Although they say that "home is where the heart is", and in my case this is Texas, everyone here has made Boston my home away from home. For this I am truly grateful. Although I complained at every possible moment about the New England area; from too much snow, to not enough parking, to too much traffic, I am going to miss it. Not the things I complained about, mind you, those I will not miss, but I will definitely miss the people.

Some of these people provided immeasurable support and assistance for my research and completion of this thesis. I must first thank Prof. Ron Ballinger for his mentorship in his inimitable naval manner. I would also like to thank Prof. Otto Harling for his guidance of my research. Both provided the support without which this would not have been possible.

At the M.I.T. Nuclear Reactor Laboratory there were many others that also need to be mentioned and thanked. Dr. Gordon Kohse (Kanukes Team Leader), Mr. Pete Stahle, and Mr. Ernesto Cabello, all provided their time and knowledge with extreme patience every time I was learning something new. To Jeff O'Donnell, thanks for heading up the IASCC gang and officing with me, and good luck in Houston. Although you're not a native Texan, I'm sure they will soon deem you an honorary one. Thanks also to Theodore J. Weber and Julian Guerra de la Torre for all their supreme technical support.

The assistance of the NRL machine shop was also much appreciated, so many thanks to Mr. Yakov Ostrovsky, Ronny St. Jean, and Johnny Wasik.

Thanks also to RRPO: Fred McWilliams, Todd Date, Marcia Austin, and Bruce Graber. The term "particle-man" now has a whole new meaning to me.

On the other side of the road, I would like to thank Martin Morra, Hiu Au, John Murphy, Henri Tsukahara, John Chun, and especially Alexis Lewis. They all taught me something new almost every day I was in lab, and were always willing to share their time. Alexis, many thanks to you for all the etching, polishing, and x-ray diffraction work. I would never have had enough time on my own. Also, many thanks are extended to Dr. Yutaka Watanabe. His competence is unsurpassed, and I consider it an honor to have worked with him. Yutaka, you would have made a fine naval officer.

Thanks also have to be given to the organizations which made this possible. Thanks to the Tokyo Electric Power Company and the Electric Power Research Institute for funding and guidance. Thanks also to the United States Navy for this opportunity to go to graduate school, and thanks to the professors at the U.S. Naval Academy who urged me to go and wrote the letters of recommendation. Thanks also to the National Science Foundation for the funding which provided for my tuition.

A Hilaire Mansoux (et sa famille), pour lesquels aucun mots ne sauraient exprimer la gratitude éprouvée envers l'aide et l'amitié que vous m'avez porté au cours de cette année. Tout ce que je puis dire, est: "Puisse le Seigneur vous bénir, et se faire qu'un jour vous veniez me rendre visite au Texas, chez moi (pour une bonne raison)".

Table of contents

List of Figures

List of Tables

Chapter 1

1. Introduction

Irradiation-assisted stress-corrosion cracking (IASCC) is the premature cracking of material in an aggressive environment system exposed to ionizing radiation. [1] IASCC can result from effects on materials due to gamma irradiation, neutrons, electrons, or ions. In a practical sense, however, the problem is mainly concerned with accelerated intergranular cracking in austenitic alloys in light-water nuclear reactor cores. This is caused by fast neutron damage to the material in the aggressive environment which is created in part by fast neutron and gamma radiation. Because of its adverse effects on in-core structural components, and hence system reliability, it is important for IASCC to be studied and modeled. [2]

Although initially viewed as a completely independent phenomena, IASCC is now seen as an accelerant of the environmental cracking process, Stress Corrosion Cracking (SCC). The enhancement effects that irradiation causes are illustrated in Figure 1.1. Enhancement of SCC susceptibility by certain types of radiation is due to the effect of radiation on microstructure and aqueous chemistry. One of these microstructural effects is known as Radiation Induced Segregation (RIS) and has been the focus of much research related to IASCC. [3] One cannot fully appreciate the complexities of IASCC, however, without a basic understanding of SCC and RIS.

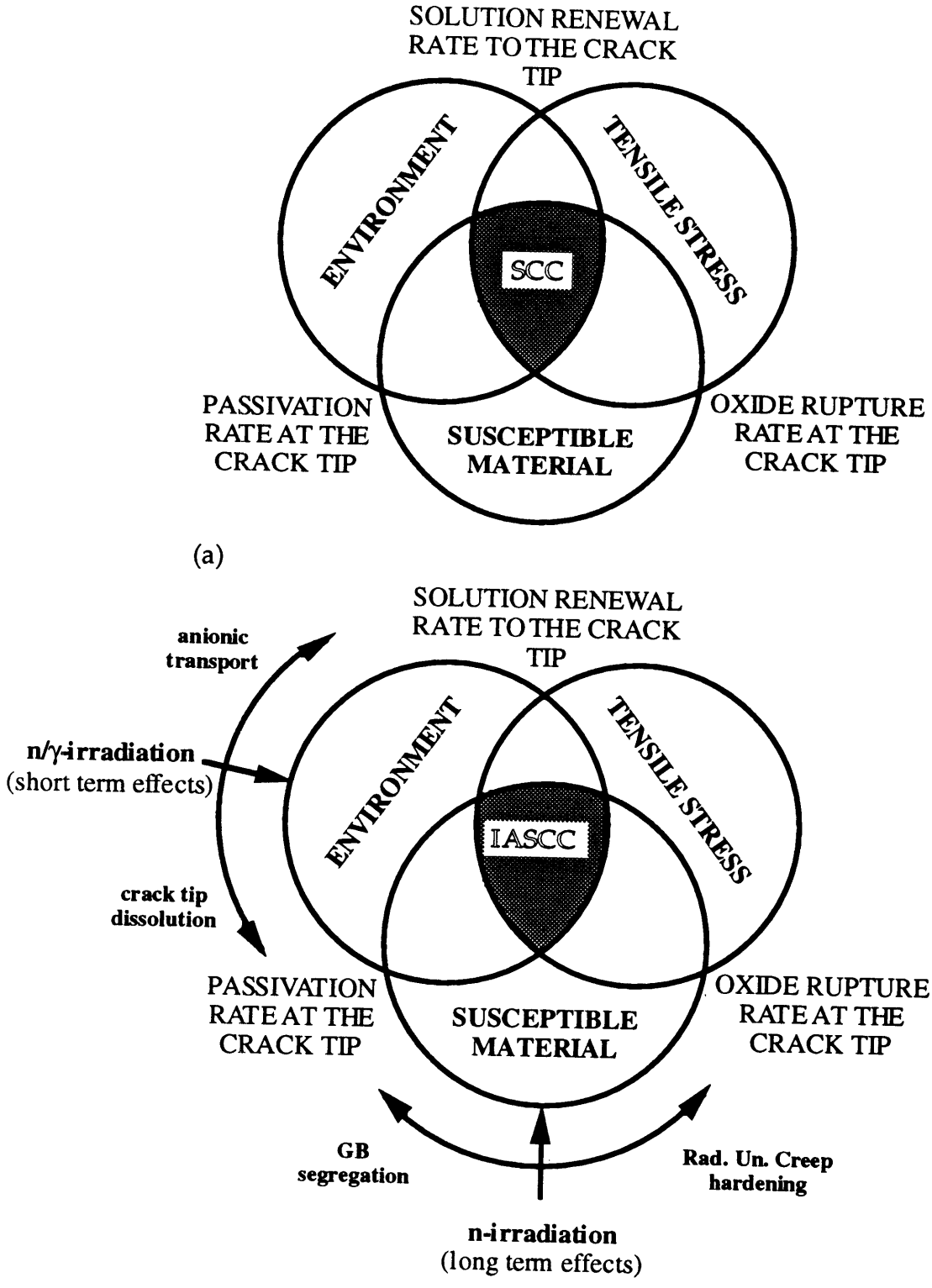

Figure 1.1 (a and b): a) Venn Diagram showing the phenomenological factors required for SCC. b)Effects of radiation on SCC. [4]

1.1. STRESS CORROSION CRACKING

Stress Corrosion Cracking (SCC) is a term used to describe failures in engineering materials that occur by environmentally induced crack initiation and propagation. [5] For SCC to occur, the system must meet three basic requirements which are illustrated in Figure 1.1(a) and described as follows:

1. Susceptible Material: Factors such as grain boundary chemistry and microstructure.

2. Tensile Stress: The surfaces of the components in the given environment have to be loaded in tension.

3. Aggressive Environment: A very specific environment is required for SCC to occur for any given material. This environment provides for an electrochemical process resulting in the release of metal ions, the result being the localized dissolution of the metal. [6]

As clearly depicted in Figure 1.1, SCC is not a result of any of these factors acting independently, but rather, conjointly. Although stress may be applied at corrosion-generated surface faults, it is not necessary for K_{crit} (a materials characteristic relating crack length to the required fracture stress) to be exceeded for mechanical fracture to occur, as would be normal for an inert environment, but rather, K_{scc} (the relation between crack length and and required fracture stress during an instance of SCC) is less than K_{crit}. Also, if pre-corrosion occurs and then a load is applied, crack propagation by SCC will

not occur. SCC is a result of a combined mechanical and chemical crack propagation process which has been termed "synergistic". [7]

Grain boundary chemistry is another key factor in determining the susceptibility of materials to SCC. For austenitic stainless steels (which usually contain 18% Cr for corrosion resistance), chromium carbides ($Cr_{23}C_6$) will precipitate at the grain boundary in weld heat affected zones. As a result, there is a localized depletion of chromium near these grain boundaries, and the material is said to be sensitized. [8] Chromium depletion results in the grain boundary region losing corrosion resistance. It becomes anodic while the chromium-precipitates and the bulk of the material act as cathodes in a rapid electro-chemical dissolution of the material as illustrated in Figure 1.2. Deep penetration of the corrosive medium can also take place. [9]

Many mechanisms have been proposed to explain how SCC occurs, but they can generally be divided into two categories; dissolution models which propose that crack propagation proceeds by anodic dissolution at the crack tip, and models which propose that crack propagation occurs mainly due to mechanical processes. [10] A summary of these mechanisms is as follows:

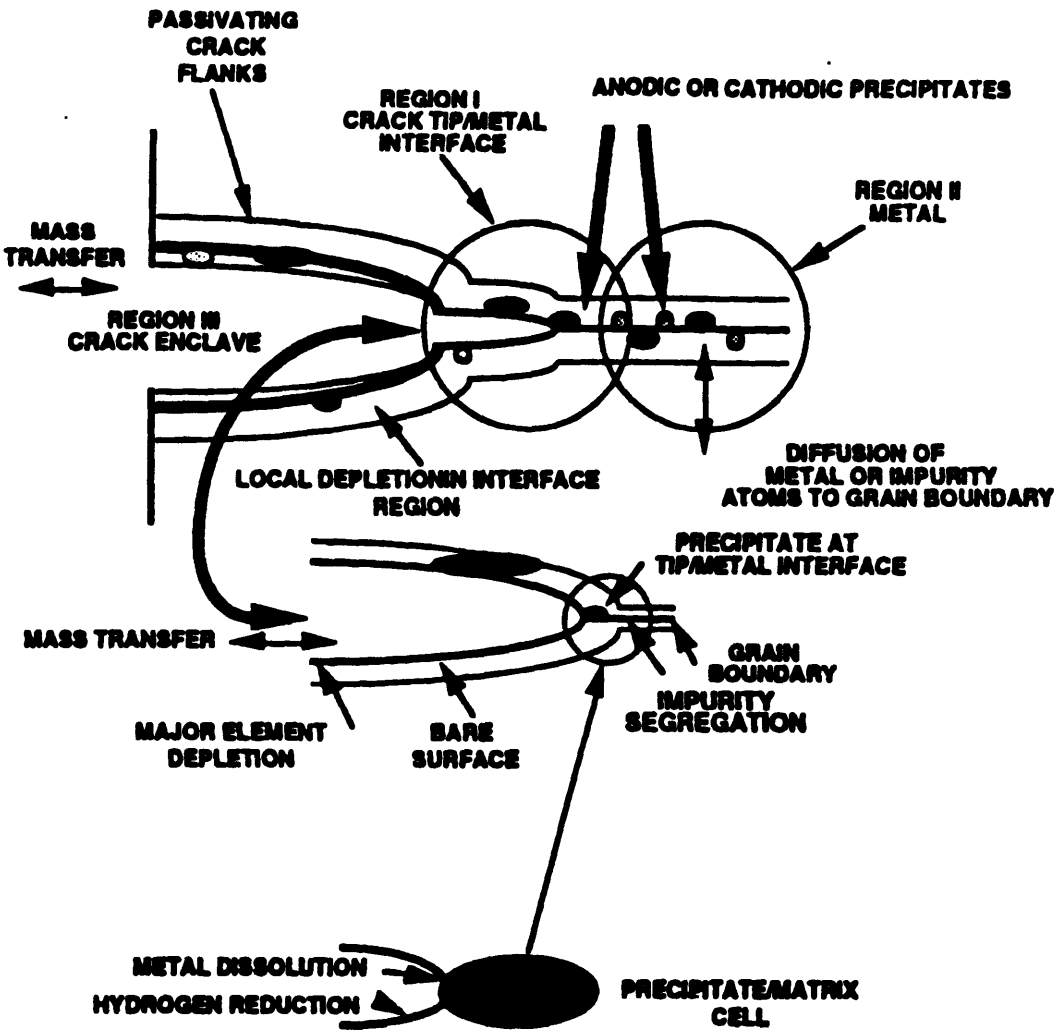

Figure 1.2: General overview of environmentally assisted cracking. [11]

1. The mechano-chemical model proposed by Hoar and Hines [12] relates crack propagation to the dissolution of film-free metal due to an increase in active sites caused by plastic deformation at the crack tip.

2. The film-rupture or slip step dissolution model first proposed by Champion [13] and Logan [14] agrees that dislocations at the crack tip of passivated metal surfaces promote localized dissolution, thus causing corrosion that leads to crack propagation.

3. Forty [15] first described a crack propagation mechanism due to repeated rupture and formation of a brittle film growing into the crack tip.

4. Petch [16] and Uhlig [17] together proposed a stress sorption means of crack propagation: the surface energy required to form a crack is reduced by the aggressive environment, thus reducing fracture stress.

5. Crack propagation due to combinations of the above. [18]

All mechanisms have in common, however, two requirements for SCC to occur. The first is that the corrosion process has to be electrochemically possible; the metal has to become an active anode of an electrolytic cell. The second requirement is that the rate of corrosion has to be within the proper range to allow a passive layer to form on the newly exposed metal surface immediately behind the propagating crack tip. The reasons for this are two-fold. First, this ensures that the tip of the crack remains the most active (or most anodic) part of the region, and second, the current density at the crack remains orders of magnitude higher than at the crack walls. These conditions ensure that the tip of the crack dissolves preferentially, thus ensuring crack propagation (no blunting of the crack tip) and not a reversion

to some other type of corrosion. [19] Figure 1.3 is an Evans diagram that shows the active-passive anodic behavior of a material that satisfies the requirements for SCC to occur. This figure illustrates the effects to the anodic curves due to the loss of chromium at the grain boundaries. It illustrates just how drastically this can affect the corrosion rate.

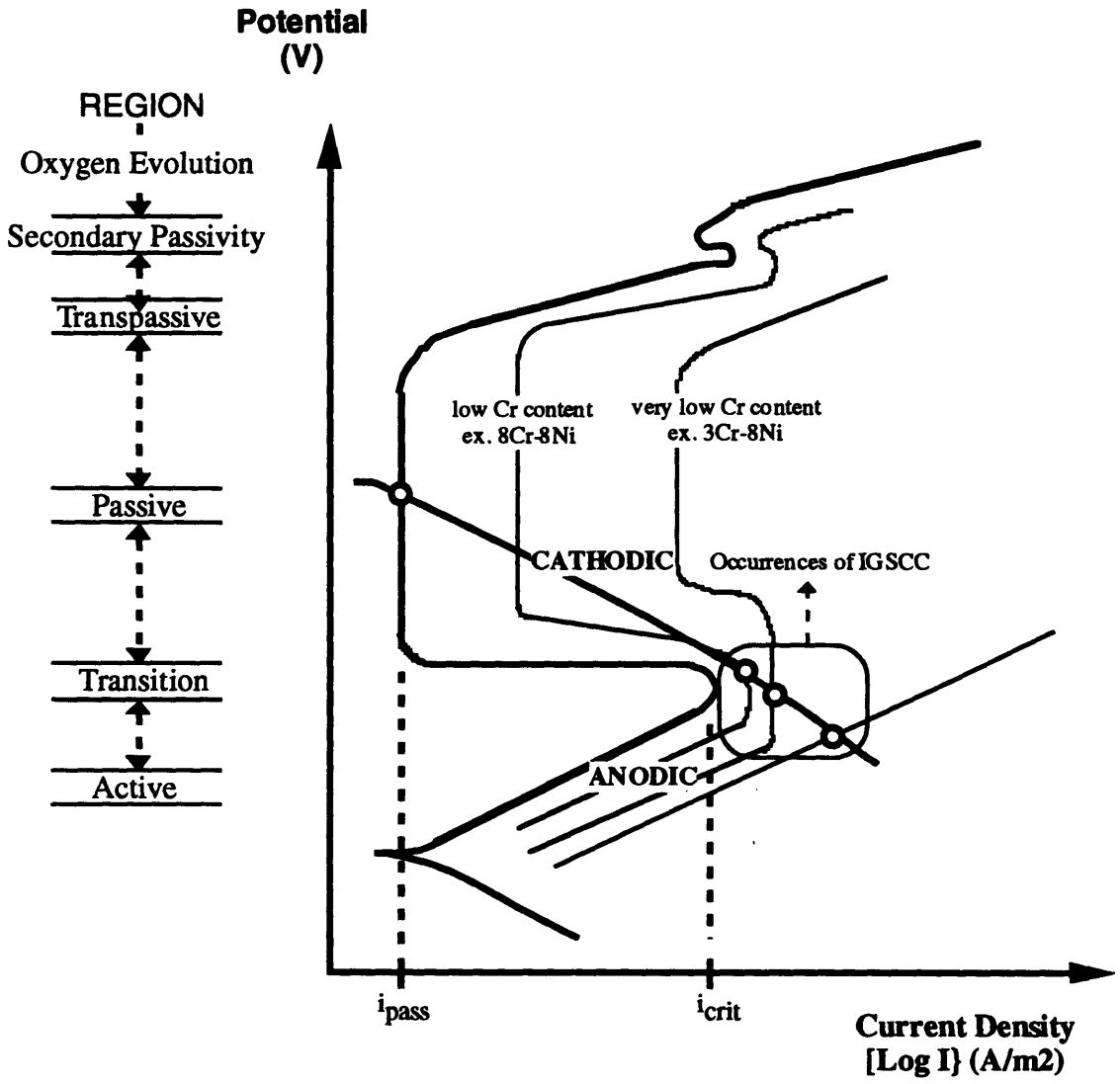

Figure 1.3: Simplified schematics of Ni-Cr-Fe materials showing activation and passivation anodic polarization behavior, and a single cathodic curve representing the environment. [20]

With a basic understanding of SCC, one can now ask the question of how external factors such as radiation might affect, add to, or change the

processes by which SCC occurs. The answer to these questions is summed up in the term "Irradiation-Assisted Stress-Corrosion Cracking".

1.2. IASCC SERVICE HISTORY

Instances of IASCC were first reported in the early 1960's. Despite the precautionary measures taken, including the use of non-sensitized stainless steels in-core materials, intergranular stress corrosion cracking (IGSCC) of several stainless steel components has been reported for many different types of light-water reactors (LWR's) as ahown in Table 1.1.

A summary of field service history is as follows[21]:

1. All cracking was intergranular and initiated at contact points with the water environment, and crack branching was observed. Post-irradiation tests in a dry environment found only ductile, transgranular cracking.

2. No grain boundary chromium-carbide precipitates were found.

3. There existed a definite correspondence between time to failure and stress level. Failure was first noted to occur in fuel rods with thin cladding where swelling strains were the highest.

4. A higher incidence of cracking existed in the areas of peak heat flux which also correspond to the areas of greatest fuel-cladding interaction and stress and strain.

5. Fewer reports of intergranular cracking in PWR's occurred, and at the time these incidents were believed to be the result of off-chemistry conditions or stress rupture. In retrospect, however, IASCC is the likely mechanism by which these failures occurred. Hydrogen over-pressure and the resulting lower corrosion potential could possibly be off-set by the higher temperatures.

Table 1.1: IASCC Service Experience [22]

Component	Material	Reactor	Sources of Stress
Fuel Cladding	304 SS	BWR	Fuel Swelling
Fuel Cladding	304 SS	PWR	Fuel Swelling
Fuel Cladding	20%Cr/25% Ni/Nb	AGR	Fuel Swelling
Fuel Cladding Ferrules	20%Cr/25% Ni/Nb	SGHWR	Fabrication
Neutron Source Holders	304 SS	BWR	Welding & Be Swelling
Instrument Dry Tubes	304 SS	BWR	Fabrication
Control Rod Absorber Tubes	304 SS	BWR	B_4C Swelling
Fuel Bundle Cap Screws	304 SS	BWR	Fabrication
Control Rod Follower Rivets	304 SS	BWR	Fabrication
Control Blade Handle	304 SS	BWR	Low Stress
Control Blade Sheath	304 SS	BWR	Low Stress
Plate Type Control Blade	304 SS	BWR	Low Stress
Various Bolts*	A-286	PWR & BWR	Service
Steam Separator Dryer Bolts*	A-286	BWR	Service
Shroud Head Bolts*	600	BWR	Service
Various Bolts	X-750	BWR & PWR	Service
Guide Tube Support Pins	X-750	PWR	Service
Jet Pump Beams*	X-750	BWR	Service
Various Springs	X-750	BWR & PWR	Service
Various Springs	718	PWR	Service

* Cracking of Core Internal Occurs Away from High Neutron and Gamma Fluxes

The above summary and Table 1.1 show that Type 304 stainless steels suffered extensive cracking, especially in its use as a fuel cladding which is subject to high stresses. Because of this it was subsequently replaced with Zircaloy-2. [23] The cracking suffered by the 304 stainless steel was also the first sign that annealed type stainless steel could suffer from IASCC in a BWR environment. [24]

In more recent instances of IASCC, failure of lower-stress components has been noticed and are noted in Table 1.2 and Table 1.3. This leads to the conclusion that cracks may occur at lower stresses for higher fluences. [25] The major concern of IASCC, however, is not these lower stressed, replaceable parts, but such major internal components as the shroud and the top guide. [26]

Table 1.2. Summary of field IASCC experience up to 1980.

Component	Fluence (N/cm^2)	Source of Stress
Fuel Cladding	$5x10^{20}$-$2x10^{21}$	Fabrication & Fuel Cladding Interaction
Neutron Source Holders	10^{21}-10^{22}	Welding & Beryllium Swelling after Initial Crevice Attack
Control Rod Absorbers Tubes	$5x10^{20}$-$3x10^{21}$	B_4C Swelling
Fuel Bundle Cap Screws	10^{21}-10^{22} (estimated)	Fabrication and / or Assembly
Rivets in Control Rod Follower	$5x10^{20}$	Unknown

Table 1.3. Summary of post 1980 IASCC field experience.[27]

Component	Fluence (N/cm^2)	Source of Stress
Plate Type Control Blade	$2x10^{21}$	B_4C Swelling
IRM/SRM Dry Tubes	~$1x10^{22}$	Fabrication

1.3. IASCC MECHANISMS

The presence of fast neutrons and gamma radiation act to enhance the process of stress corrosion cracking by affecting two legs of the SCC triad, the material and the environment. [28] Because IASCC is primarily concerned with the intergranular cracking of irradiated regions of austenitic alloys in high-temperature water; the micro-compositional effects due to neutron-irradiation, and the change in water chemistry, due to gamma and fast

neutron irradiation, are of primary importance to the IASCC phenomenon. [29]

An aggressive environment is required for SCC occurrence. In the case of IASCC, ionizing radiation helps to create such an environment. Both neutron and gamma irradiation act to create a more aggressive environment in-core by increasing the amount of oxidizing species in the coolant through radiolysis. [30] Ionizing radiation causes the breakdown of water into many oxidizing and reducing agents (e.g. e^-_{aq}, H^+, H, H_2, O_2, OH, H_2O_2, HO_2). The concentrations of these species varies depending on decomposition and recombination rates, but is highly dependent on the radiation flux, dissolved gases, and the temperature. [31]

G-values (molecules produced per 100eV absorbed by water) define the production of the above-mentioned species with respect to the energy spectrum of the ionizing radiation. Table 1.4 shows the energy deposition due to differing types of radiation and the possible species produced.

Table 1.4: Linear energy transfer (LET) and G-values for different radiation species. [32]

Radiation Type	Radiation Mean LET, eV/nm	e_{aq}	H^+	OH	H_2	H_2O_2	H	HO_2
Fast n	40	0.93	0.93	1.09	0.88	0.99	0.5	0.04
γ	~0.01	2.7	2.7	2.86	0.43	0.61	0.61	0.03
mixed	n & γ	1.26	1.26	1.42	0.80	0.92	0.52	0.04
10 MeV H^+	13.5	1.46	1.46	1.52	0.70	0.90	0.64	0.04

Typical BWR Peak Fluxes: ~300 MRad/hr neutron, ~60 Mrad/hr gamma

Although both gamma and fast neutron radiation are contributing factors to the water chemistry in a typical LWR, the greatest effect on water chemistry is due to fast neutrons. Not only is their Linear Energy Transfer (LET) of 40eV/nm larger than that of gamma radiation (which has a LET of 0.01 eV/nm), but their typical higher fluxes (~300 MRad/h neutron as

compared to ~60 MRad/h gamma) in LWR's make them the major contributing factor to radiation water-chemistry effects. The ratio of neutron to gamma dose rate is, however, an important determinant of the net radiolysis effect. Thermal neutrons and beta particles play an insignificant role in affecting the water chemistry. [33]

The electrochemical potential is a convenient monitor of water radiolysis effects which are important to SCC. This results from the fact that the corrosion potential is a measurement gauge of the thermodynamics and the kinetics that control the electrochemical reactions resulting in corrosion. [34] The correlation between the increase in oxidants and reductants produced by radiation and the corrosion potential is shown by the Nernst equation:

$$E = E_O + (RT/nF)\ \ln(products/reactants)$$

The fore-mentioned logarithmic dependence of species' concentration on water chemistry is shown through dissolved oxygen concentrations in water. Increased dissolved oxygen concentrations typically raise the corrosion potential in a system, but its effectiveness in doing so is dependent on the temperature. Figures 1.4(a) and 1.4(b) show that there is a range of dissolved oxygen concentrations over which a large change in the corrosion potential occurs for hot water temperatures as found in a BWR. Beyond this range, however, even changes of orders of magnitude cause negligible effects on the corrosion potential. [35] If one looks at Figure 1.5 one also sees the contribution of oxidizing water chemistry to IASCC. There is clearly a strong dependence of cracking on dissolved oxygen starting at a fluence of $2x10^{21}n/cm^2$.

It is still unclear, however, if the increase in corrosion potential occurs in both the crack and the bulk environment. It was thought that the presence of radiation could raise the corrosion potential at the crack tip above that at the crack mouth through the presence of a net oxidizing environment. This was due to the fact that gammas and neutrons have a high penetrating power, allowing them to reach the crack tip, and the water is stagnant there. [36] Measurements of crack-tip potentials in growing cracks in non-irradiated, hot-water environments show that the corrosion potentials remain low, approximately -0.5 V_{she} for all bulk environment oxygen concentrations. [37] Recently, measurements have been made under irradiated conditions which show that only a negligible rise in corrosion potential at the crack-tip occurs (<0.05 V_{she}). [38] Although, the crack-tip corrosion may not be affected greatly, it is clear, however, that an increase of dissolved oxygen in the bulk, and correspondingly the corrosion potential, causes a large increase in the crack growth rate as illustrated in Figure 1.5. This potential difference is what largely controls the enhancement mechanism producing increased anion migration and altered pH at the crack-tip. [39] In essence, the radiolysis of water can increase the corrosion potential in the bulk having a great influence on the free metal surfaces, but little direct effect in cracks and crevices.

The effects due to the water chemistry are mainly concerned with the corrosion potential. In both unirradiated and irradiated cases an increase in environmental cracking kinetics is seen with an increase of the corrosion potential to a range of -100 mV_{she} to 0 mV_{she}. The presence of a constant, aggressive water chemistry is required to have great effect on the cracking rate, but cumulative radiation exposure has a lasting effect on IASCC occurrence. This is seen by an increase in the occurrence of intergranular

stress-corrosion cracking (IGSCC) in post-irradiation slow strain rate tests as illustrated in Figure 1.6. It has also been observed that, under LWR conditions, the occurrence of IASCC has a fluence threshold. This threshold dependence also leads to the conclusion that there are both "persistent" effects of radiation such as micro-compositional changes and 'in-situ' effects, such as the water chemistry involved with the occurrence of IASCC. [40]

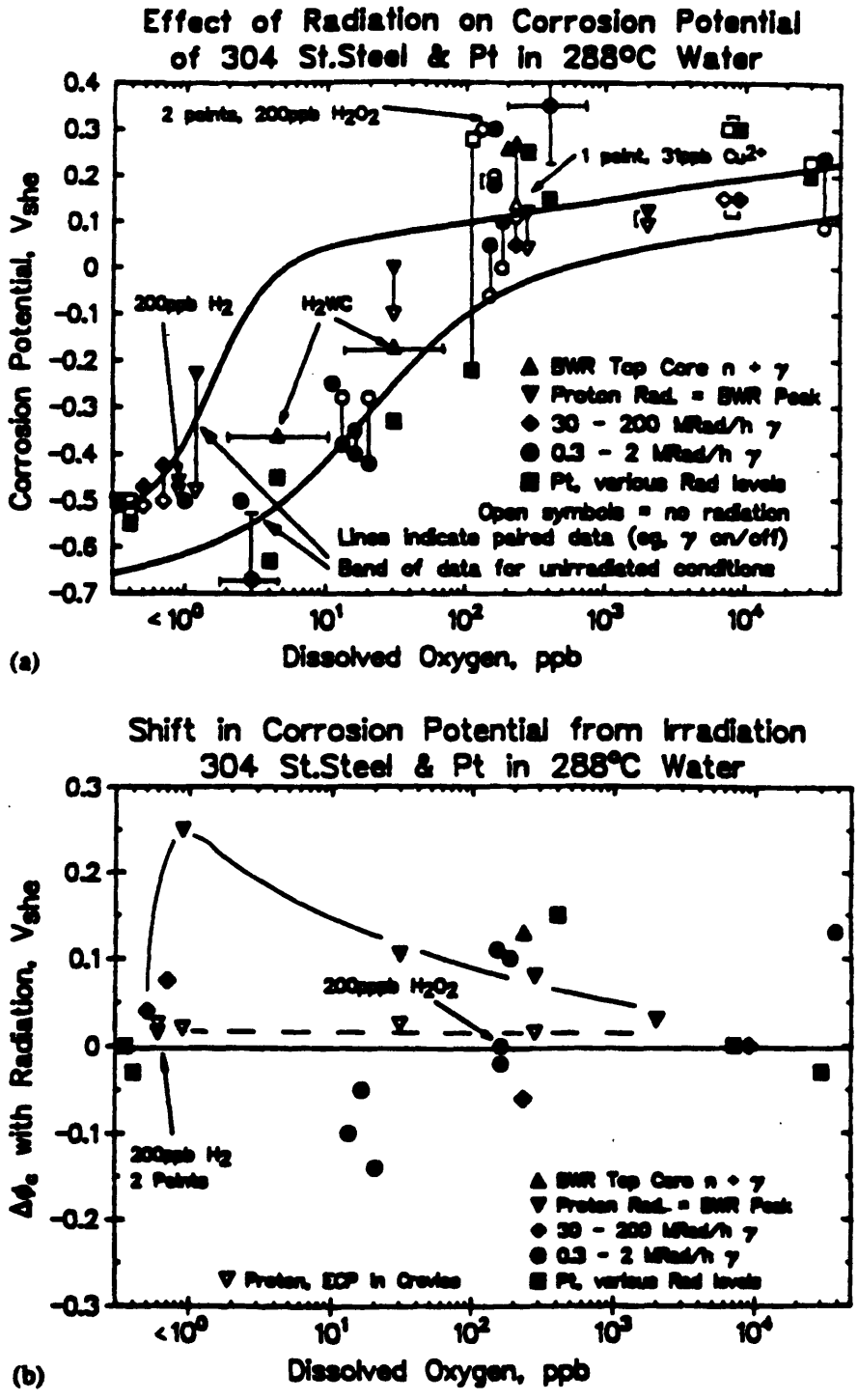

Figure 1.4: a) Effect of radiation on the corrosion potential of type 304 stainless steel in 288 C water. The curves denote the range of typical values in the unirradiated corrosion-potential data. (b) Effect of radiation on the shift in corrosion potential from the value under unirradiated conditions for type 304 stainless steel in 288 C water. [41]

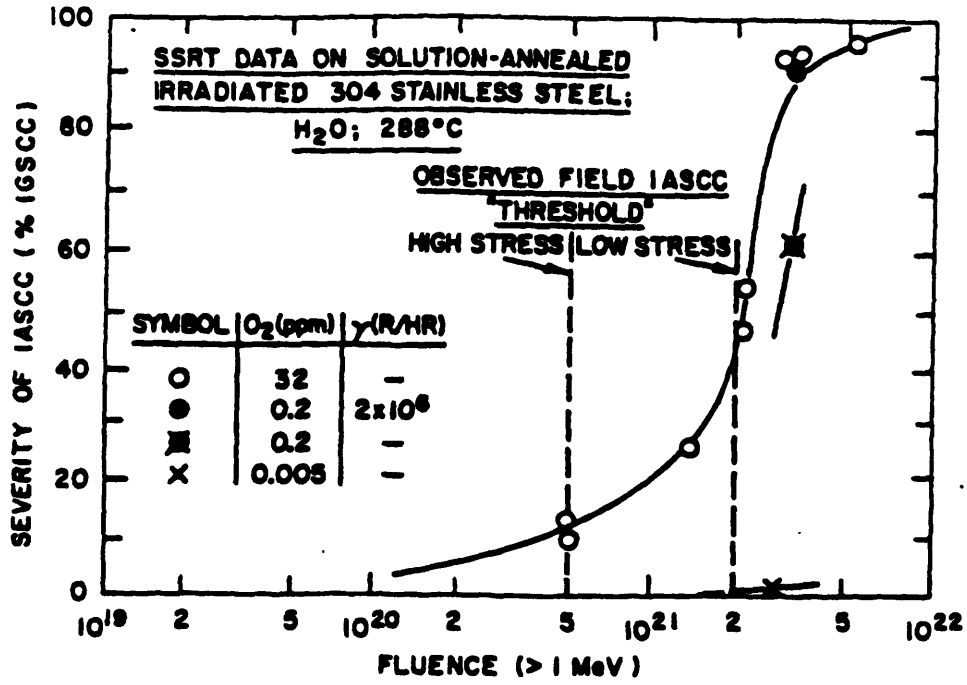

Figure 1.5: Dependence of IASCC on fast neutron fluence as measured in slow-strain-rate tests at $3.7x10^{-7}$/s on preirradiated type 304 stainless steel in 288 C water. The effect of corrosion via changes in dissolved oxygen is shown at a fluence of approximately $2x10^{21}n/cm^2$. [42]

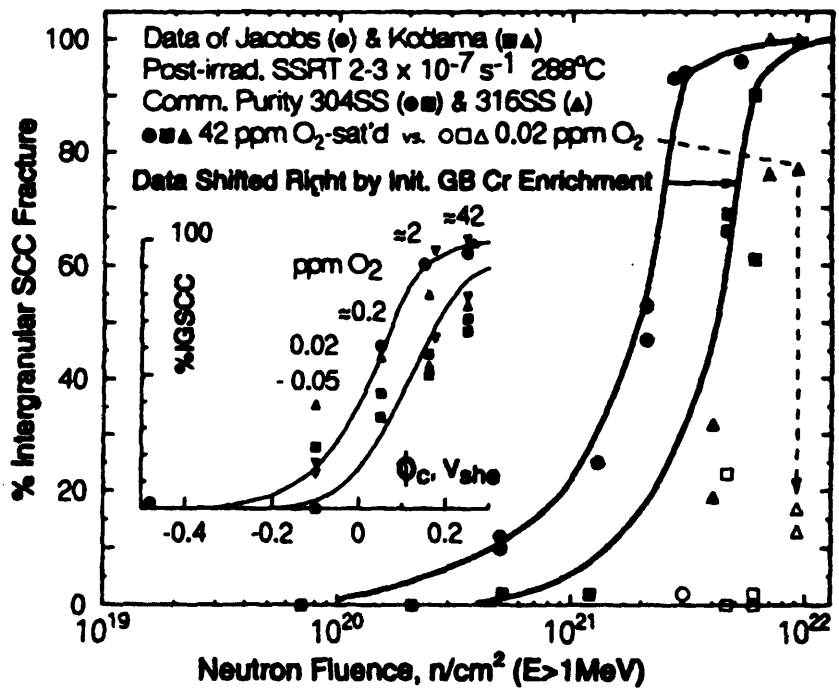

Figure 1.6: The effect of fast neutron fluence on IASCC as measured in slow strain tests on pre-irradiated types 304 and 316 stainless steels in 288 C water. In the inset figure, the effect of corrosion potential is shown for data obtained at several different fluences. [43]

Micro-compositional effects also play a key role in the occurrence of IASCC. Radiation damage to a material has the immediate result of the production of vacancy and interstitial pairs, Frenkel pairs. Concentrations and migration of these radiation produced defects varies with different conditions, but "freely migrating" defects can have long range effects on such processes as loop nucleation and growth, creep, and segregation. [44]

The effects of radiation on materials has been recognized and studied for quite some time. Intergranular cracking in fuel elements observed in-core in LWR's in the early 1960's was attributed primarily to the high stresses due to fuel swelling. Radiation hardening is also considered a material effect that aids in the occurrence of IASCC due to the accompanying increase in brittleness. Even at doses as low as 2 dpa, there is a marked reduction in material ductility corresponding to a noted decrease in fracture toughness as illustrated in Figure 1.7. Post-irradiation tensile testing has shown the result of "dislocation channeling". Deformation is confined to submicron sized shear bands while the matrix undergoes little if any deformation. Dislocation motion can be made much easier if its path is clear of radiation-damage 'debris'. If one dislocation shifts to this 'clear path' of travel, other dislocations will follow. In this manner, slip is confined to a narrow band of slip planes free from defects. This results in intense shear bands which, if confined to the grain boundary region and combined with chromuim depletion, can act so as to increase susceptibility to SCC. [45]

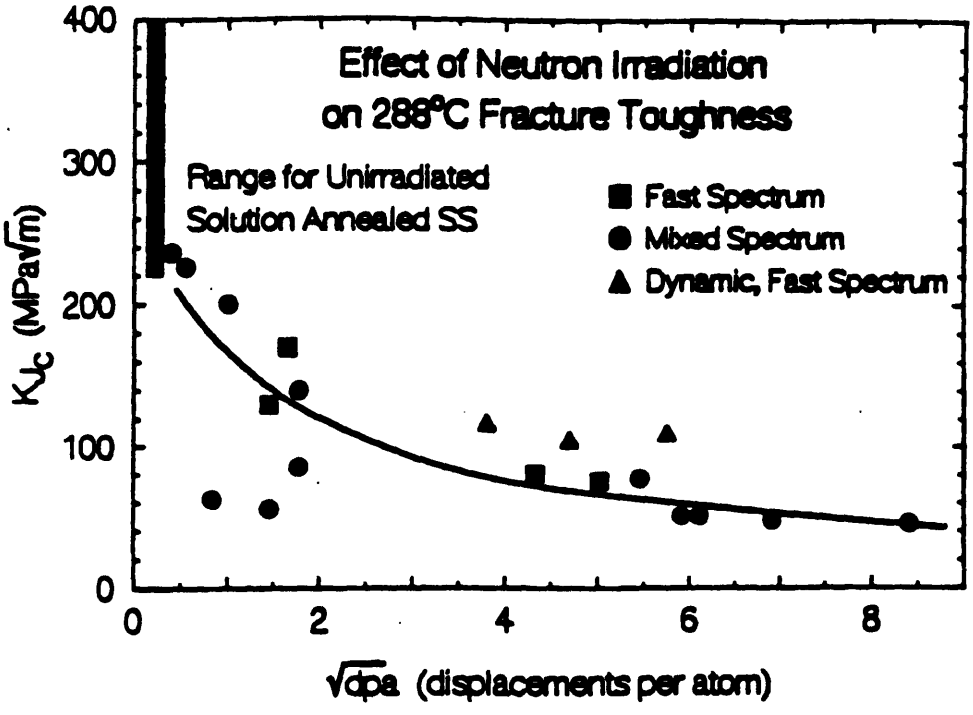

Figure 1.7: Effect of fast neutron fluence under LWR conditions on mechanical properties at 288 C of types 304 and 304L stainless steel. [46]

The occurrence of IASCC in austenitic stainless steels as a function of neutron fluence is shown in Figure 1.5 and Figure 1.8. The data shown was collected for control-blade sheath cracking in high-conductivity water in BWR's (Fig. 1.5) and for laboratory tests on pre-irradiated material (Fig. 1.8).

An obvious inference from Figure 1.8 (and also Figure 1.5) is the presence of a threshold fluence (of approximately $5x10^{20}n/cm^2$; $E_{neutron} > 1$ MeV) below which IASCC does not occur. [47] Clearly, the neutron fluence affects the material leg of the IASCC susceptibility triad. However, only relatively recently has this phenomenon been attributed in part to a process proposed theoretically by Anthony [48] in 1968 and observed in the early 1970's called radiation-induced segregation (RIS). [49]

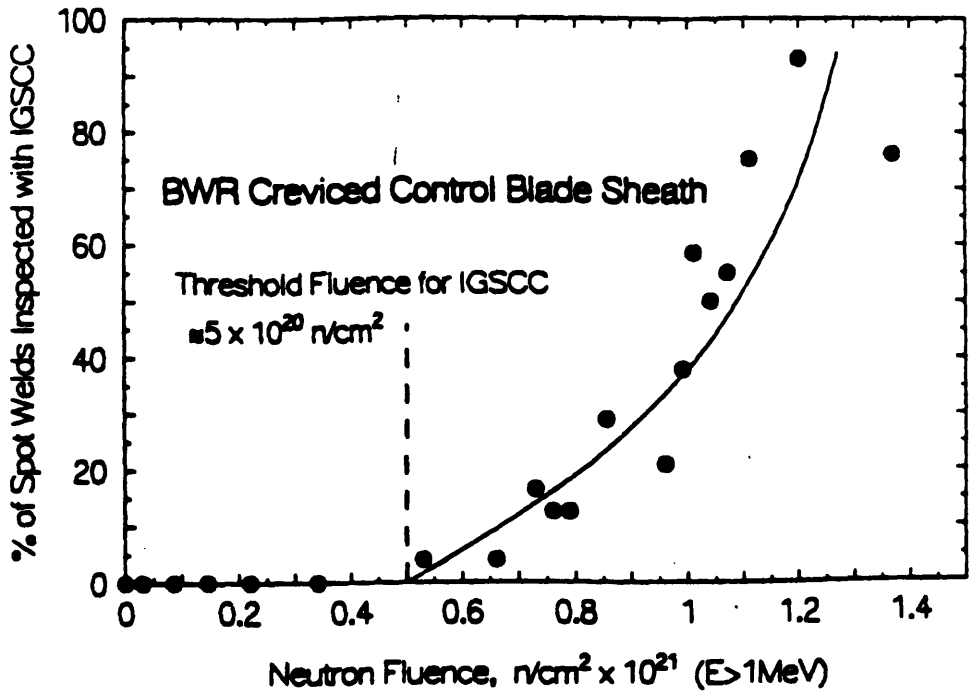

Figure 1.8: Dependence of IASCC on fast neutron fluence for creviced control blade sheath in high conductivity BWR's. [50]

1.4. Radiation Induced Segregation

Radiation-induced segregation (RIS) is the preferential migration of atoms in a point defect flux (i.e., vacancies and self-interstitials) directed either away from or towards point-defect sinks. [51] When high energy particles bombard a metal, atoms are displaced to interstitial sites, with a resultant increase in vacancy concentration. Point defects such as these directly affect the metal by reducing its ductility and fracture toughness. [52] The damage is further intensified by the diffusion of vacancies and interstitial atoms to sinks, such as surfaces or grain boundaries resulting in non-equilibrium segregation (RIS). [53] The observed consequences of such segregation is a collection of compositional profiles illustrated in Figure 1.9.

At the grain boundaries, research to date shows a decrease in Cr, Mo, Fe, and Ti and an increase in Si, P, S, and Ni for austenitic stainless steels. The presence of the latter impurities were shown by Jacobs *et al.* [54] to lower the strain required for material susceptibility to IASCC.

Although the profiles seen in Figure 1.9 look similar to those caused by thermal segregation at the grain boundaries, the radiation-induced segregation process is fundamentally different. First, the impurity level at the interface is usually much higher. Also, the basic defects produced by radiation, vacancies and interstitials, reach concentration levels that are orders of magnitude greater those at thermal equilibrium. This also leads to diffusion of solutes by vacancy or interstitial methods that is greatly accelerated in comparison to the thermal equilibrium rates. Also, a basic characteristic of RIS profiles is their narrowness (typically on the order of 5-10 nm at the grain boundaries). [55] One should also note that chromium depletion at the grain boundaries due to RIS does not have to be accompanied by chromium-carbide depletion. [56]

In general, because different atomic species in an alloy diffuse at different rates with respect to the interstitial and vacancy flux that is produced by the radiation, some species move towards the sinks while others move away. [57] In RIS it has been observed that the directions of segregation are dependent upon the atomic volume of the solute. Subsized solutes preferentially migrate with the interstitial flux, whereas, oversized solutes preferentially migrate with the vacancy flux. [58] The driving force for these phenomena can best be understood by two major mechanisms which occur at various times depending on the concentrations of the solutes in the alloy. These mechanisms are the inverse Kirkendall effect and solute-defect binding.

For low solute concentration alloys, segregation results primarily due to strong binding between solute species and point defects. [59] In this mechanism, known as self-interstitial (SI)-solute binding, it is energetically favorable for self-interstitials to bind with an undersized solute atom. This is due to the fact that self-interstitials have a very large lattice strain energy associated with them. If the migration energy of this complex is less than the dissociation energy, this structure becomes mobile in the lattice. This SI-solute complex is still affected by the SI concentration gradient, however, which causes it to migrate towards the sink taking the undersized solute along with it. Some typical undersized solutes, or impurities in the matrix are sulfur, silicon, and phosphorous [60]

The second mechanism by which RIS takes place occurs mainly in high solute concentration alloys (more than a few percent solute). [61] This mechanism is known as the inverse Kirkendall effect. In this mechanism, solute segregation occurs due to defect concentration gradient. The irradiation-produced vacancies have to exchange positions with atoms in the lattice in order to diffuse to the sink. In doing so, they preferentially exchange with the faster diffusing species. This is illustrated in the cartoon Figure 1.10. This causes a decrease in the faster diffusing species at the grain boundaries (such as Cr in austenitic stainless steels), and, due to the local conservation of mass, a corresponding increase in the concentration of slower diffusing species at such sinks. [62]

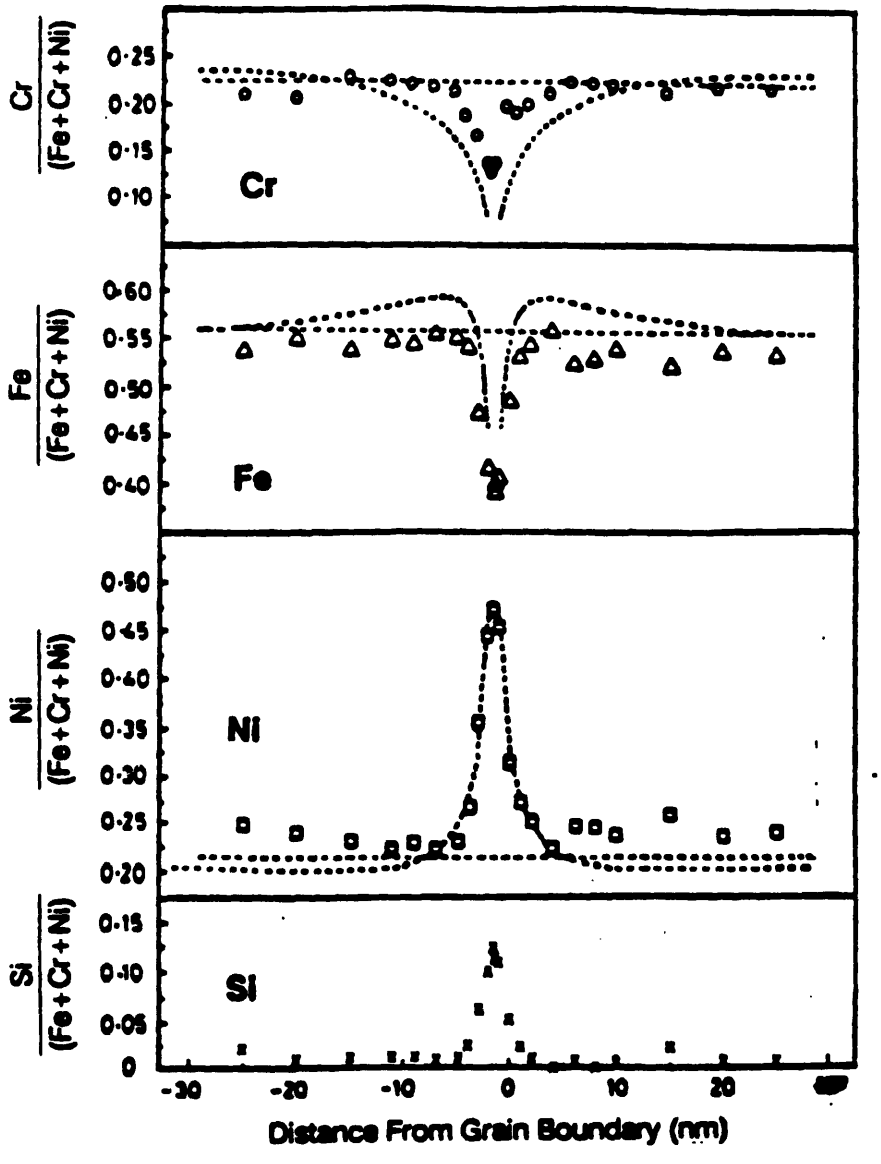

Figure 1.9: Composition profiles across grain boundaries obtained by D-Stem in a 20Cr-25Ni-Nb stainless steel irradiated to 2 to $5x10^{21}$ n/cm^2 at 288 C. Data are compared with predictive modeling of RIS. [63]

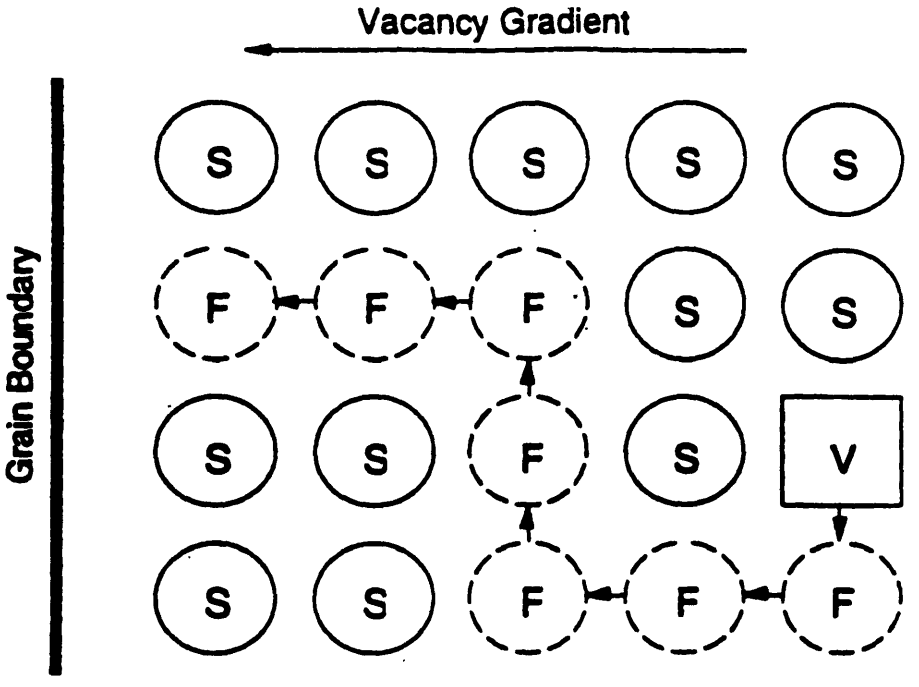

Figure 1.10: Cartoon of the inverse Kirkendall effect. Faster diffusing species are depleted from the near boundary region under the vacancy flux. [64]

It is clear from the above segregation profiles and mechanisms, that different alloying elements segregate in different directions, but what still needs to be understood is the effects of the different elements on each other. Many effects have been seen in commercial purity stainless steels, such as Type 304 but with such high impurity levels and the presence of so many solutes, there are too many different variables in order to postulate how one element can affect the RIS of another.

At Harwell Laboratory research has begun in the study of RIS using experimental alloys where the "composition and irradiation conditions have been varied in a systematic manner." [65] After examining grain boundaries with a STEM, in different Fe-Cr-Ni alloys where the only major difference between the samples was a Ni concentration change from 15% to 35% , it was

observed that chromium depletion at the boundaries was highly dependent upon Ni concentration, but Ni segregation to the boundary was not. The grain boundary nickel level was increased by 13 $\pm$ 6 wt% regardless of the initial concentration of nickel. On the other hand, when Ni concentration was increased, the Cr grain boundary concentration depletion changed from 6 $\pm$ 1 wt% to 2 $\pm$ 1 wt%. [66]

1.5. Present Work and Motivation for Research

A full understanding of IASCC and how all factors relate and culminate in material failure is still not known. In order to piece together some of the known factors, however, a series of carefully selected materials have been pre-irradiated at the MIT Nuclear Reactor Laboratory. These materials are in the form of SSRT, TEM, and Auger specimens so that several methods of analysis can be used to ascertain what occurs when IASCC is seen.

The slow strain-rate tensile (SSRT) specimens will be placed in a rig which positions them in the center of the MITR-II reactor-core while exerting on them a tensile load as shown in Figure 1.11. This rig also functions as an isolated loop from the MIT nuclear reactor thus allowing other parameters to be adjusted so as to create a BWR environment. After a slow strain rate test is complete, the specimen will be examined for signs of IASCC occurrence.

In conjunction with the SSRT testing, the TEM specimens, some of which are made of the same material as the SSRT specimens and irradiated to the same fluences, will be analyzed using a transmission electron microscope (TEM), a scanning transmission electron microscope (STEM), and electro-potentiokinetic reactivation (EPR) testing. This will provide both analytical and electro-chemical analysis of the micro-structure and micro-composition of the materials. In this manner, if IASCC is seen in the SSRT specimens, the

corresponding TEM specimens can provide the information as to what is a susceptible material.

The full effect of different solutes on each other with respect to RIS is still not known, and much work is being done to understand this. At the M.I.T. Nuclear Reactor Lab (MIT-NRL), a computer code has been written by Boerigter [67] to model the effects of neutron-irradiation induced segregation in tertiary austenitic stainless steels. In order to validate this computer model, in this thesis, analytical electron microscopy (AEM) will be used to examine grain boundaries in a carefully selected series of materials. Corrosion testing will also be done, and with the data obtained, it is hoped to be able to update the computer model to better simulate RIS.

Concern with the phenomenon of IASCC is rising in the nuclear power community for both vendors and utilities associated with both Pressurized-Water Reactors (PWRs) and Boiling-Water Reactors (BWRs). Replacing in-core components is expensive both material-wise and in facility down-time, and the threat to major internal components causes even more alarm. Also, the recent increase in failures of lower-stressed components and the fact that there appears to be a threshold fluence means that more failures may occur in the future. [68] The purpose of the work in this thesis is to provide information on the RIS process that can be used in the modeling and the understanding of this phenomenon.

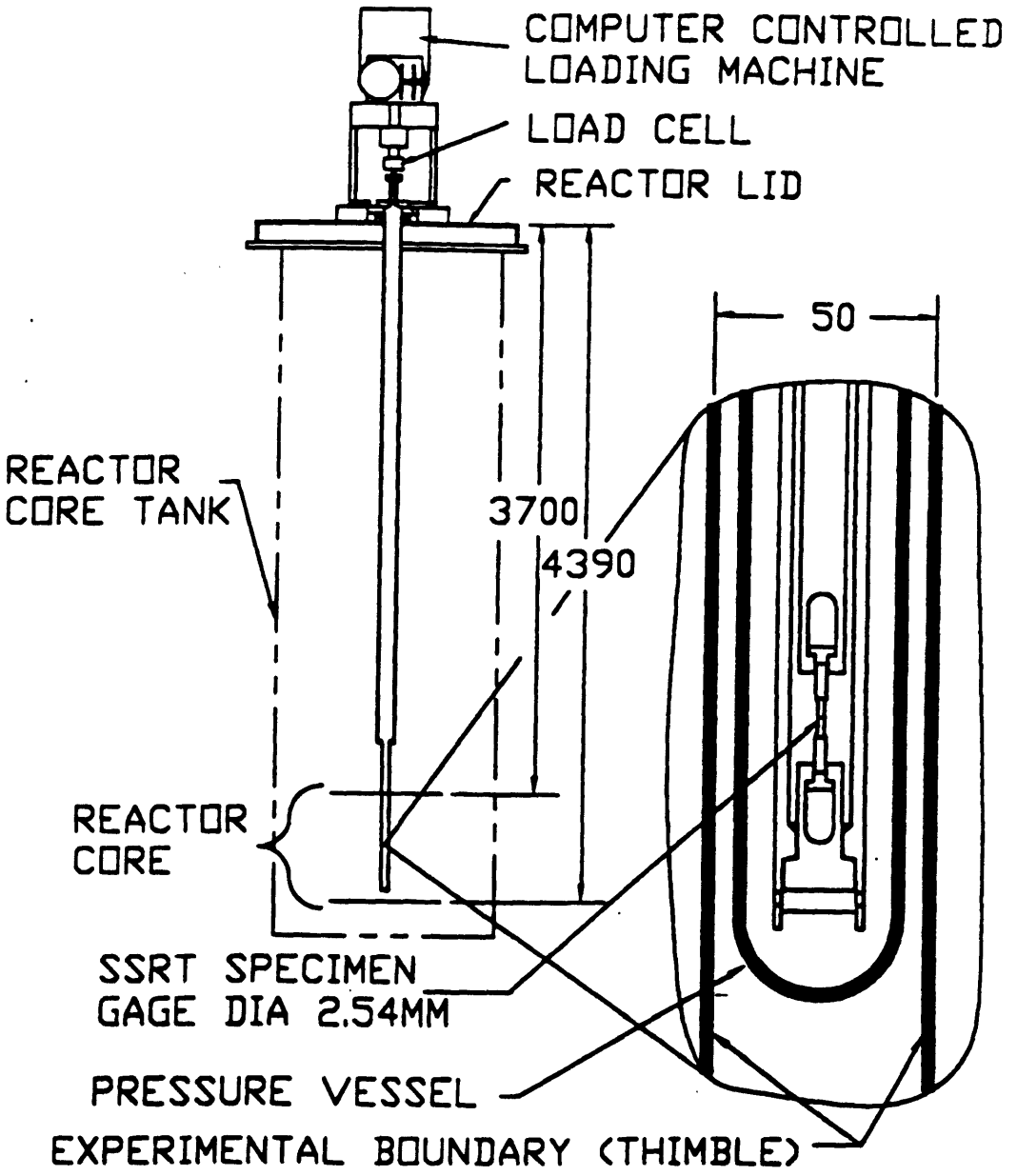

Figure 1.11: SSRT Rig for study of IASCC and RIS. [69]

1.6. REFERENCES:

1. Russell H. Jones, ed., Stress Corrosion Cracking, ASM International, Materials Park, Ohio, 1992, p.181.

2. G.S. Was and Peter L. Andresen, "Irradiation-Assisted Stress Corrosion Cracking in Austenitic Alloys", JOM, April 1992, p.8.

3. Was and Andresen, p.10.

4. Aimone. pp 30 and 39.

5. Jones, p.181.

6. Julio A. V. Aimone, "The Development of a Facility for the Evaluation of Environmentally Assisted Cracking of In-Core Structural Materials in Light Water Reactors", PhD Thesis, Dept. of Nucl. Eng., M.I.T., (May 1992), p.30.

7. Jones, p.1.

8. Aimone, p.32.

9. H.H. Uhlig and R.W. Revie, Corrosion and Corrosion Control: an Introduction to Corrosion Science and Engineering, 3rd ed., John Wiley and Sons, New York, 1985, p.308.

10. R.M. Latanison, O.H. Gastine, and C.R. Compeau, "Stress Corrosion Cracking and Hydrogen Embrittlement: Differences and Similarities", paper presented at the symposium on Environment Sensitive Fracture of Engineering Materials, Fall AIME meeting, 24-26 Oct., 1977, p.3.

11. Notes from 22.70 taught by Prof. R. Ballinger, Fall of 1992.

12. T.P. Hoar and J.G. Hines in Stress Corrosion Cracking and Embrittlement, Wiley, New York, 1956, p.107.

13. F. A. Champion, in Symposium on Internal Stresses in Metals and Alloys, Inst. of Metals, London, 1948, p.468.

14. H. L. Logan, J. Res. N. B. S., 48, 99 (1952).

15. A. J. Forty, Physical Metallurgy of Stress Corrosion Cracking, Interscience, New York, 1959, p.99.

16. N. J. Petch, Phil. Mag., 1, 331 (1956).

17. H. H. Uhlig, in Ref. 18, p.1.

18. Aimone, p.37.

19. Aimone, p.32, and Uhlig, Corrosion and Corrosion Control, p.14.

20. Aimone, p.33.

21. P. L. Andresen, F. P. Ford, S. M. Murphy, J. M. Perks, "State of Knowledge of Radiation Effects on Environmental Cracking in Light Water Reactor Core Materials," Proceedings of conference on Environmental Degradation of Materials in Nuclear Power Systems, Jekyll Island, GA, August, 1989, p.3.

22. Was and Andresen, p.107.

23. B. M. Gordon and G. M. Gordon, "Material Aspects of BWR Plant Life Extension", Nuclear Engineering and Design, 98, (1987), p.118.

24. Gordon and Gordon, p.118.

25. Gordon and Gordon, p.119.

26. Gordon and Gordon, p.119.

27. Gordon and Gordon, p.119.

28. J. O'Donnell, PhD candidate student, Seminar on IASCC, M.I.T., 25 November, 1992.

29. Jones, p.181, and Andresen and Ford, p.2.

30. Aimone., p.40.

31. Was and Andresen, p.11.

32. Andresen and Ford, p.108.

33. Andresen and Ford, p. 90.

34. Was and Andresen, p.12.

35. Was and Andresen, p.12, Andresen and Ford, p.90.

36. Andresen and Ford, p.91.

37. Jones, p.192.

38. Was and Andresen, p.12.

39. Jones, p.203.

40. Was and Andresen, pp.8-10

41. Was and Andresen, p.11.

42. Jones, p.182.

43. Was and Andresen, p. 8.

44. Was and Andresen, p.11.

45. Andresen and Ford, p.84.

46. Jones, p.189.

47. Jones, p.181.

48. T.R. Anthony, "Solute Segregation and Stresses around Growing Voids in Metals", Proc. Radiation Induced Voids in Metals and Alloys, Eds. J.W. Corbett and L.C. Ianiello, U.S. Atomic Energy Commission Sym. SDeries 26, CONF 710601, 1971, p.630.

49. Andresen and Ford, p. 84.
50. Jones, p.182.

51. Stephen T. Boerigter, "An Investigation of Neutron-Irradiation Induced Segregation in Austenitic Stainless Steels", PhD Thesis, Dept. of Nucl. Eng., M.I.T., (December 1992), p.29.

52. Andresen and Ford, p.84.

53. Andresen and Ford, p.84.

54. A.J. Jacobs, R.E. Clausing, M.K. Miller, and C. Shepherd, "Influence of Grain Boundary Composition on the IASCC Susceptibility of Type 348 Stainless Steel", in Proc. 4th Int'l Conf. on Env. Degredation of Materials in Nuc. Power Systems, Nat'l Assn. of Corrosion Engineers, 1990.

55. Was and Andreson, p.10.

56. Andresen and Ford, p. 84.

57. Colin A. English, S.M. Murphy, and J.M. Perks, "Radiation-induced Segregation in Metals",J. Chem. Soc. Faraday Trans., 1990, 86(8), p. 1263.

58. Was and Andresen, p.10.

59. S. Dumbill and T.M. Williams, "Irradiation-induced grain boundary segregation in neutron irradiated Fe-Cr-Ni alloys", work done as part of the UKAEA Underlying Research Programme, Harwell Laboratory, p. 119.

60. Boerigter, p.31.

61. Dumbill and Williams, p.119.

62. Boerigter, pp. 29-30.

63. Was and Andresen, p.10.

64. Boerigter, p.30.

65. Dumbill and Williams, p.119.

66. Dumbill and Williams, p.122.

67. Boerigter, PhD Thesis.

68. Was and Andresen, p.9.

69. J. O'Donnell.

Chapter 2

2. Materials Selection

2.1. Introduction

At the MIT Nuclear Reactor Laboratory, a series of metals in the form of SSRT, Auger, and TEM specimens have been pre-irradiated with the goal of studying the phenomena of IASCC. A listing of these materials and their elemental composition is given in Appendix I. Ten of these alloys, designated as N1 through N10, are high-purity experimental alloys made with the intent of benchmarking the radiation induced segregation (RIS) code written by Boerigter [1]. These materials will be used as a control because their elemental composition is precisely known. Furthermore, other conclusions may be drawn about the processes of RIS and sensitization and the effect other elements in an alloy can have on these phenomena.

The plan for STEM work on the irradiated materials was two-fold. STEM analysis priority initially corresponded with the test sequence of the SSRT specimens. However, validation of the RIS model, developed at MIT, will best be achieved by comparisons of predictions for the above-mentioned model alloys, also irradiated as part of the program. With the use of the scanning transmission electron microscope (STEM) and electrochemical potentiokinetic reactivation (EPR) testing, it is hoped that the degree of RIS at the grain boundaries can be determined and that this information will lead to clues concerning the role that the major alloying elements play in RIS.

2.2. Specimen composition

2.2.1. Motivation for Selection of Specimen Composition

The experimental alloys designated N1 through N10 are high purity Fe-Ni-Cr alloys with systematically varied compositions. The rational in choosing their compositions stems from previous research which postulates that the amount of nickel affects the depletion of chromium. Harwell data suggests that higher nickel concentrations diminish the amount of chromium depletion. [2] On the other hand, most model's simulations conflict with this and predict that an increased nickel concentration actually enhances the amount of chromium depletion seen at the grain boundary. This is understood by the fact that as the slower diffusing species, Ni, replaces the faster diffusing one, Fe, and as concentrations of the slower species increases, the relative effects should be seen as well. [3] It is hoped that by varying the nickel concentrations over the same range in both a high-chromium and a low-chromium series of alloys one can determine how the alloying elements affect the degree of RIS.

2.2.2. Elemental Composition

For the precise elemental compositions of the experimental alloyswas determined by wet chemistry. The results of this are listed in Table 2.1.

Table 2.1. Composition in wt% of the experimental alloys N1-N10

Alloy	Ni (wt%)	Cr (wt%)	C (wt%)	S (wt%)	P (wt%)	Si (wt%)	Mn (wt%)
N1	21.1	17.4	0.005	0.004	<0.004	0.059	0.19
N2	30.2	17.2	0.007	0.003	<0.004	0.025	0.20
N3	40.0	17.5	0.008	0.002	<0.004	0.013	0.20
N4	49.7	17.6	0.004	0.003	<0.004	0.013	0.21
N5	60.3	17.5	0.002	0.002	<0.004	0.014	0.21
N6	21.1	25.6	0.002	0.005	<0.004	0.015	0.19
N7	31.3	25.4	0.004	0.004	<0.004	0.018	0.21
N8	39.7	25.1	0.005	0.003	0.004	0.019	0.21
N9	50.9	24.9	0.003	0.002	<0.004	0.023	0.19
N10	60.4	25.3	0.002	0.002	<0.004	0.011	0.20

2.3. Specimen manufacturing and pre-irradiation thermal history

To perform the STEM analysis and EPR testing, TEM specimens were prepared from the above materials. Due to difficulties in manufacture, two batches of the TEM specimens were manufactured for study, the second batch being those intended for the project. This is mentioned because both batches went through the same pre-irradiation heat treatment, thus, allowing data of non-irradiated specimens to be collected from TEM specimens of the first batch. A description of the manufacturing process for both batches is as follows.

The first batch of TEM specimens were manufactured by wire-EDM; cylinders were cut out of the material, and these cylinders were then cut into thin discs with a thickness of 10 mils. These discs were lapped down to the final thickness of 4-6 mils, but after this last treatment, it was noticed that the

discs had a cupped appearance on one side, and the inside of this cupped area had a thickness of much less than 4-6 mils. The jet-thinning process was tested on some specimens, but was found not to be adversely affected. Treatment of the specimens then continued by having them solution annealed at 1050°C for one-half hour to achieve a known microstructure. [4]

The second batch of specimens was cut into cylinders by wire-EDM and solution-annealed and quenched in this form. These cylinders were then sliced into discs of 12 mil thickness by wire-EDM and were hand ground down to a 10 mil thickness using 800 grit SiC paper. [5]

2.4. Dry-irradiation and In-Core thermal history

2.4.1. Capsule Design

The irradiation of the TEM specimens along with the Auger and SSRT specimens occurred as part of the MIT IASCC Project. A dry irradiation rig was designed by S. Boerigter and began continuous operation in the MIT Reactor on November 11, 1990. This rig consisted of eight aluminum capsules all of which contained TEM specimens except for three, capsules #2, #6, and #8. Figures 2.1 [6] and 2.2 [7] show the dry irradiation assembly, and the design of the TEM specimen containing capsules. [8] In this figure, the holes that the SSRT specimens were placed in can clearly be seen, and the hole for the Auger specimens is similar to that of the TEM specimens.

Note that the hole in which the TEM specimens were placed has a counter-sink of 0.12 inches in diameter. TEM specimens were stacked into a cylindrical shape and hand-placed into the capsule holes. A plug was then press-fitted in the end that they were placed in to keep them in place.

Once all specimens were placed in the eight capsules, these capsules were welded together, end to end, and the welded stack was turned to its final diameter of 1.726 inches and irradiated.[9]

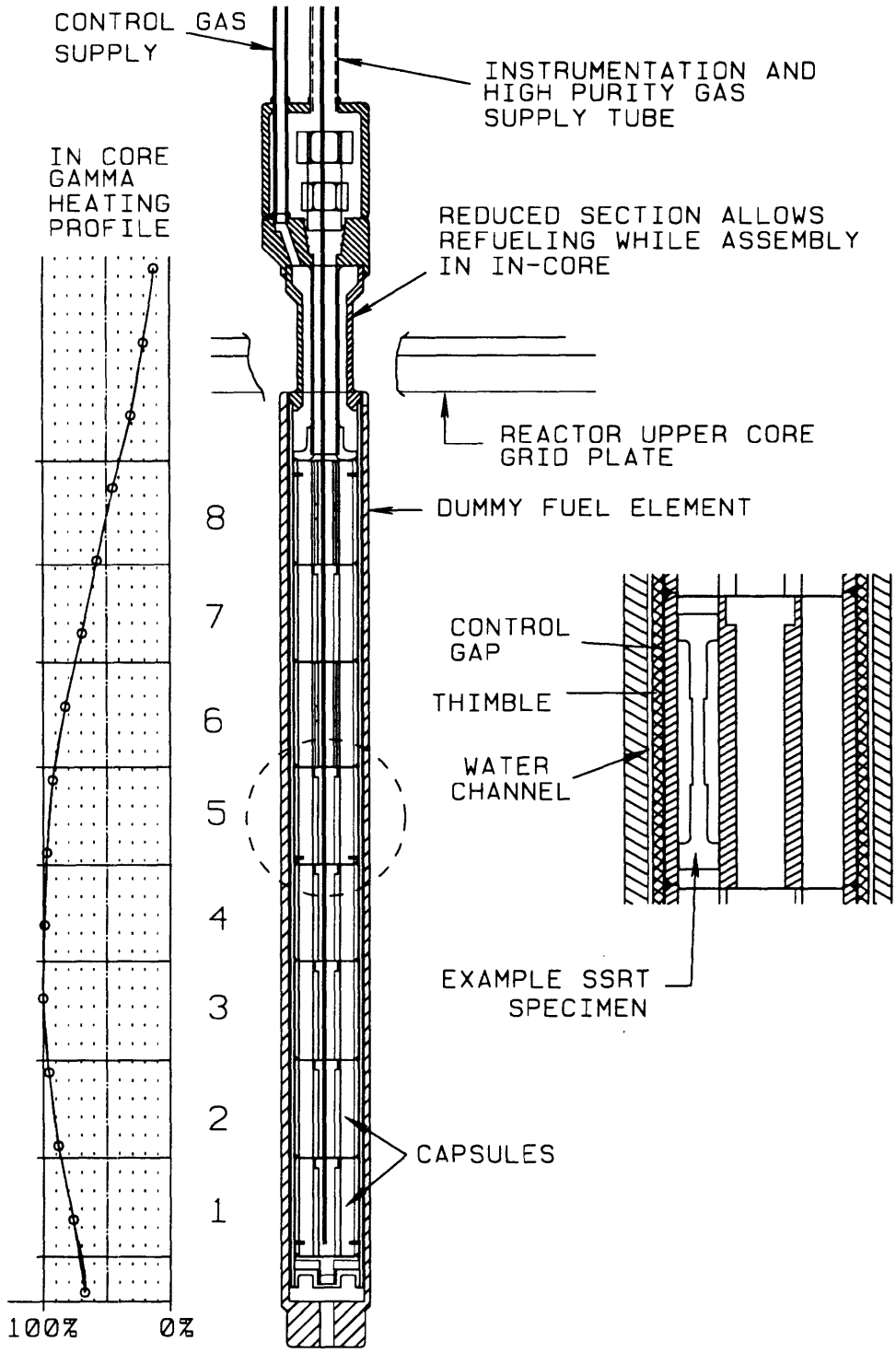

Figure 2.1. Dry irradiation assembly shown with the dummy fuel element and the nuclear heating profile.

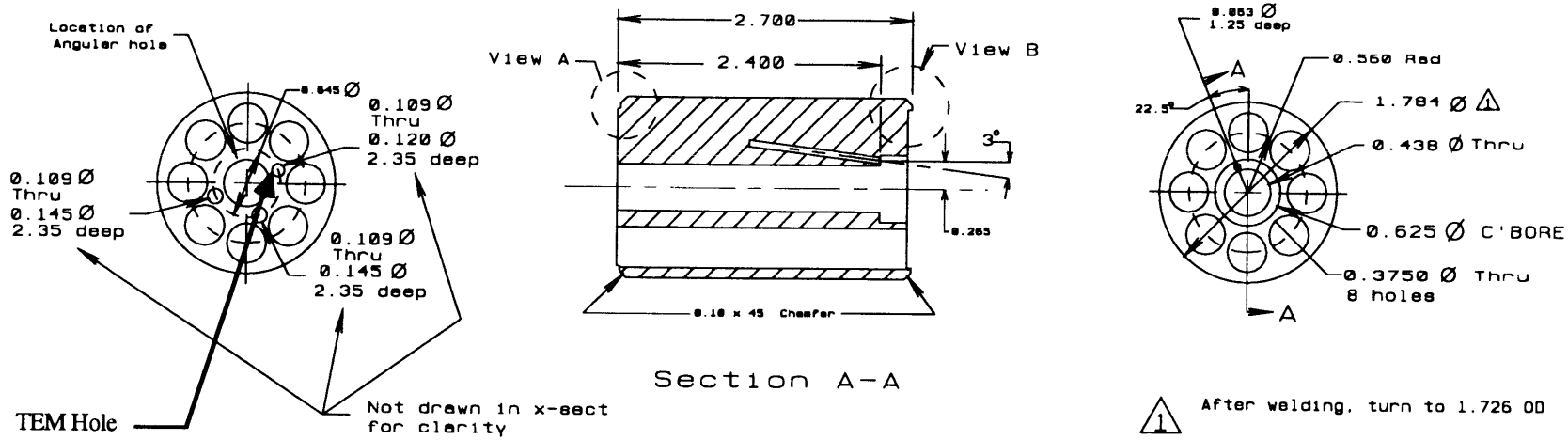

Description	QTY	Material	Stock
St. cap.	7	6061-T6	2" OD Rod

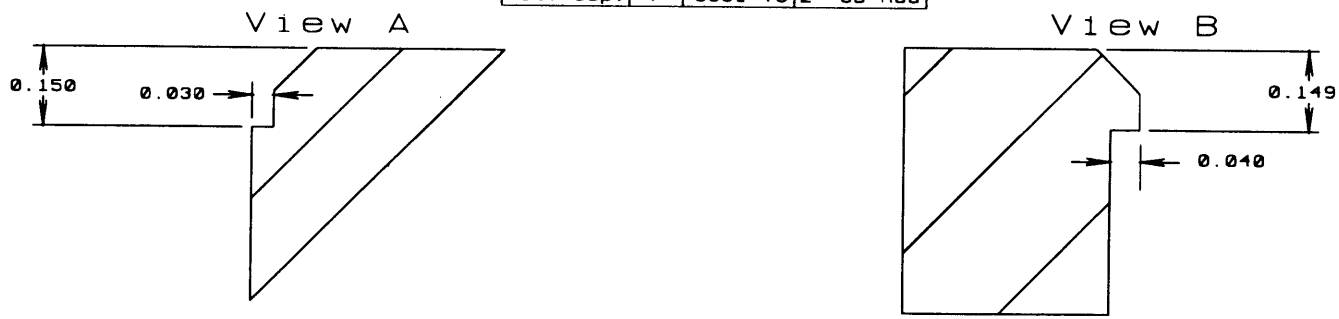

Figure 2.2. Standard Specimen Capsule

2.4.2. Capsule Dosimetry

Along with the TEM specimens, ultra-high purity iron dosimeters were also placed in the TEM holes during the irradiation. These dosimeters served to determine the actual fast neutron irradiation damage that the TEM specimens were exposed to during the irradiation. The fast neutron fluence varies axially depending on the location in the reactor core as as shown in Figure 2.3. These fluence calculations were made by using the radioactive isotope ^{54}Mn. This isotope is created by the following reaction:

$$^{54}Fe + n \text{ --------> } ^{54}Mn + p$$

The above reaction requires a neutron threshold energy of approximately 1 MeV which also corresponds to the minimum neutron energy responsible for any significant damage in stainless steel. ^{54}Mn decays by a single-energy gamma emission, and by the use of a germanium detector the dose that the TEM specimens were exposed to was determined. [10] A complete report of the measurement of the Fe-dosimeters was completed by H. Mansoux and is shown in his SM thesis. [11]. Figure 2.3 summarizes some of the results and shows the error associated with the measurement technique.

From the resulting dosimetry, the irradiated TEM specimens were divided into two categories, those that were exposed to more than 0.7 dpa which were labeled High-Dose specimens, and those which were exposed to less than 0.7 dpa which were labeled Low-Dose specimens. These labels correspond to specimens from capsules 3, 4, and 5, and to specimens from capsules 1 and 7 respectively. A listing of where the 'N'-alloy TEM specimens were placed and their corresponding fluences is given in Table 2.2.

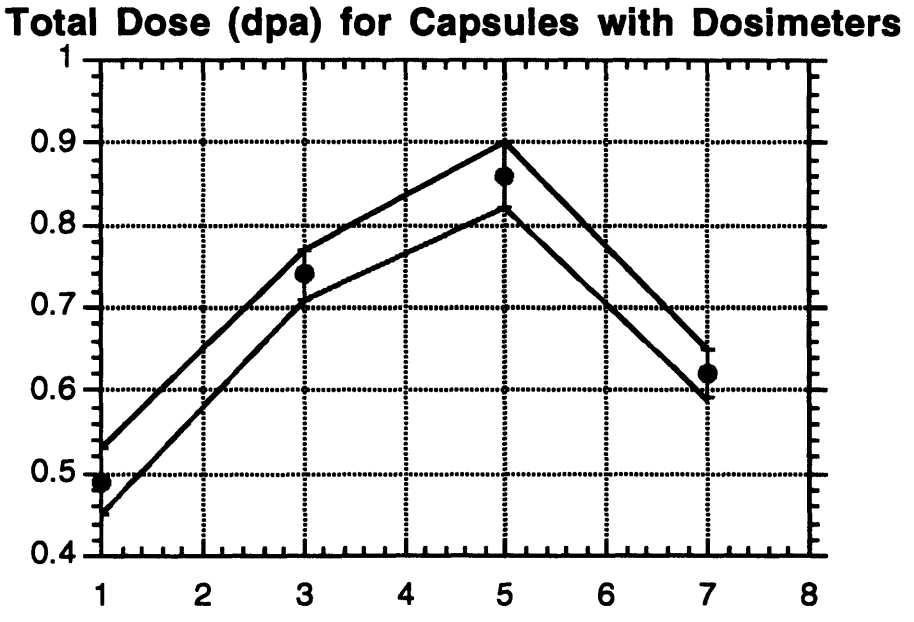

Figure 2.3. Axial Dose Distribution of Irradiated Capsule Stack

Table 2.2. Experimental Alloy Positions in Capsule Irradiation Stack.

Alloy	Capsule 1	Capsule 3	Capsule 4	Capsule 5	Capsule 7
N1	1	1	2	1	2
N2	0	1	3	0	5
N3	3	4	1	0	1
N4	0	0	2	0	1
N5	3	0	3	2	1
N6	1	4	0	0	2
N7	4	0	2	2	2
N8	2	3	2	1	2
N9	2	0	3	0	1
N10	1	1	2	2	3
	0.49 dpa	0.74 dpa	0.8 dpa	0.86 dpa	0.62 dpa

2.4.3. In-Core Thermal History

Irradiation of the specimens took place in an inert gas environment of CO_2 and He. During irradiation, which lasted for a total of 220 days at a reactor power of 4.5 MW, the design temperature was planned to be

300°C±5°C at the gauge section of the SSRT specimens. The reasons for this are two-fold. Damage characteristics are temperature dependent. Therefore, during all times of irradiation, regardless of reactor power, the dry irradiation rig was designed to operate at this 300°C temperature. Also, even short periods of temperatures in excess of 300°C can cause damage by annealing the regions where segregation may have occurred. This is a highly temperature dependent phenomena; therefore, the absolute temperature was never to exceed 325°C. [12]

In order to protect the specimens from annealing damage, alarms were added to the rig to warn of temperatures of 310°C, 315°C, and 330°C. Fortunately, none of these alarms were ever set-off in the course of the entire dry irradiation run. [13]

Although the design goal was to achieve a flat temperature distribution among all the specimens, this was achieved with only partial success. Dose weighted temperature histograms were calculated for each capsule, and from this the dose weighted temperature standard deviations for each capsule were also calculated. [14] The results are shown in Figure 2.4. [15], and they show a nominal temperature distribution. This axial distribution of temperatures is still acceptable with respect to useful metallurgical information that can be obtained.

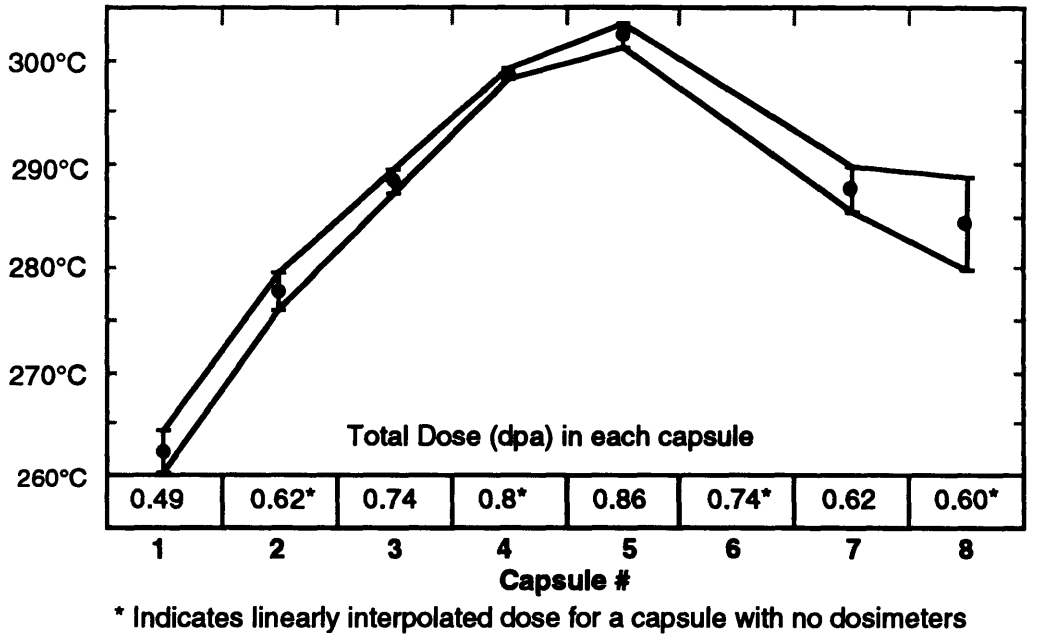

Figure 2.4. Standard deviation of the temperature range for each capsule in the dry irradiation and the estimated damage accumulated in each capsule.

2.5. Specimen Transfer

2.5.1. Specimen Removal

The second batch of TEM specimens had their thickness chosen in part to protect them from any cold working that may be induced during their removal. From hindsight, this was very beneficial when removing them from the irradiation capsules. The designed plan for removal was to push the specimens out. However, with aluminum to aluminum friction of the press fitted plugs being much stronger after irradiation than before, a light push did not free the specimens. To complicate the process further, the weld that had held the dry-irradiation capsules together, had penetrated into the capsule assembly and partially covered most of the TEM holes. Due to difficulty in removing the SSRT specimens, it was decided to remove the TEM specimens first. [16]

With all these obstacles to overcome, TEM removal became much more difficult than originally planned. The first task to overcome was to clear the openings of the TEM holes from weld material. This was done by lowering a dremel tool fitted with a small bit into the hot cell. While one person used a manipulator to hold a capsule tightly on the table in the hot cell, another operator used the other manipulator to guide the dremel tool over the TEM hole and grind away the overlying weld material.

After clearing the TEM holes in the above process, the removal of the specimens began. A #39 drill blank was chosen for pushing the specimens out. This size of drill blank fit easily into the smaller-diameter side of the TEM hole but also had a large enough diameter to belay fears of it bending while pushing on the TEM specimens.

Before pushing out the TEM specimens, the selected capsule was placed in an aluminum funnel that served two purposes. First, it held the capsule while the TEM specimens were being pushed out, and it also channeled the pushed out TEM specimens into a cup waiting below the capsule. This whole assembly was placed in the bottom half of the lead transfer pig that was used to transport the TEM specimens out of the hot cell. This assembly is illustrated in Figure 2.5.

Once in the cup, the lead transfer pig was lifted out of the hot cell and placed in a concrete transfer cask. In this fashion, the TEM specimens were moved to a hot box for sorting and storage in lead bricks. This procedure was repeated six times, once for each capsule containing TEM specimens.

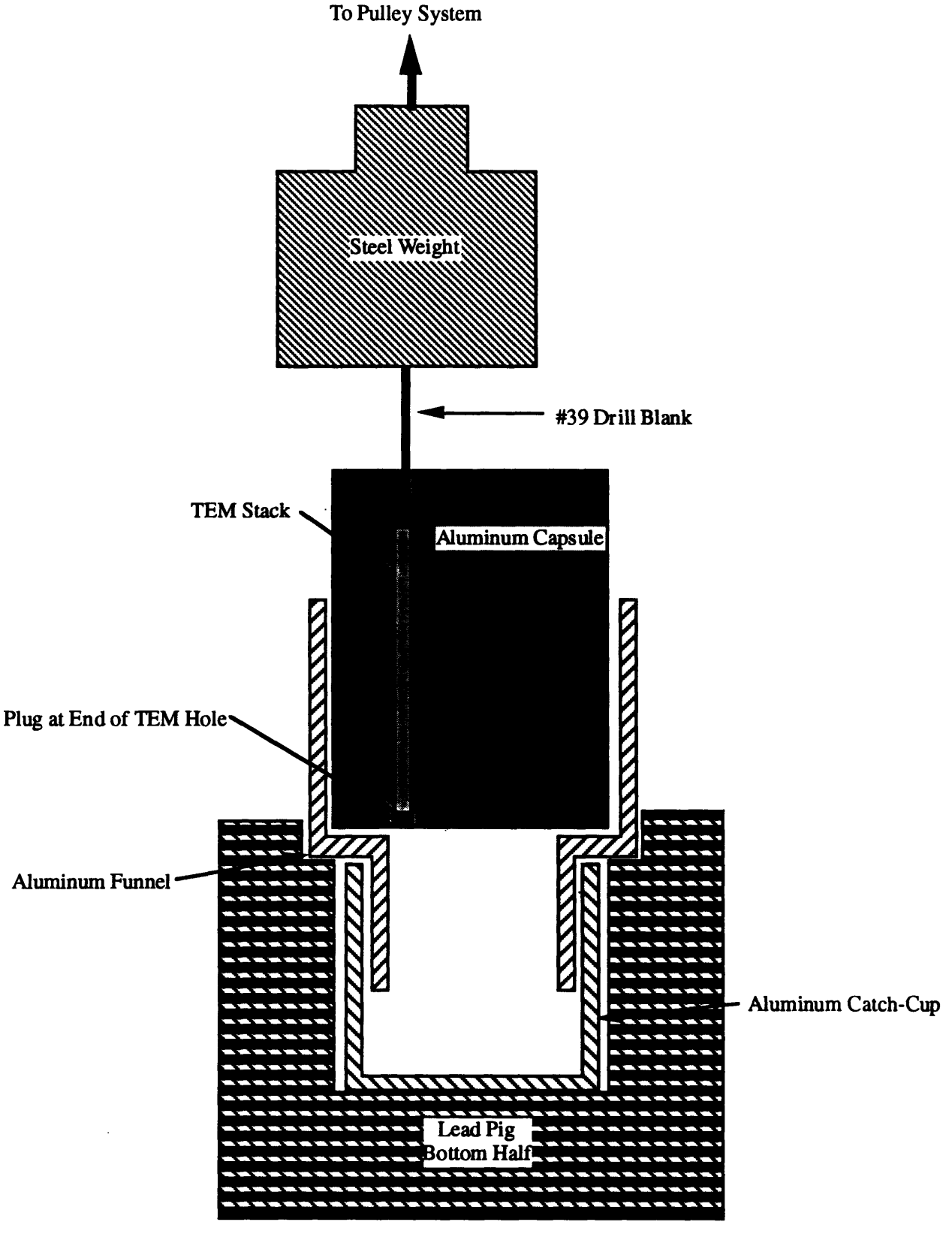

Figure 2.5. TEM Capsule Extraction and Transfer Assembly.

2.5.2. Specimen Storage

Sorting of TEM specimens occurred in the TEM hot box. Lead bricks with small holes in them were marked with different colored paint and arranged in the hot box. TEM specimens were placed in vials that fit in the holes of the lead bricks, and the TEM specimens were arranged by capsule and material. A detailed overview of the specimen storage is shown in Appendix II. This also contains the current listing of what specimens were used for what tests, and which specimens are currently available for testing.

2.6. References:

1. Stephen T. Boerigter, "An Investigation of Neutron-Induced Segregation in Austenitic Stainless Steels", PhD Thesis, Dept. of Nucl Eng., M.I.T., (December 1992).

2. S. Dumbill and T.M. Williams, "Irradiation-induced grain boundary segregation in neutron irradiated Fe-Cr-Ni alloys", work done as part of the UKAEA Underlying Research Programme, Harwell Laboratory, pp. 122-123.

3. Boerigter, PhD Thesis, (December 1992).

4. Boerigter, PhD Thesis, (December 1992), p. 311-312.

5. Boerigter, PhD Thesis, (December 1992), p. 312.

6. Boerigter, PhD Thesis, (December 1992), p. 121.

7. Boerigter, PhD Thesis, (December 1992), p. 124.

8. Boerigter, PhD Thesis, (December 1992), p. 121 and p. 124.

9. Boerigter, PhD Thesis, (December 1992), pp. 165-166.

10. Mansoux H., "Experimental Determination of Radiation Induced Segregation Susceptibility in Austenitic Stainless Steels", SM Thesis, Dept. of Nuclear Engineering, M.I.T., (May 1994).

11. Mansoux, SM Thesis, (May 1994).

12. Boerigter, PhD Thesis, (December 1992), pp. 92-93.

13. Boerigter, PhD Thesis, (December 1992), p. 140 and p. 150.

14. Boerigter, PhD Thesis, (December 1992), p. 151.

15. Boerigter, PhD Thesis, (December 1992), p. 152.

16. Boerigter, PhD Thesis, (December 1992), pp. 165-166.

Chapter 3

3. Analysis Methods and Results

3.1. Introduction

Analysis of the experimental alloys, N1 through N10, was done with two main goals in mind. The first of these was to use the data to benchmark the RIS code written by Boerigter [1]. The other goal was to determine what effect the major alloying elements have on each other with respect to segregation. Both of these goals necessitate the use of high-purity tertiary alloys for several reasons; Boerigter's code was written for tertiary alloys, not accounting for the presence of impurities, and the high purity experimental alloys serve as control alloys in that their elemental compositions are precisely known. Furthermore, because their compositions are varied in a systematic manner, some conclusions may be drawn about the processes of RIS with special attention given to how nickel affects chromium depletion.

The RIS code written by Boerigter contains a series of parameters which aid in describing the segregation process. A strong effort was made to use parameters for which a fundamental theoretical basis exists, so as to avoid a 'fitting' process, and an exhaustive literature search was done to obtain the most accurate values of these parameters. Defect-species exchange rate data is extremely limited in the temperature range of the dry-irradiation [2]. For this reason the values listed for Boerigter's code were extrapolated to lower temperatures from high temperature thermal diffusion tracer measurements made by Rothman *et al.* [3] and/or Perkins, Padgett, and Tunali [4]. A complete listing of the parameters is shown in Table 3.1, along with their initial values determined from the literature search.

Table 3.1. Parameters used in the non-equilibrium segregation calculations.[5]

Quantity	Symbol	This Model
Ni-vacancy migrational enthalpy	$\Delta H^{m}_{V\text{-}Ni}$	1.38 eV
Fe-vacancy migrational enthalpy	$\Delta H^{m}_{V\text{-}Fe}$	1.30 eV
Cr-vacancy migrational enthalpy	$\Delta H^{m}_{V\text{-}Cr}$	1.26 eV
Vacancy Formation Enthalpy	ΔH^{f}_{V}	1.9 eV
Vacancy Formation Entropy	ΔS^{f}_{V}	10 k
Interstitial migrational enthalpy (same for all)	ΔH^{m}_{I}	0.30 eV
Interstitial Formation Enthalpy	ΔH^{f}_{I}	4.0 eV
Interstitial Formation Entropy	ΔS^{f}_{I}	0 k
Vacancy correlation factor	f_V	0.7815
Interstitial correlation factor	f_I	0.44
Lattice parameter	λ	3.4 Å
Recombination Volume	R_V	12
Core Radius of dislocations	r_0	1.5 $\bar{b}$
Percentage of G.B. lattice points where recombination occurs	P_R	10%
Production Efficiency of freely migrating defects	η	30%
Activity Coefficients	γ_j	1

It is these values that will be adjusted so as to correlate the data collected on the experimental alloys with the results of the RIS code. The key parameter to be adjusted is (P_R) which is a measure of the grain boundary angle, indirectly, since the degree of "openness" at the grain boundary

increases with grain boundary angle. Improved simulation will be defined as a better fit of the grain boundary profiles obtained by STEM analysis.

3.1.1. Analysis Methods

In order to validate the RIS code, data was obtained on some of the experimental alloys, N1-N10, through a number of analysis methods. These methods include the use of analytical electron microscopy (AEM); specifically scanning electron microscopy (SEM), and scanning transmission electron microscopy (STEM). Electro-chemical potentiokinetic reactivation (EPR) [6] testing and optical microscopy were also done.

The STEM was used to detect microcompositional changes in the grain boundary region. These results can be used as a direct comparison with the RIS code output. It should be noted, however, that the STEM analyzes a volume of material, whereas the RIS code calculates concentrations at discrete points. This subject will be discussed later in detail.

EPR testing was chosen as a method to determine the general degree of sensitization. Differences between the irradiated specimens and those that were not irradiated were hoped to be seen by differences in the EPR results. In this manner an objective, comparative analysis could be made between the different materials and the unirradiated and irradiated materials.

SEM, EPR testing, and optical microscopy were used to evaluate the microstructure of the material. Corrosion morphology of the surface of a material can be quite easily determined by SEM analysis, and differences in the EPR results between irradiated and non-irradiated versions of the same material can also provide information about microstructural and microchemical changes.

Finally, optical micrographs were taken to determine the grain-size and the general microstructure of the experimental alloys. These, however, were taken of only the non-irradiated materials.

3.2. Optical Microscopy

3.2.1. Sample Preparation

From the original materials, samples of the materials N1 through N10 were cut, solution annealed at 1050°C, and quenched in water. These sample were then mounted and mechanically polished to a 3μ diamond finish. Samples were etched in a solution of 30ml HCl, 15ml HNO_3, and 12ml glycerol [7] was decided upon. Etching time varied depending upon the material, being especially dependent upon the chromium content, but on average required 5 to 10 minutes immersed in the etchant while stirring. The same etchant worked reasonably well on all materials.

3.2.2. Optical Micrographs

After etching, optical micrographs at a magnification of 100X were taken to show the general microstructure and any inclusions, voids, precipitates, or possible phase changes. None were seen. The results are shown in Figures 3.1 through 3.10.

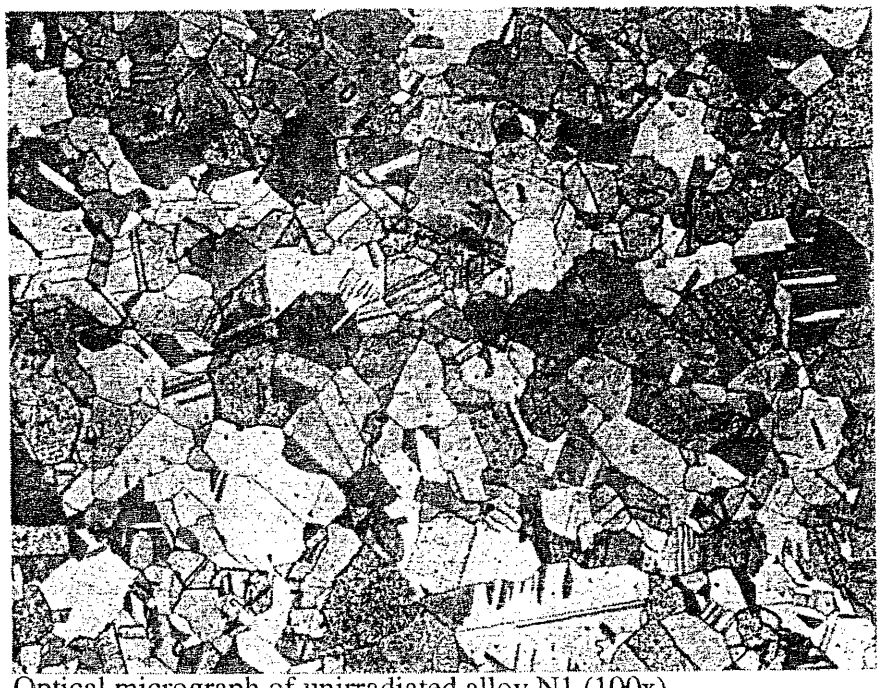

Figure 3.1. Optical micrograph of unirradiated alloy N1 (100x).

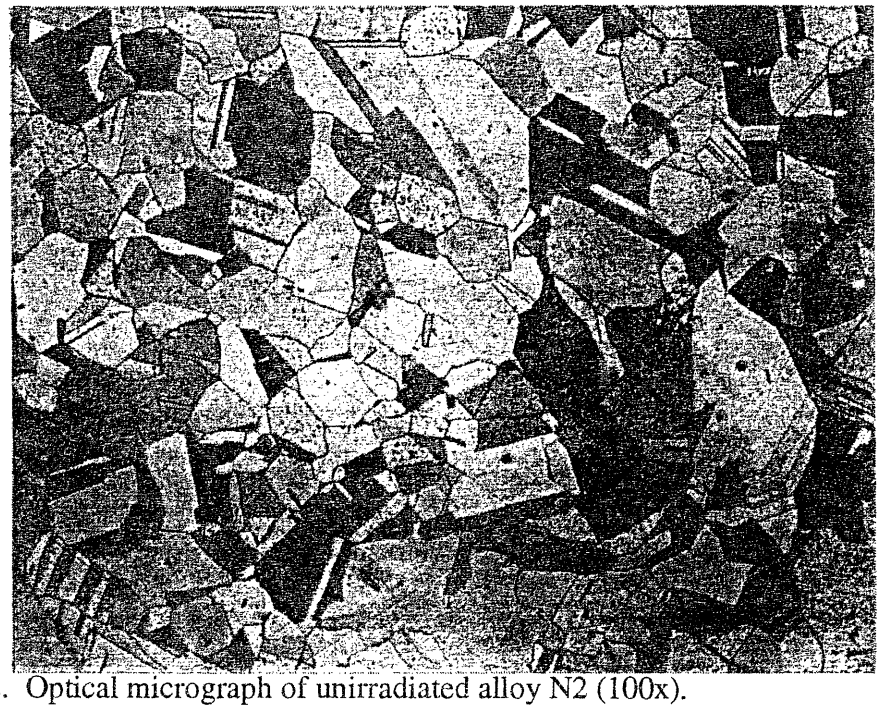

Figure 3.2. Optical micrograph of unirradiated alloy N2 (100x).

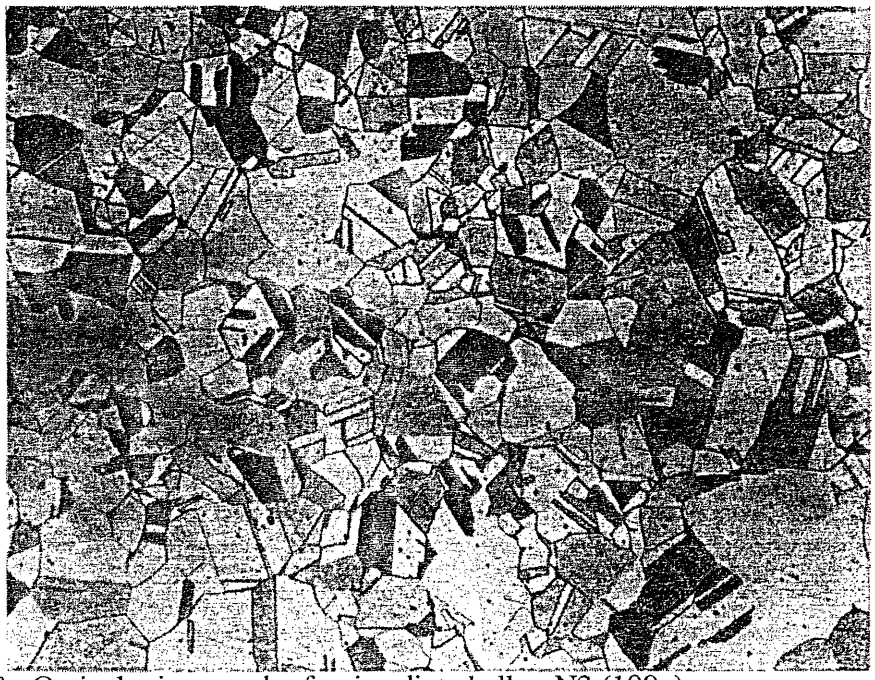

Figure 3.3. Optical micrograph of unirradiated alloy N3 (100x).

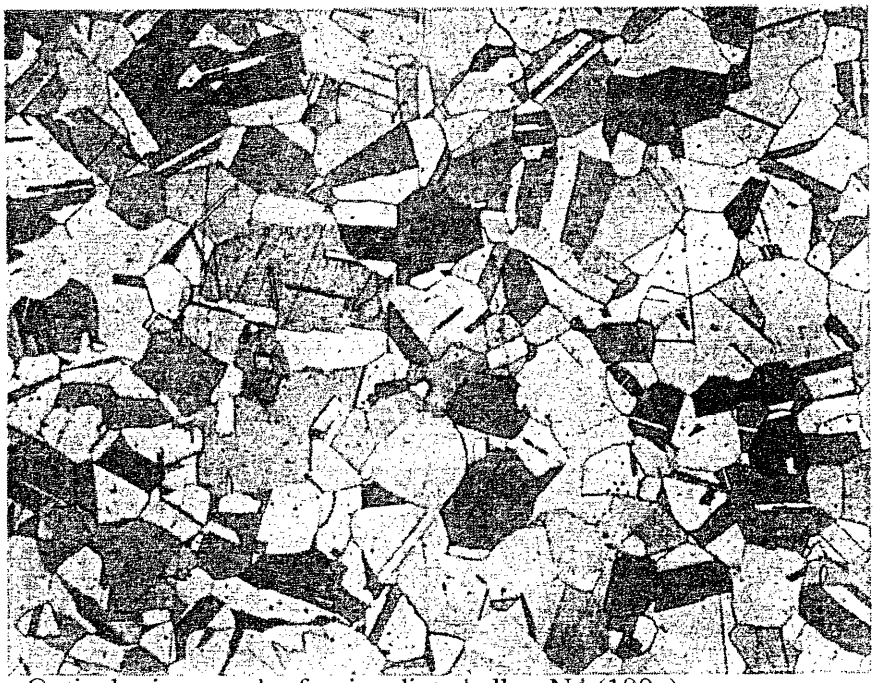

Figure 3.4. Optical micrograph of unirradiated alloy N4 (100x).

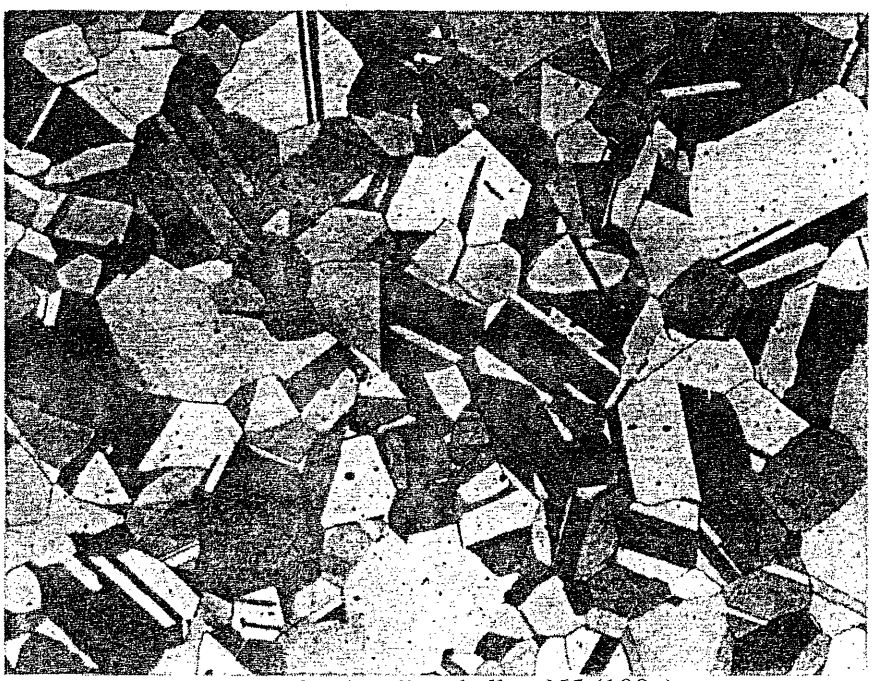

Figure 3.5. Optical micrograph of unirradiated alloy N5 (100x).

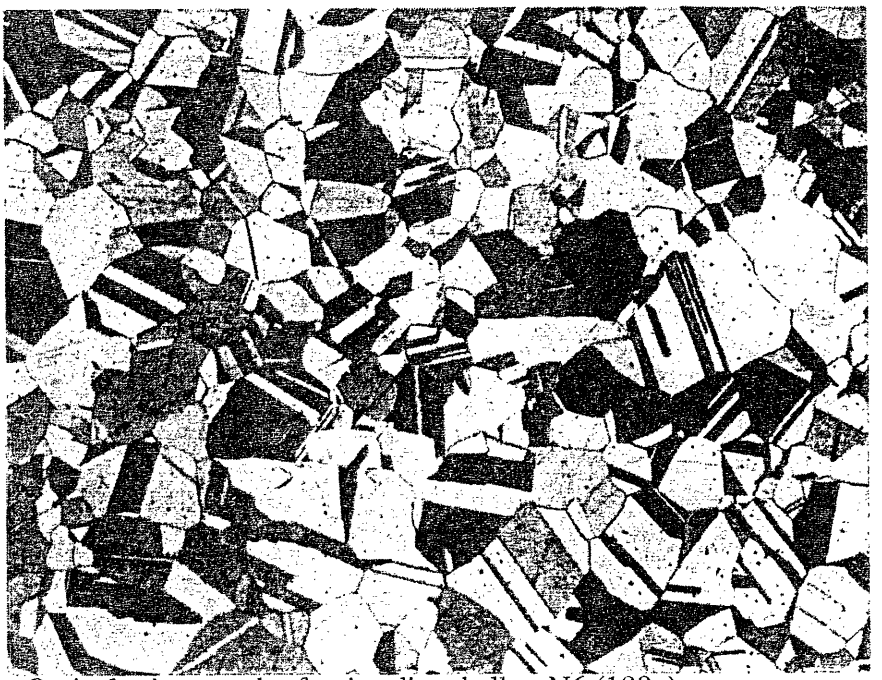

Figure 3.6. Optical micrograph of unirradiated alloy N6 (100x).

Figure 3.7. Optical micrograph of unirradiated alloy N7 (100x).

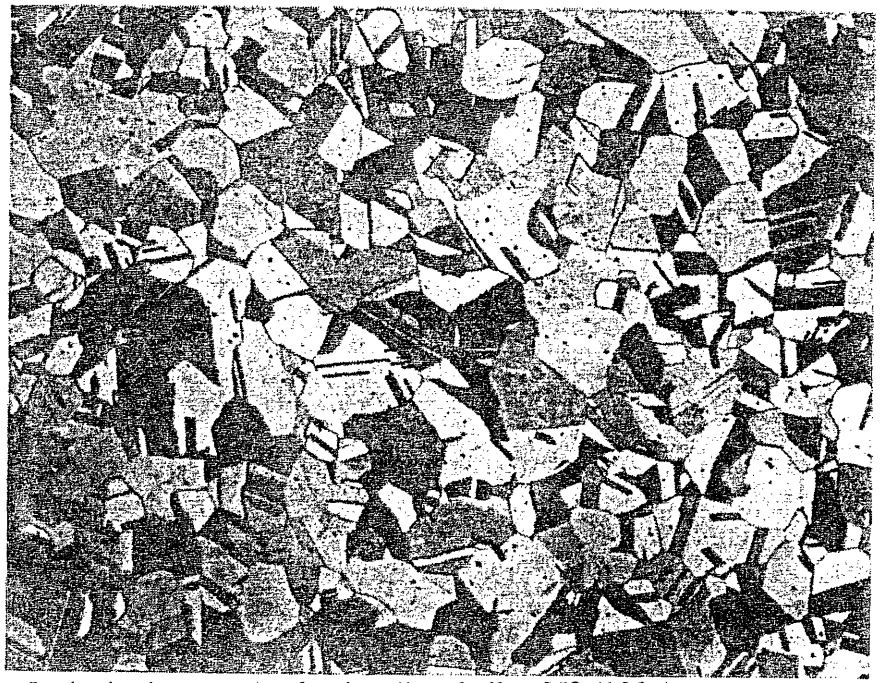

Figure 3.8. Optical micrograph of unirradiated alloy N8 (100x).

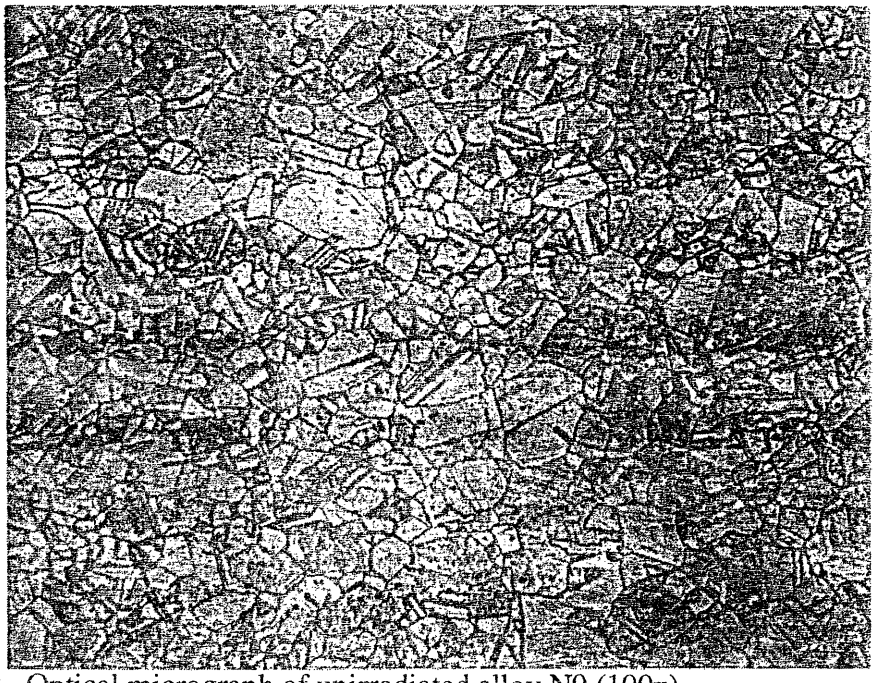

Figure 3.9. Optical micrograph of unirradiated alloy N9 (100x).

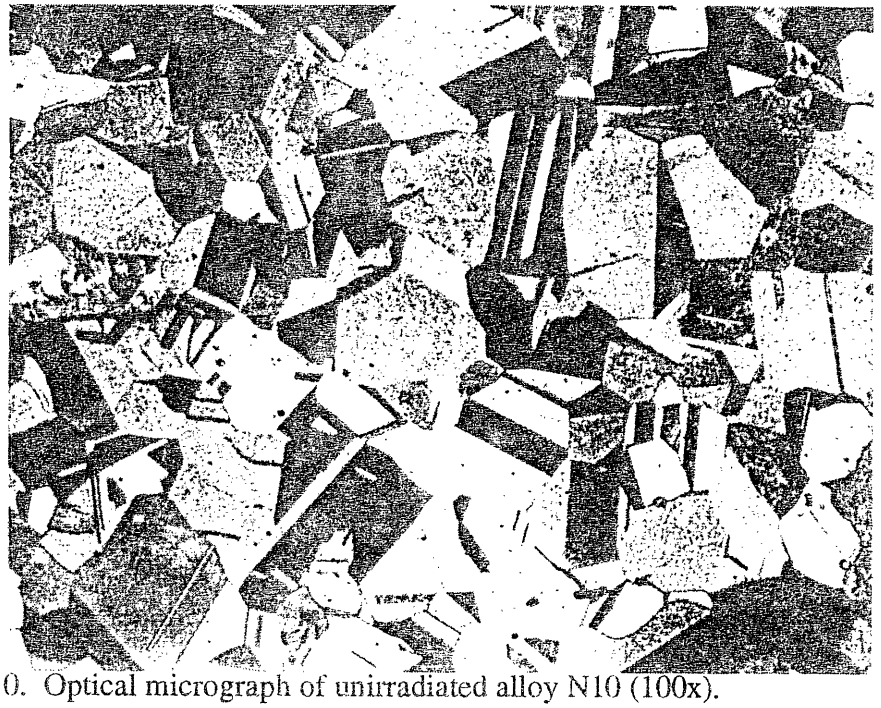

Figure 3.10. Optical micrograph of unirradiated alloy N10 (100x).

Grain size was also calculated from the optical micrographs. This was done by taking a number of measurements on the micrographs in both the X and Y directions along a straight edge. The number of intersections made with visible etched lines were counted, and the distance measured was divided by this number. All boundaries were counted as intersections, even those that appear to be twin boundaries. Approximately fifteen measurements were made on each micrograph, and these numbers were averaged. The results of these calculations are shown in Table 3.2.

Table 3.2. Grain size measurements done on model alloys.

Alloy	Grain Size (μm)
N1	36.75
N2	47.50
N3	44.40
N4	43.90
N5	57.10
N6	43.30
N7	48.50
N8	46.80
N9	33.0
N10	63.1

Crystal structure and the possible presence of phase transformations was also looked for through X-ray diffraction analysis. Square samples of the N1-N10 alloys were cut, solution annealed, and polished to a 6μ finish prior

to analysis. The results indicated that the structure of all 10 alloys was fully austenitic.

3.3 STEM Analysis

At the MIT Electron Microscopy Facility two STEM's were available for the analysis. The first was a VG HB5 150kV STEM and the second was a VG HB603 250kV STEM. Both of these microscopes have a probe size of less than 2nm and are equipped with a Link Systems x-ray detector. All compositional analysis of the model alloys was done by EDX. The level of radioactive decay was small and did not influence the analysis (detector dead time) significantly.

3.3.1. Specimen Preparation for STEM

Before any STEM analysis could begin, the technique used for thinning the specimens had to be perfected and approved by the Reactor Radiation Protection Office (RRPO). A Fischione twin-jet electro-polisher was set up in the perchloric acid hood at the MIT Nuclear Reactor Laboratory (MIT-NRL). Many electrolyte and temperature combinations were used on practice Type-304L TEM specimens until the technique had been perfected. The final combination which gave the best results was an electrolyte that consisted of 375ml ethanol, 87ml H_2O, 125ml $HClO_4$, and 63ml 2-butoxyethanol used at a polishing temperature of -35°C . An acetone and dry-ice combination in conjunction with a temperature controller was used to maintain this temperature, and total polishing time for a specimen that started from a thickness of 10 mils was approximately 60 minutes.

Jet-polishing of the TEM specimens usually occurred the day before the STEM analysis. If a longer delay occurred between sample preparation and

analysis, the sample was ion-milled for one-half hour just prior to the STEM analysis so as to clean the surface.

3.3.2. STEM Results

Before analyzing irradiated specimens, the sensitivity of the STEM analysis technique was tested on a thermally sensitized Type-304L SS sample. This specimen was thermally sensitized at 650°C for 25 hours, and jet-polished in the same manner that was planned for the irradiated specimens. Analysis was done on the HB603, and the results are shown in Figure 3.11. This figure shows the microscope sensitivity to be capable of easily detecting a 1wt% change over a distance of only 5nm.

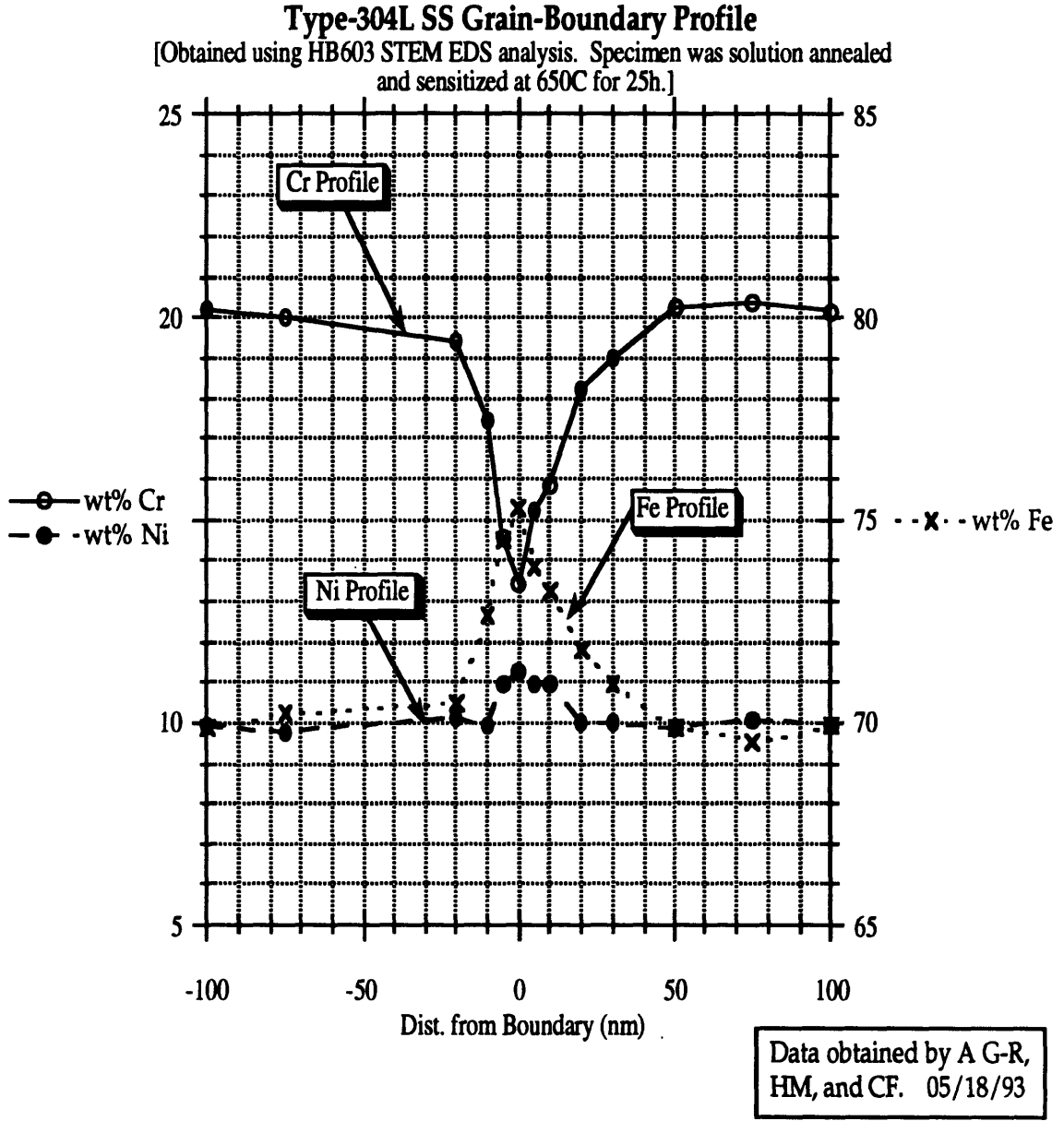

Figure 3.11. STEM-EDX analysis of Type 304 grain boundary.

STEM analysis on all materials took place in the following manner:

1) A grain boundary oriented such that its plane was as close to parallel with beam direction as possible was found. Often this necessitated

specimen tilting, such that the average "effective" width of the analyzed grain boundaries varied from 1nm to 4nm.

2) A background spectrum was taken from the area of the grain boundary being analyzed. This was done with the electron beam off in order to account for the activity of the sample.

3) Spectra were collected in point mode at several locations moving in a perpendicular direction with respect to the grain boundary. Each spectrum was obtained by counting for a total of 75 seconds real time and stopped every 15 seconds to account for drift.

4) Link Systems' software was used to obtain the compositional analysis by subtracting the background from the individual spectra and using corresponding K_α and K-factors for chromium, nickel, and iron.

5) Error analysis for each compositional point was calculated by standard statistical counting techniques.

The results of the STEM analysis on materials N1, N5, N6, N9, and N10 are shown in Figures 3.12 through 3.16. These materials were given priority due to the expectation that the largest degree of grain boundary sensitization would be seen in the materials with the most extreme material compositional differences. Alloy N9 was analyzed as well as alloy N10 because of compositional fluctuations seen in alloy N10 (see Figs. 3.12(a), 3.12(b), and 3.12(c)).

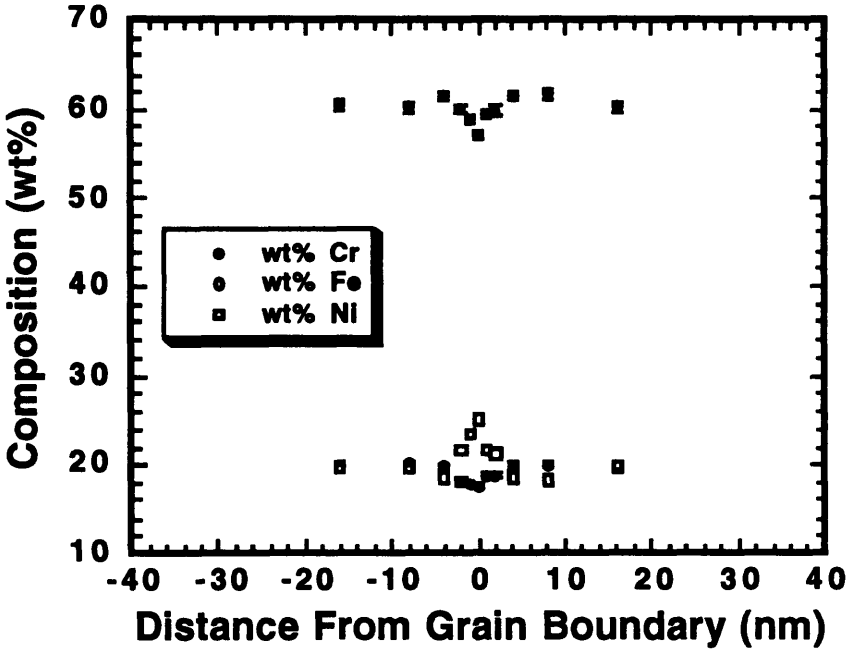

Figure 3.12(a). STEM-EDX grain boundary profile in alloy N1 (Caps4 $0.8 \times 10^{21} n/cm^2$).

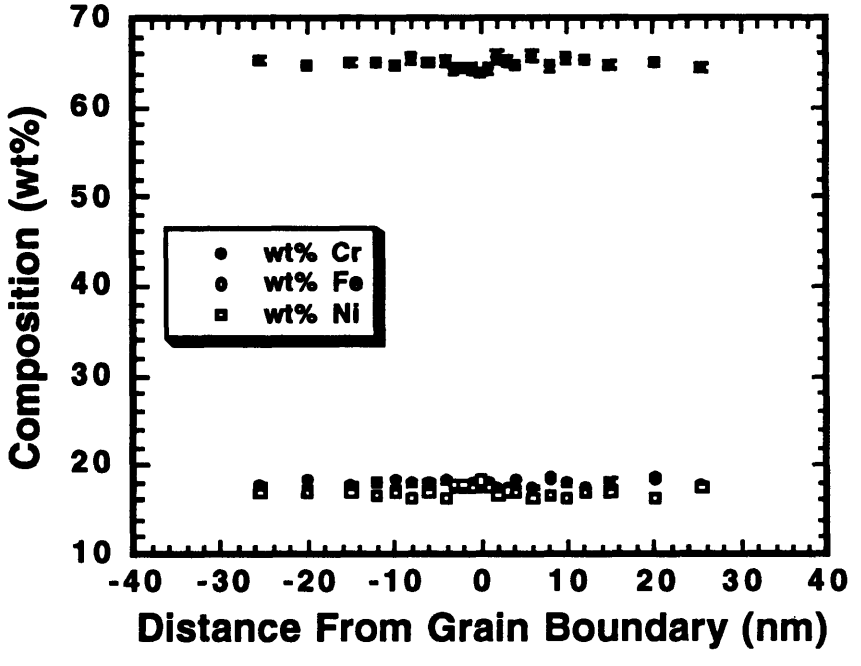

Figure 3.12(b). STEM-EDX grain boundary profile in alloy N1 (Caps4 $0.8 \times 10^{21} n/cm^2$)

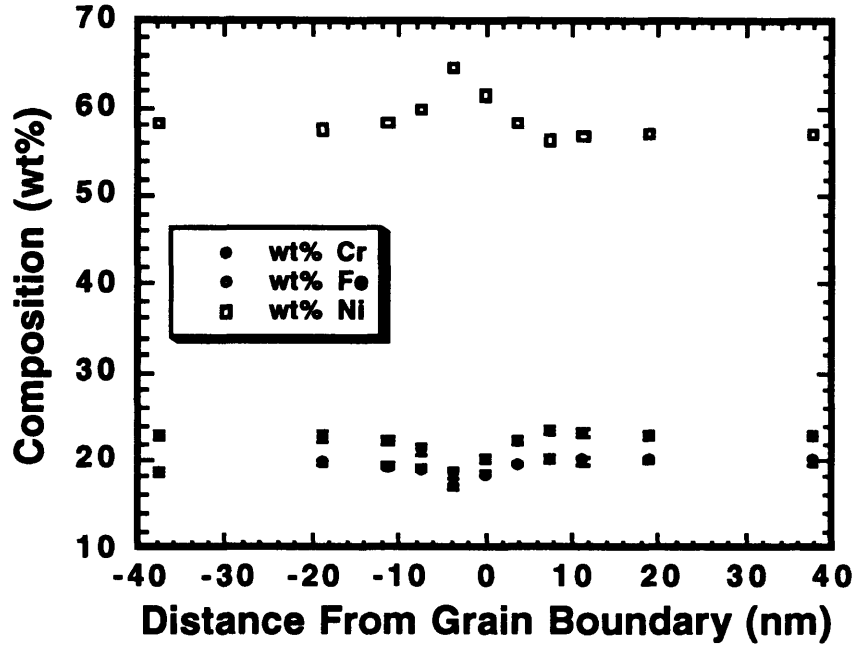

Figure 3.13(a). STEM-EDX grain boundary profile in alloy N5 (Caps4 $0.8 \times 10^{21} n/cm^2$).

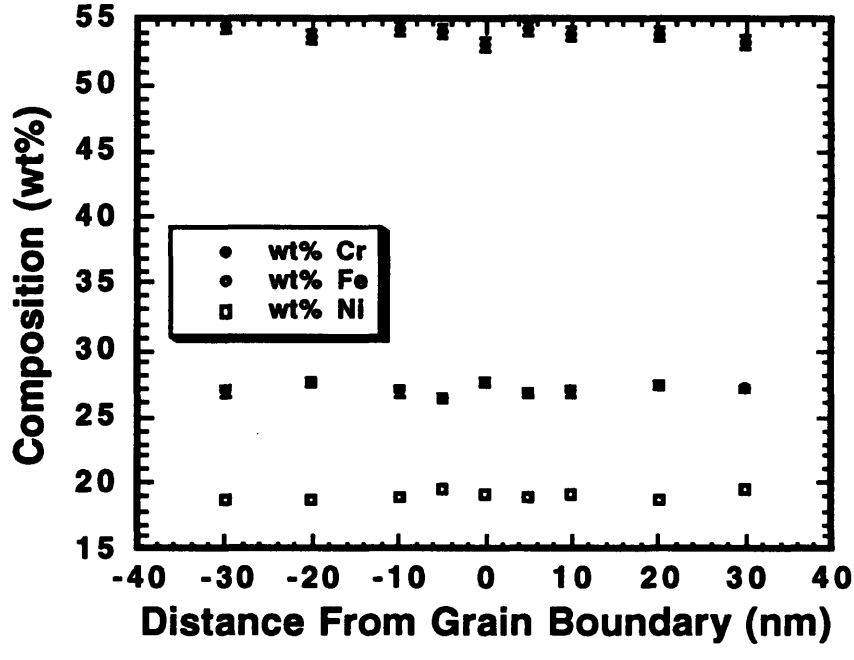

Figure 3.14(a). STEM-EDX grain boundary profile in alloy N6 (Caps3 $0.74 \times 10^{21} n/cm^2$).

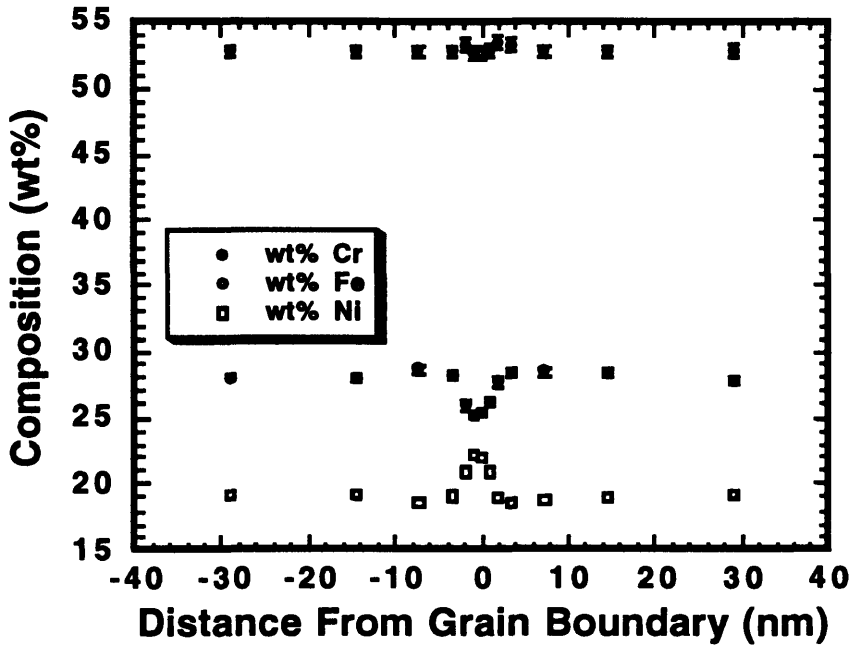

Figure 3.14(b). STEM-EDX grain boundary profile in alloy N6 (Caps3 $0.74 \times 10^{21} n/cm^2$).

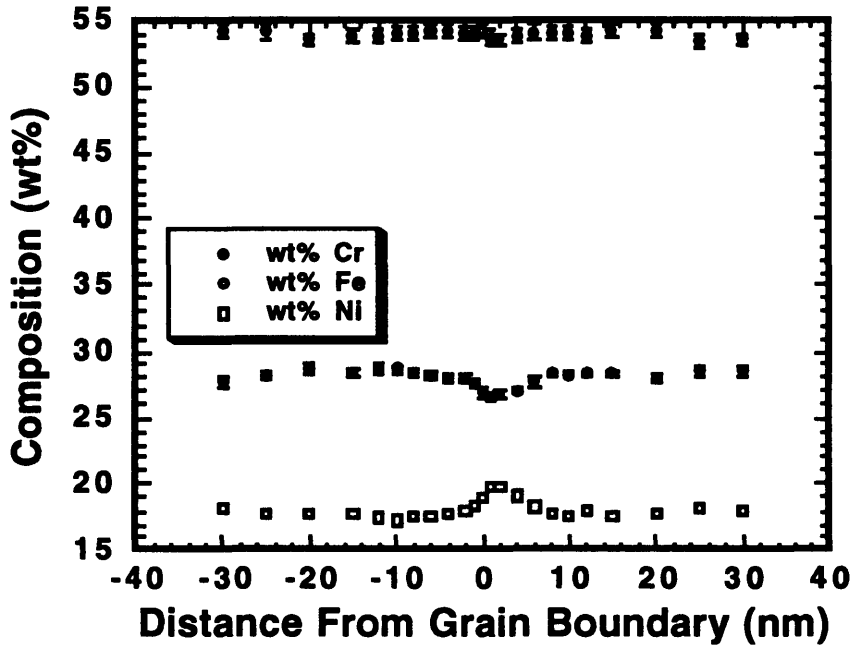

Figure 3.14(c). STEM-EDX grain boundary profile in alloy N6 (Caps3 $0.74 \times 10^{21} n/cm^2$).

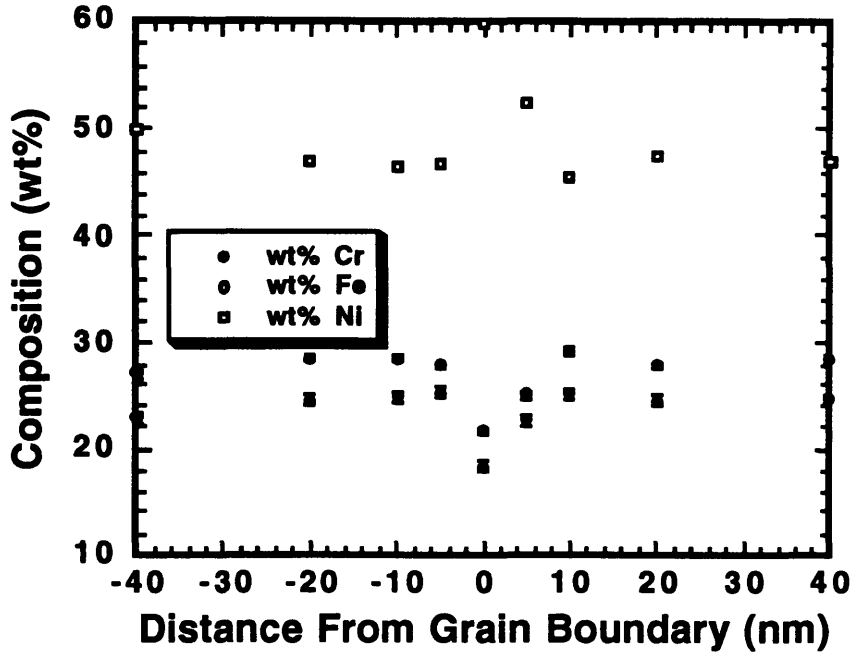

Figure 3.15(a). STEM-EDX grain boundary profile in alloy N9 (Caps4 $0.8 \times 10^{21} n/cm^2$).

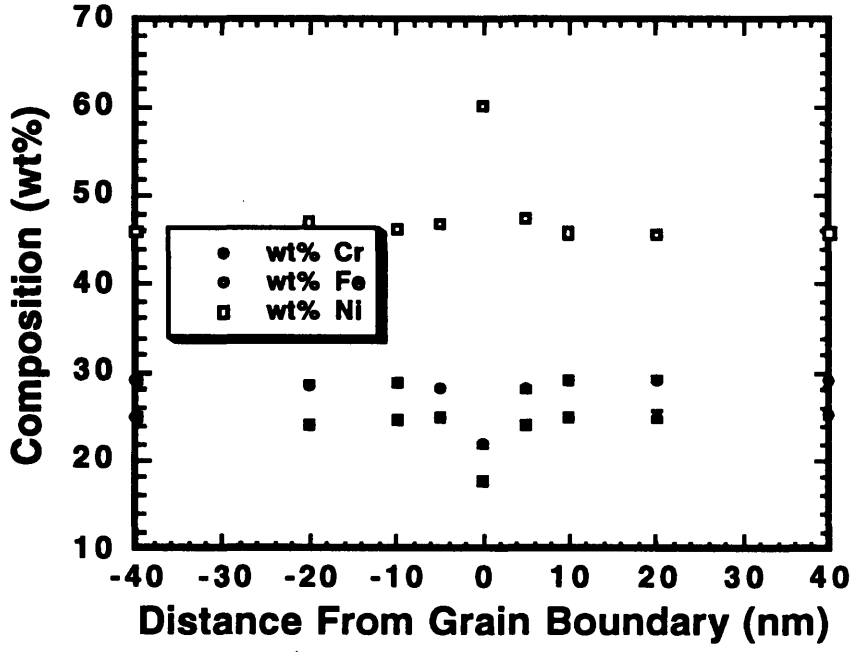

Figure 3.15(b). STEM-EDX grain boundary profile in alloy N9 (Caps4 $0.8 \times 10^{21} n/cm^2$).

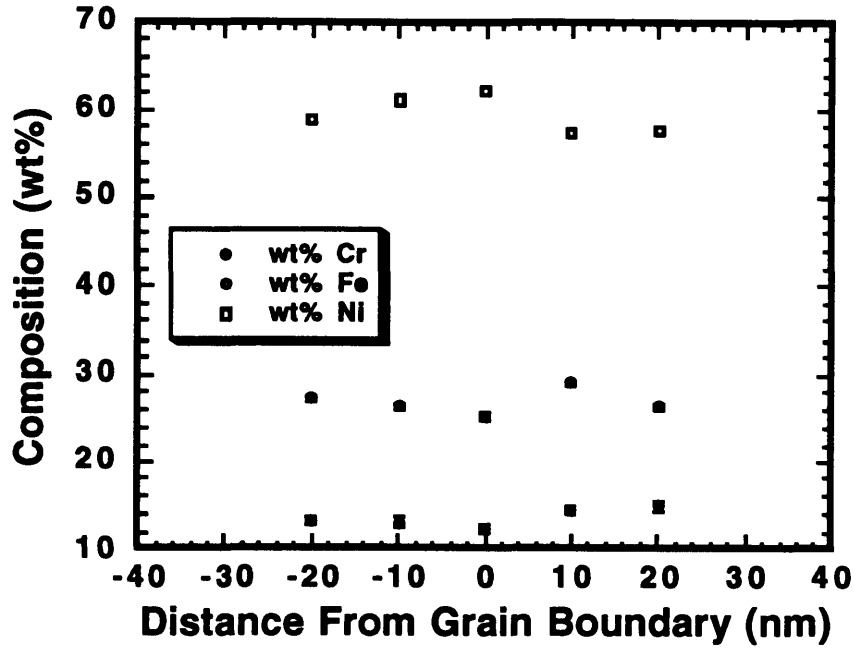

Figure 3.16(a). STEM-EDX grain boundary profile in alloy N10 (Caps4 0.8×10^{21} n/cm^2).

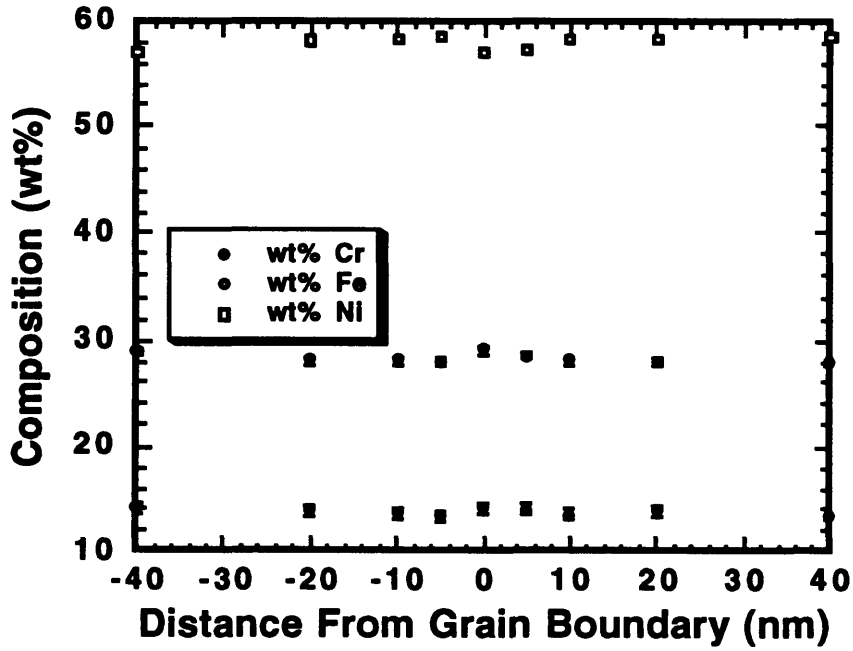

Figure 3.16(b). STEM-EDX grain boundary profile in alloy N10 (Caps5 0.86×10^{21} n/cm^2).

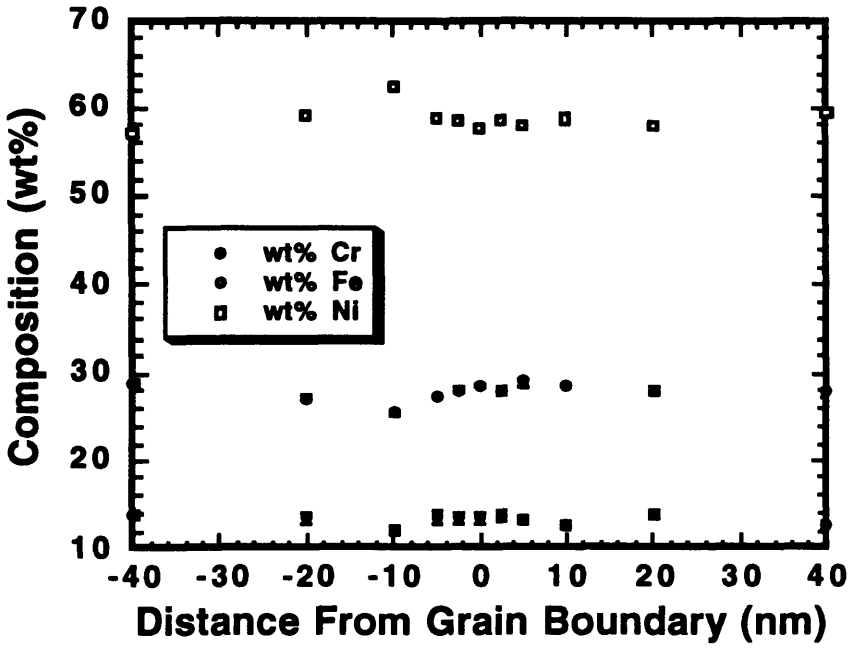

Figure 3.16(c). STEM-EDX grain boundary profile in alloy N10 (Caps5 0.86×10^{21} n/cm^2).

To benchmark the consistency between results from the HB5 and the HB603 a test was performed on two specimens using both microscopes. The same grain boundaries in both a N6 type specimen and a BPV603 (commercial Type-304L SS) specimen were analyzed at adjacent areas. The results are seen in Figure 3.17 and show that both microscopes are equally capable of detecting sensitization if it exists.

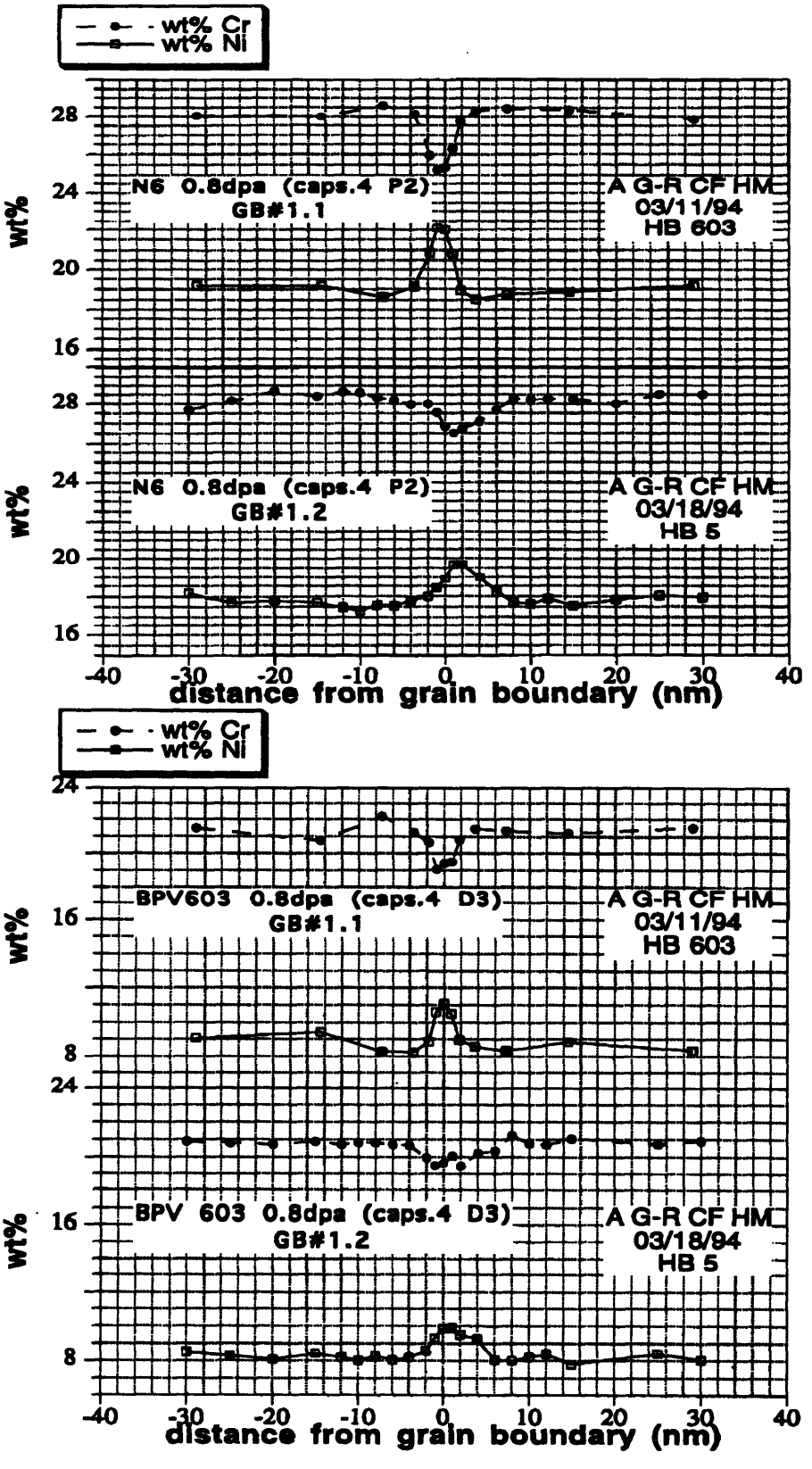

Figure 3.17. Comparison of grain boundary profiles done on the same grain boundaries at adjacent locations by the HB5 and HB603.

3.4. EPR Analysis

Because of the uses of austenitic stainless steels as structural components in nuclear reactors, a non-destructive method for studying the effects of radiation on the grain boundary chemistry was desirable. The fact that the electrochemical properties of such materials are sensitive to microstructural and microchemical changes provides one with several electrochemical materials characterization (EMAC) methods. [8] For the purpose of measuring sensitization and other microchemical changes at grain boundaries, a proven method used on austenitic stainless steels is the double loop electrochemical potentiokinetic reactivation (EPR) technique. [9]

The EPR technique is a non-destructive method used to measure mild degrees of sensitization due to chromium depletion at grain boundaries. In the single loop EPR technique, the degree of sensitization is determined from the charge density of the reactivation scan only. The double loop EPR concept is based upon the phenomena that an oxide film, formed over a depleted chromium region, will preferentially break down while sweeping the potential from the passive to the active region. The EPR ratio is defined as the ratio of the reactivation peak current density and the activation peak current density which then provides the quantitative degree of sensitization. Both techniques have good agreement, but the double loop technique has the advantages over the single loop technique of being more reproducible and less sensitive to variations in scan rate and solution composition. This technique is also independent of surface finish as well as the presence of random pitting. [10] For these reasons, this technique was chosen as the analysis method for this project. It was hoped that this analysis method would provide quantitative information concerning the degree of

sensitization in the various experimental alloys. A schematic detailing the double loop EPR technique is seen in Figure 3.18.

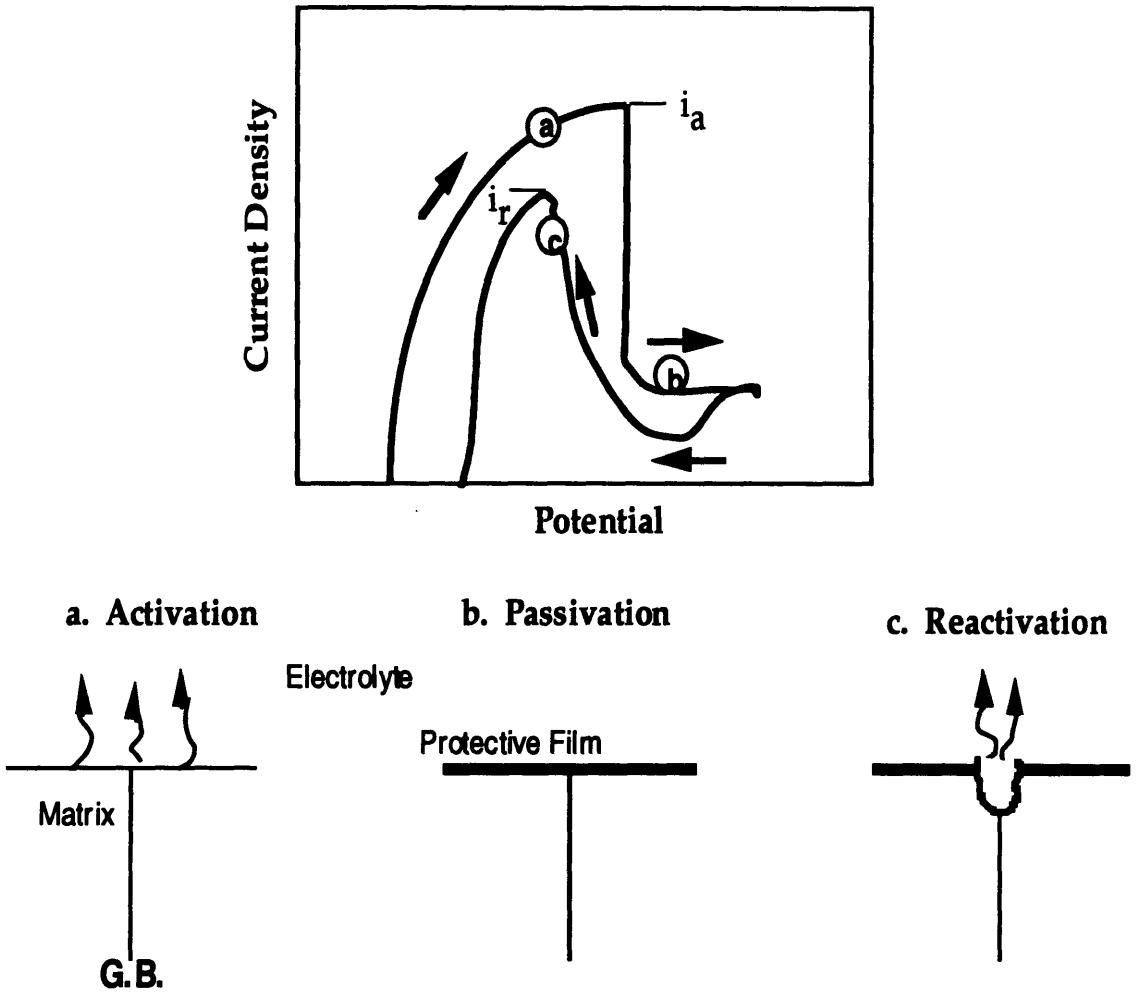

$$\text{EPR Ratio} = i_r / i_a$$

Figure 3.18. Schematic of Double-Loop EPR Analysis

For analysis of the experimental alloys, a modified EPR method was chosen. Due to the relatively high nickel and high chromium content of alloys N6, N9 and N10 and from previous practice tests done with the

standard EPR method on these same alloys, the modified EPR test appeared to give the best results. The procedures used for both the modified EPR (Mod-EPR) and the standard EPR (Std-EPR) test conditions is shown in Table 3.3. It should also be noted that for the Mod-EPR tests, pre conditioning was used to dissolve any oxide layer that formed before initiation of the test. For this case, the test method is referred to as Moc-EPR.

Table 3.3.a. Test conditions for Standard Double Loop EPR.[11]

Electrolyte: 0.5mol/*l* -H_2SO_4 + 0.01mol/*l* -KSCN
Temperature: 30°C
Potential Sweep: Corrosion potential --> 300mV(SCE) --> Corrosion potential
Sweep rate: 100mV/min
Surface finish: SiC paper # 1200 (6μ diamond paste finish)

Table 3.3.b. Test conditions for Modified Double Loop EPR.[12]

Electrolyte: 0.5mol/*l* -H_2SO_4 + 0.1mol/*l* -KSCN
Temperature: 30°C
Potential Sweep: Corrosion potential --> 300mV(SCE) --> Corrosion potential
Sweep rate: 20mV/min
Surface finish: SiC paper # 1200 (6μ diamond paste finish)

(*Moc-EPR uses the same conditions but first prepares the specimen with a 120 second pre-conditioning at 360mV (SHE).)

It was also desired to be able to compare the results with previous EPR testing done by Watanabe [13] of alloy N8 and other commercial alloys. For this reason, no other modifications were done to the EPR test conditions, hence, the only choices available were between the standard or modified versions.

3.4.1. Specimen Preparation for EPR

For EPR analysis of the experimental alloys, TEM specimens of materials N6, N9 and N10 were used. These materials were given highest priority because of their high chromium content. Procedures used for specimen preparation were developed by Watanabe.

Prior to TEM mounting, preparation of the mount occurred by epoxying two lengths of plexi-glass tubing, concentrically, one inside the other. In order to achieve a relatively flat surface, the concentric tubes were placed on a flat teflon block, being extremely careful to get no epoxy in the center hole, and allowed to dry. It was noted through trial and error that any epoxy in the center hole would cause the TEM disc during the mounting process to slant and prohibit it from drying with its surface plane parallel to that of the mount. The importance of this will be discussed later.

Mounting of the TEM disc in a Plexiglas mount took place in the following fashion (see also Figure 3.7):

1) A piece of double-sided tape with a 1cm diameter hole in its center was placed onto a Teflon block. A Plexiglas mount was centered about this hole and pressed onto the tape. In this fashion, the mount was securely fashioned to the Teflon block.
2) The selected TEM specimen was ground on 1200 grit SiC paper to remove any oxide layer that formed during or after the dry-irradiation. This was done remotely by sliding the TEM specimen across the paper with a rubber stopper that was held by pliers.
3) The TEM specimen was cleaned in a beaker full of acetone which was placed in an ultrasonic cleaner.
4) An electrical lead that had been previously prepared from a copper wire wrapped in heat shrink tubing, was also cleaned in acetone and

had a small piece of double-sided conductive aluminum tape placed on its tip.

5) The TEM specimen was then pressed onto the end of the electrical lead and set aside.

6) A polyester resin was prepared and injected into the center hole of the Plexiglas mounts.

7) The TEM specimen was then placed into the mount and allowed to drop to the bottom by the force of gravity. Once the TEM specimen had almost reached the bottom of the mount hole, a small weight was placed on top of the electrical lead, and the specimen was placed under a heat lamp to cure for 3 hours. Extreme care was taken in this step to assure that the TEM remained flat against the Teflon block while curing. This was the reason for the small weight and also the reason why the TEM specimen was not pushed to the bottom of the mount hole. After much trial and error it was seen that rushing this step caused the TEM to become 'cocked' or slanted in the hole. This not only diminished electrical conductance, but also prohibited the next step of polishing a flat surface.

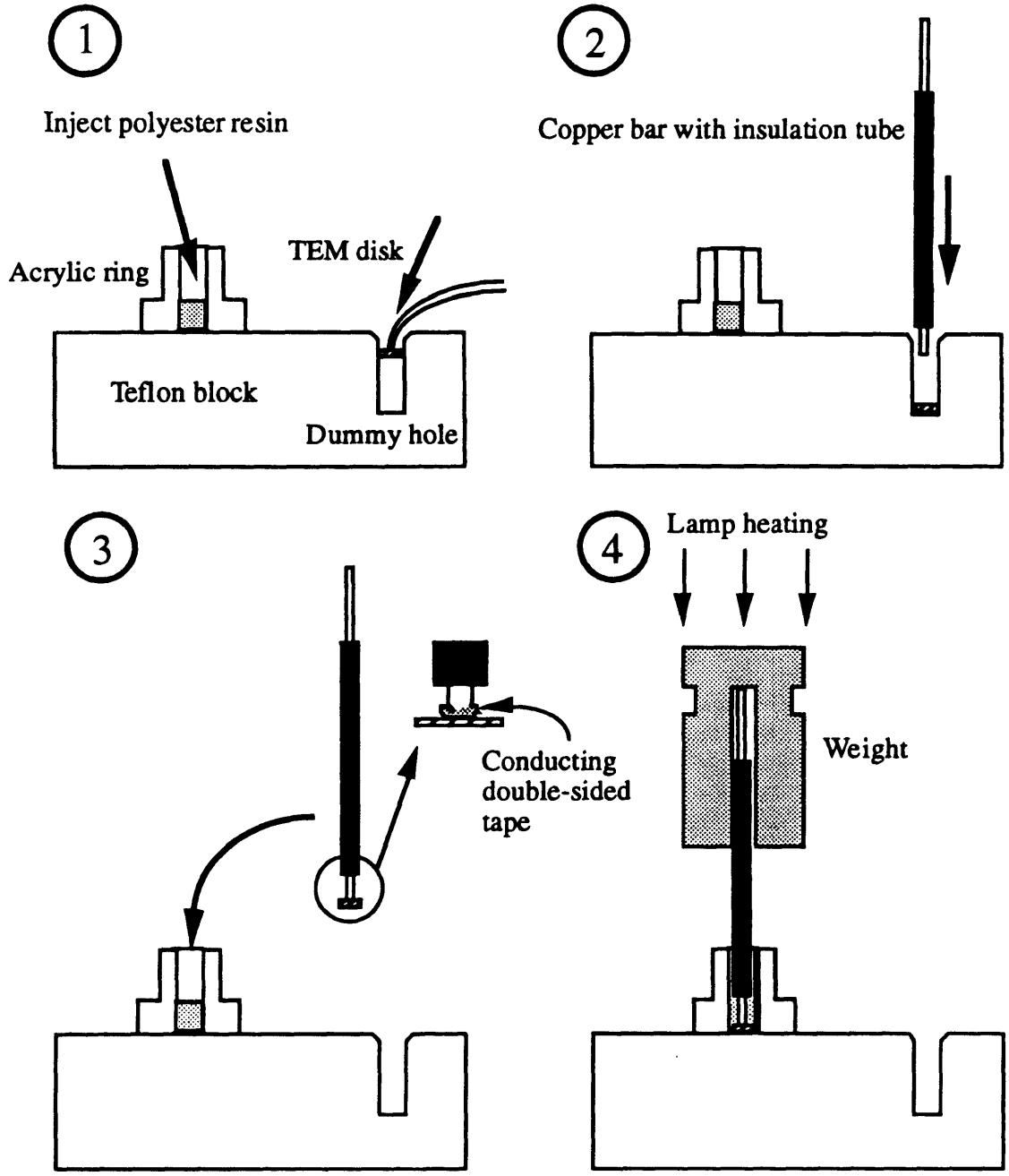

Fig. 3.19. TEM mounting process for EPR testing.[14]

8) Once cured and completely cooled, the mounted specimen was again ground on 1200 grit paper to remove any epoxy from the surface, and electrical conductance was measured to assure a resistance of no more

than 3 ohms. The mounted specimen was then placed in a steel ring-holder and remotely polished with 6μ diamond paste.

9) The mounted TEM specimen was placed in a beaker of isopropyl alcohol and cleaned in an ultrasonic cleaner.

10) After being removed from the isopropyl, the specimen was rinsed one more time by isopropyl alcohol and blown dry with an empty squeeze bottle so as to prevent any film from the isopropyl from forming.

3.4.2. EPR Results

The EPR testing was conducted in a small beaker that was surrounded by a coolant maintained at a constant temperature of 30 $\pm$ 1 °C. The setup for this procedure is shown in Figure 3.20, and the Moc-EPR results from the testing of both non-irradiated and irradiated N6, N9, and N10 TEM specimens are shown in Figure 3.21, Figure 3.22, and Table 3.4.

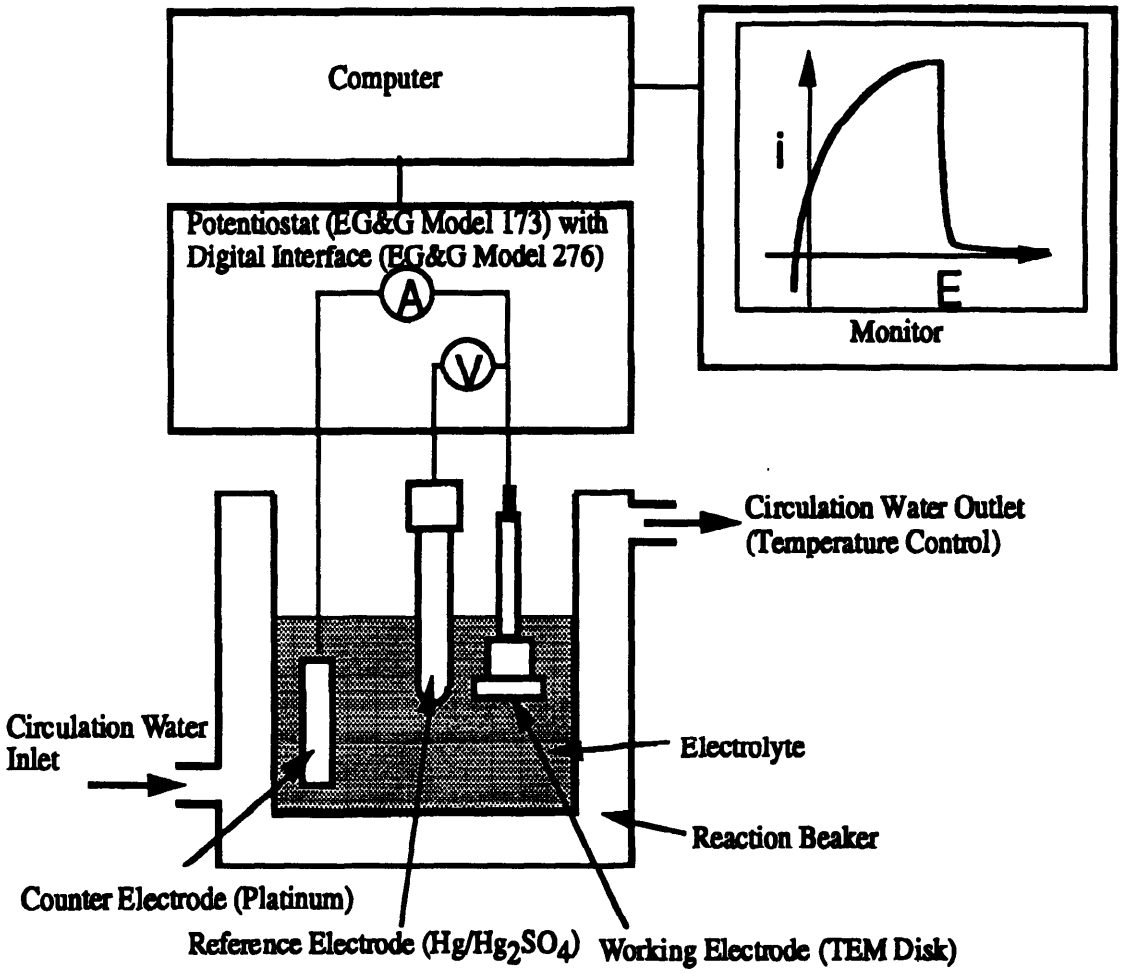

Figure 3.20. EPR testing setup.[15]

EPR testing of non-irradiated TEM specimens of alloys N6, N9 , and N10 occurred in a different laboratory, but under the same environmental conditions. For some of these tests the standard (Std-EPR), modified (Mod-EPR), or modified with pre-conditioning (Moc-EPR) methods were used. These tests were done as practice to determine the best conditions for EPR results from the experimental alloys. Their thermal history, as previously mentioned, is the same as the second batch and should provide reliable data.

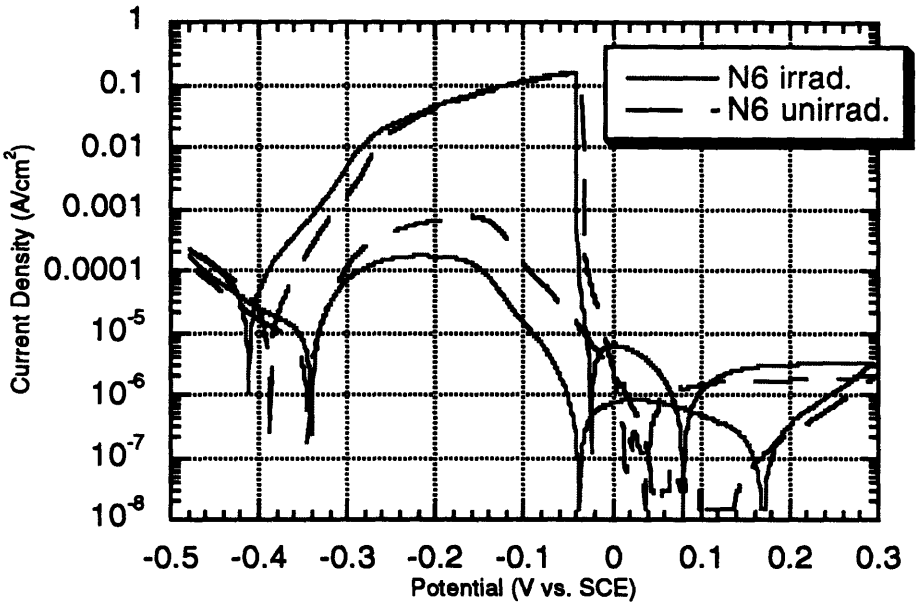
N6 irrad.
N6 unirrad.
Current Density (A/cm²)
1
0.1
0.01
0.001
0.0001
10⁻⁵
10⁻⁶
10⁻⁷
10⁻⁸
-0.5 -0.4 -0.3 -0.2 -0.1 0 0.1 0.2 0.3
Potential (V vs. SCE)

(a)

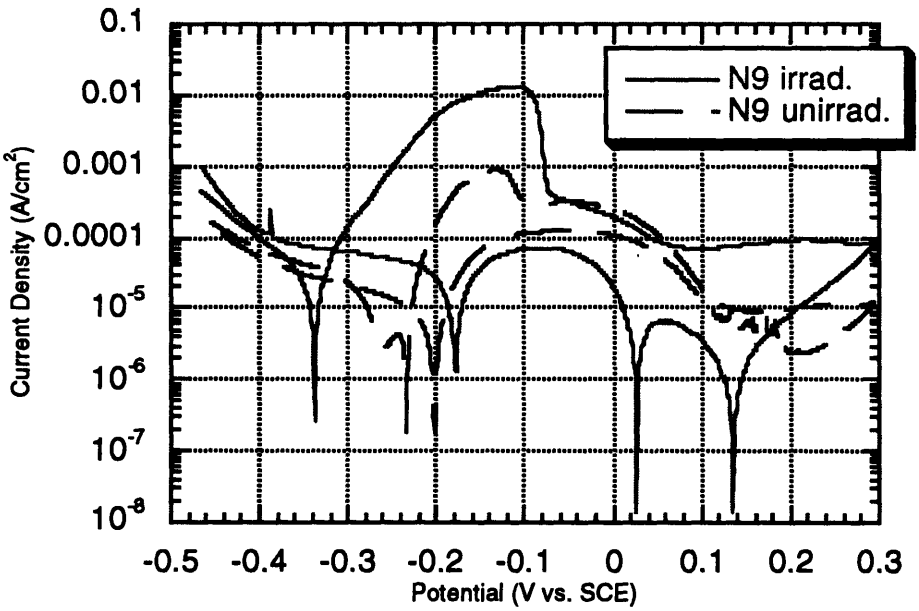
N9 irrad.
N9 unirrad.
Current Density (A/cm²)
0.1
0.01
0.001
0.0001
10⁻⁵
10⁻⁶
10⁻⁷
10⁻⁸
-0.5 -0.4 -0.3 -0.2 -0.1 0 0.1 0.2 0.3
Potential (V vs. SCE)

(b)

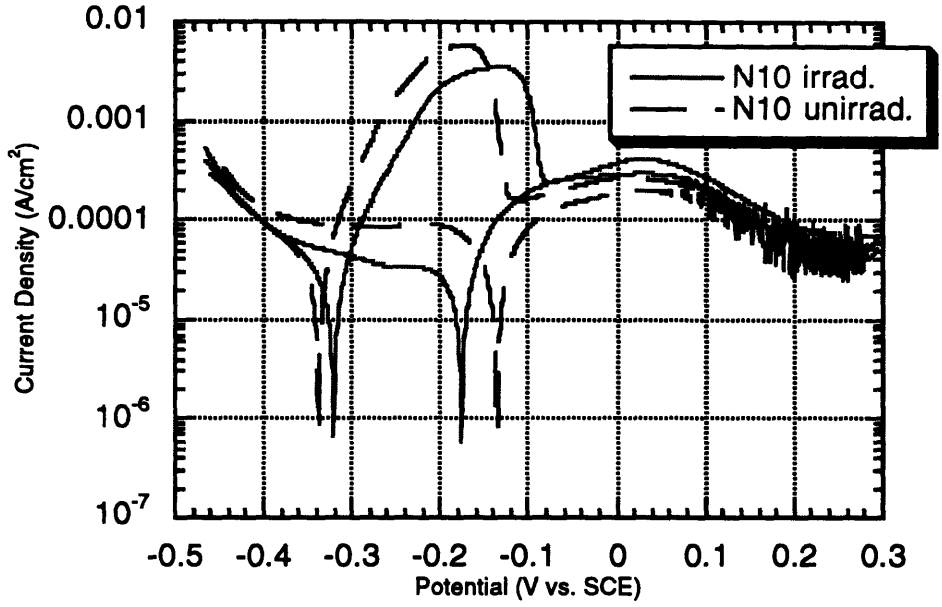

(c)

Figure 3.21: EPR data obtained by using the modified double-loop method with pre-conditioning. (a) Model Alloy N6 irradiated and unirradiated TEM specimens, (b) Model Alloy N9 irradiated and unirradiated TEM specimens, (c) Model Alloy N10 irradiated and unirradiated TEM specimens.

In some of the above EPR data, one will notice the presence of two activation peaks and sometimes two reactivation peaks in the alloy N9 and alloy N10 tests. After initial tests this was a major point of concern because it was thought that there was a lack of repeatability. This concern was alleviated by running tests on several N6 TEM specimens and achieving excellent repeatability. The results are therefore believed to be valid, and the presence of the two activation peaks will be discussed in detail in a later section. The peak with a higher current density value (also the one which has a higher absolute value of potential) will subsequently be referred to as the first or primary peak. The other peak will be referred to as the second or secondary

peak. This will be important in the following table and figures and in the later section that discusses the presence of two peaks.

Alloy	EPR Ratio (%) (unirradiated TEM specimen)	EPR Ratio (%) (irradiated TEM specimen) [Capsule #]	EPR Test Conditions
N1	0.604! 0.826!	6.57![#3]	Std-EPR
N6	0.484	0.112[#3]	Moc-EPR
N8	0.0+!	0.25![#3]	Mod-EPR
N9	13.9* (first peak) 37.9* (second peak)	0.539[#4]	Moc-EPR
N10	0.0*+ (first peak) 73.6* (second peak)	0.0*+[#3] (first peak) 70.1*[#3] (second peak)	Moc-EPR

* Two activation peaks seen during potential sweep.
+ No reactivation peak seen during potential sweep.
! Test performed by Dr. Y. Watanabe.[16]

Table 3.4. EPR results of irradiated and non-irradiated second batch specimens. For each alloy, the results listed (except those performed by Watanabe) are from a single specimen and come from the same potential sweep.

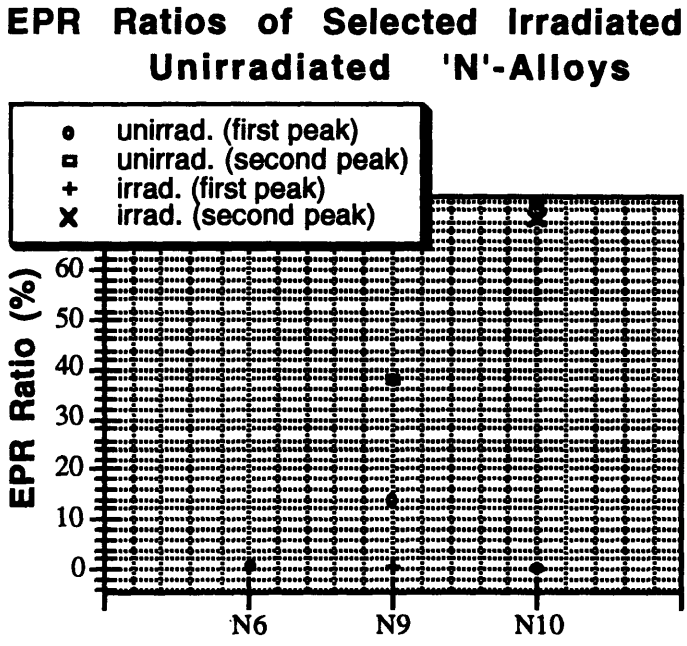

(a)

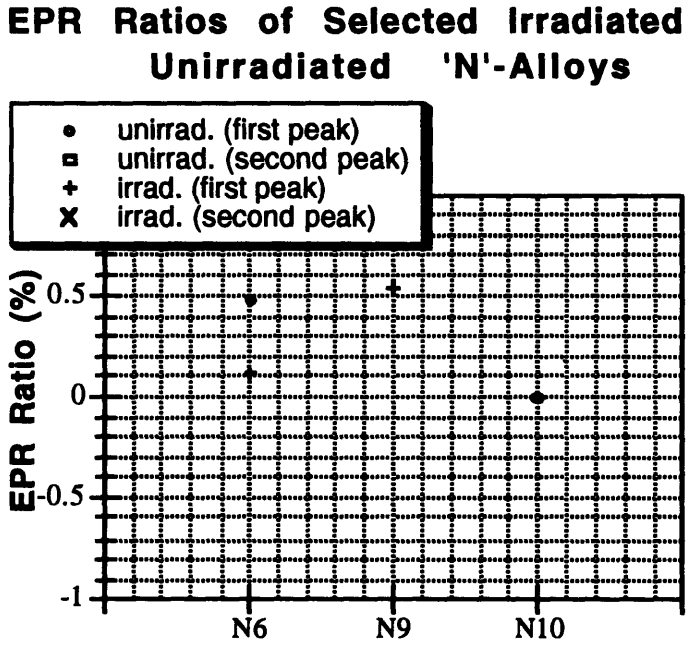

(b)

Figure 3.22. Moc-EPR results. Fig. 3.22.a. is a summary of the results obtained with the second batch of TEM specimens, both irradiated and unirradiated. Fig. 3.22.b. is a summary of the same results, but shows more detail with respect to the lesser value EPR ratios.

For comparison, the EPR results of alloys N1 and N8 done by Watanabe, are shown in Table 3.4. The same preparation techniques were used, and the test conditions are noted. In Figure 3.22, only the alloy N8 results obtained by Dr. Y. Watanabe are shown. All other results were obtained by using the Mod-EPR technique with the above-mentioned pre-conditioning.

The following SEM micrographs which are shown in Figures 3.23 through 3.25 show the surfaces of the alloy N6, N9 and N10 specimens after testing. They include both the irradiated and the unirradiated specimens. It should also be noted that the some of the labels refer to 'light' or 'dark' regions. These regions are shown in the micrographs taken at lower magnifications. This is true for those micrographs of alloys N9 and N10, and is due to the apparent differences in corrosion processes at different regions of the surface.

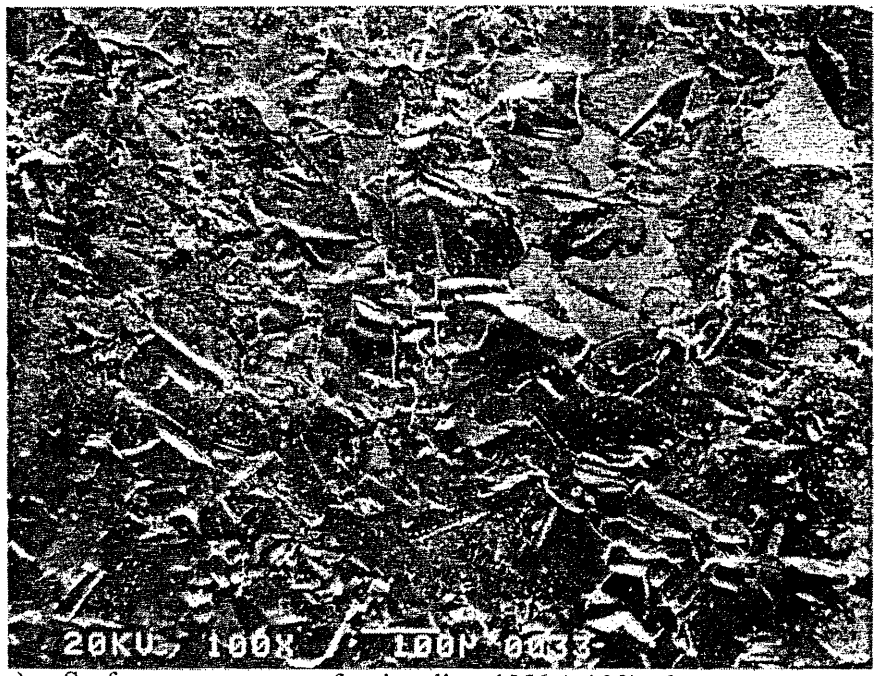

Fig. 3.23(a). Surface appearance of unirradiated N6 (x100) after exposed to Moc-EPR. [EPR ratio: 0.484%]

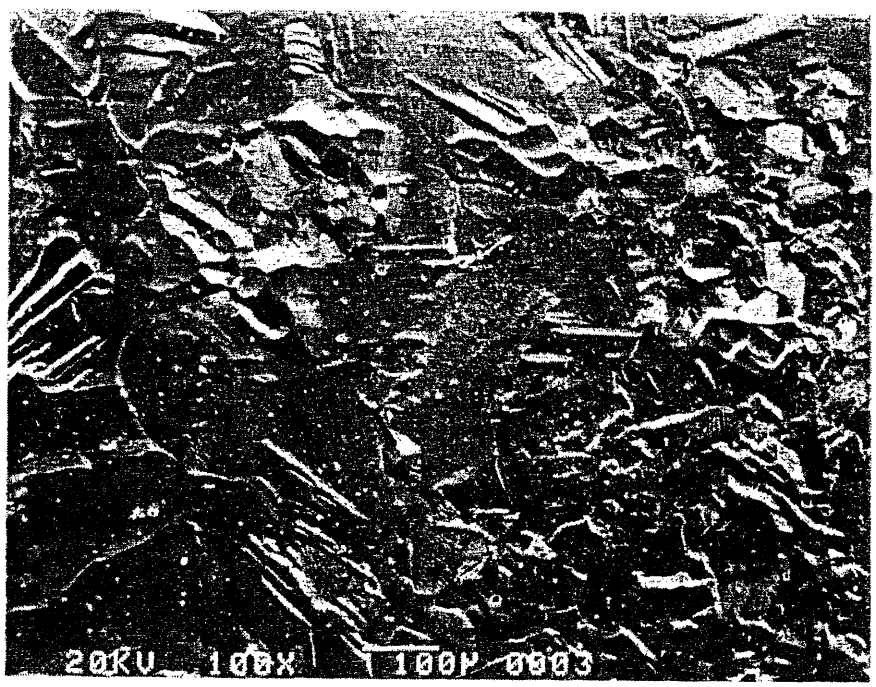

Fig. 3.23(b). Surface appearance of irradiated N6 (x100) after exposed to Moc-EPR. [EPR ratio: 0.112%]

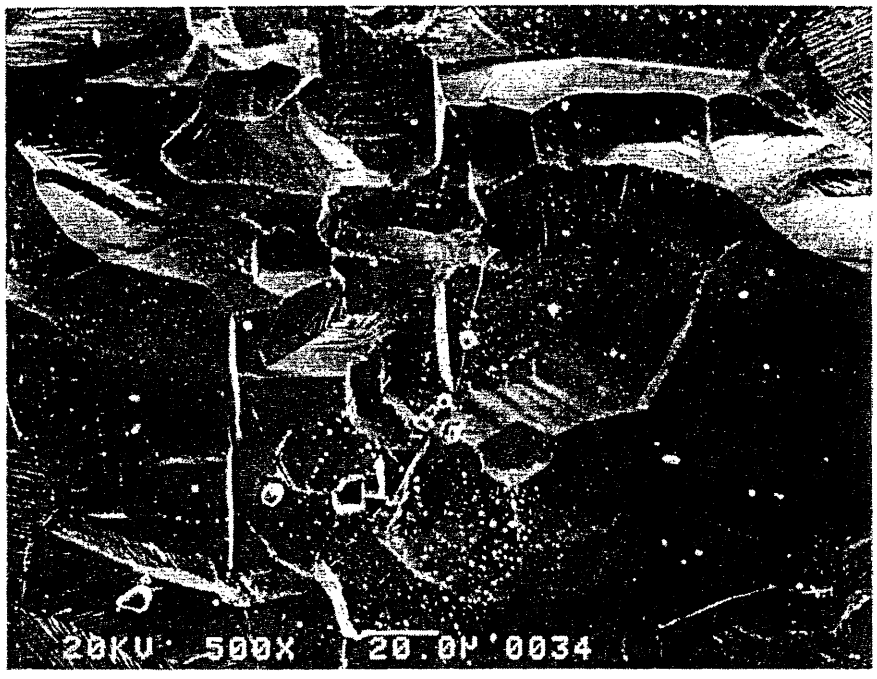

Fig. 3.23(c). Surface appearance of unirradiated N6 (x500) after exposed to Moc-EPR. [EPR ratio: 0.484%]

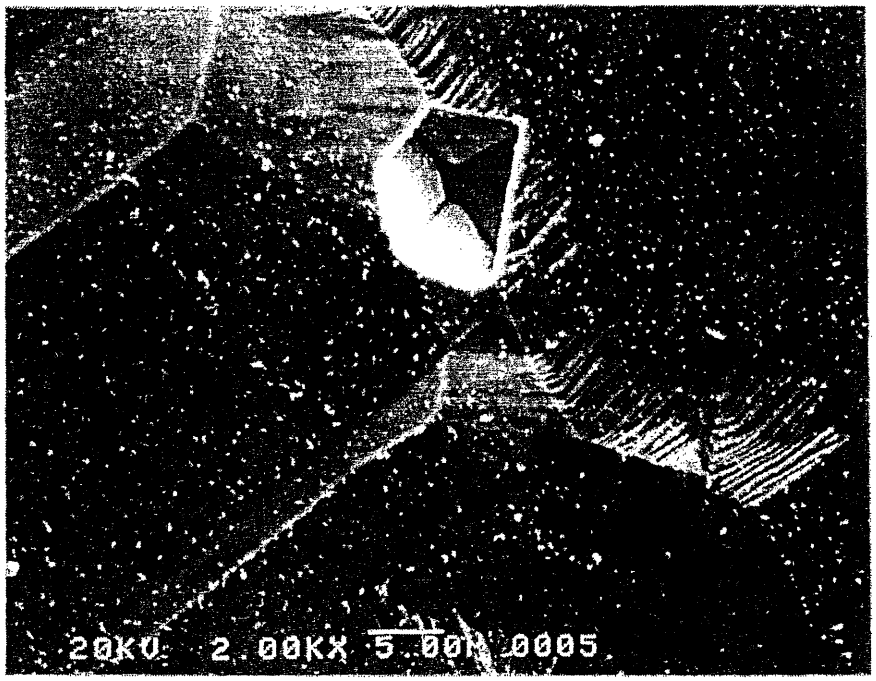

Fig. 3.23(d). Surface appearance of irradiated N6 (x2000) after exposed to Moc-EPR. [EPR ratio: 0.112%]

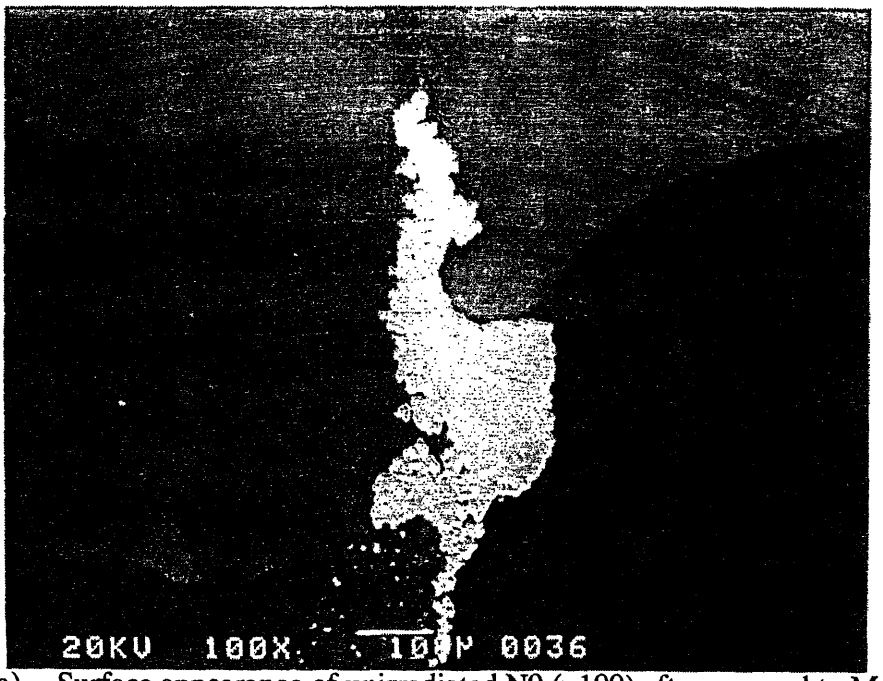

Fig. 3.24(a). Surface appearance of unirradiated N9 (x100) after exposed to Moc-EPR. [EPR ratio: 13.9% (first peak) and 37.9% (second peak)]

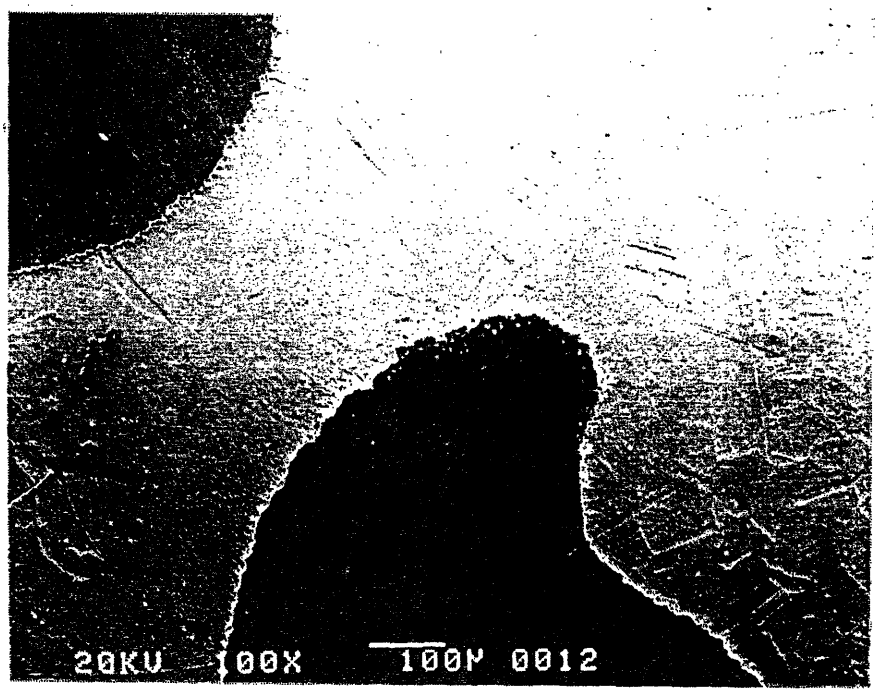

Fig. 3.24(b). Surface appearance of irradiated N9 (x100) after exposed to Moc-EPR. [EPR ratio: 0.539%]

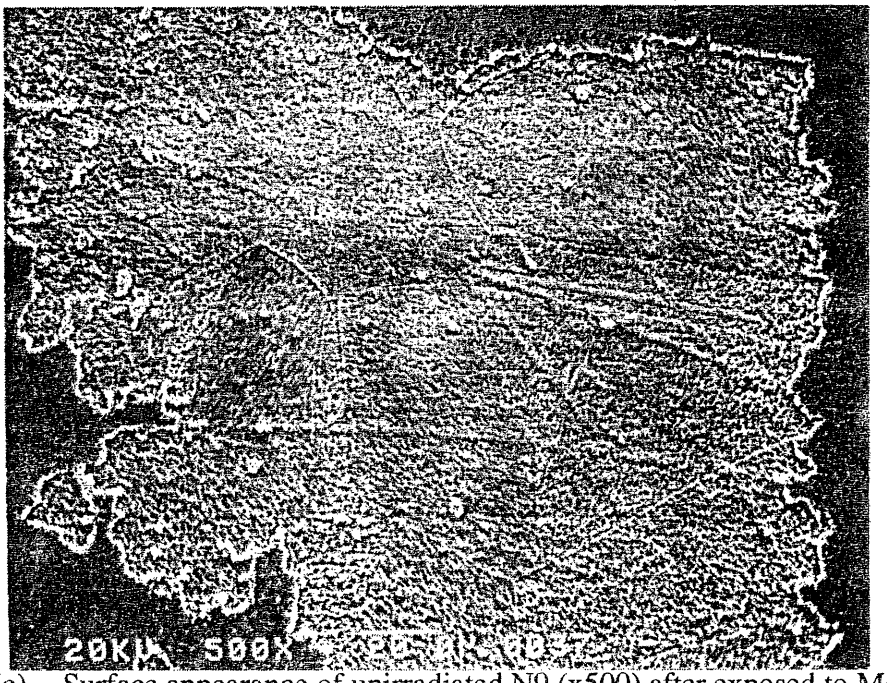

Fig. 3.24(c). Surface appearance of unirradiated N9 (x500) after exposed to Moc-EPR. [EPR ratio: 13.9% (first peak) and 37.9% (second peak)]

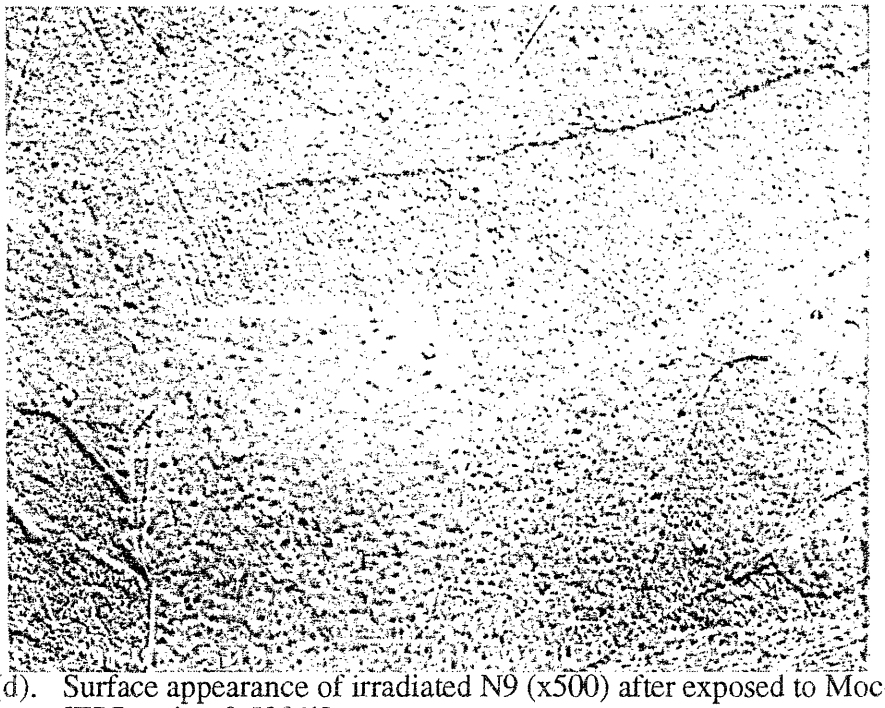

Fig. 3.24(d). Surface appearance of irradiated N9 (x500) after exposed to Moc-EPR. [EPR ratio: 0.539%]

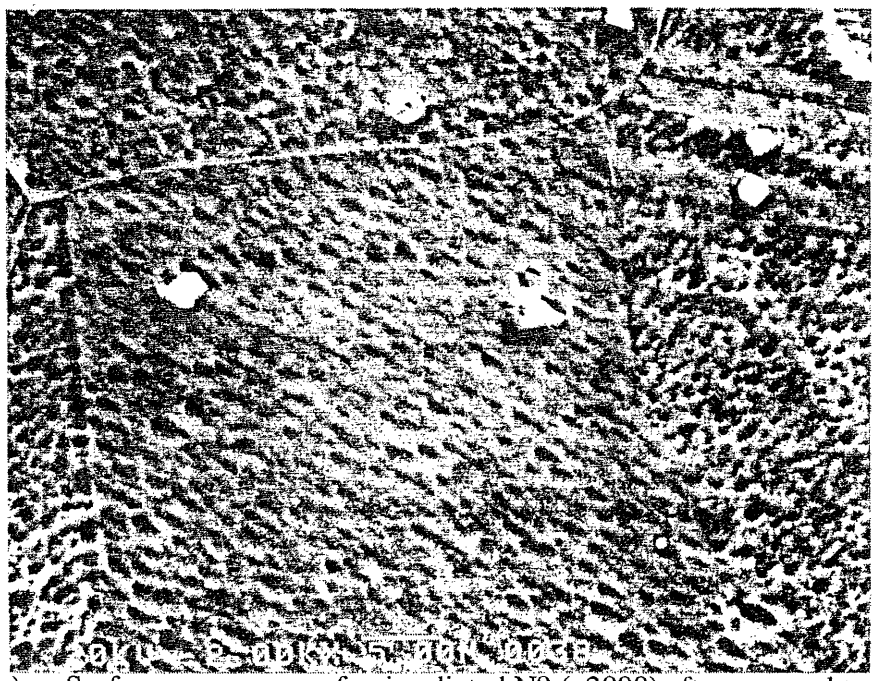

Fig.3.24(e). Surface appearance of unirradiated N9 (x2000) after exposed to Moc-EPR. The lighter tone region as seen in the above lower-magnification micrographs is shown here.
[EPR ratio: 13.9% (first peak) and 37.9% (second peak)]

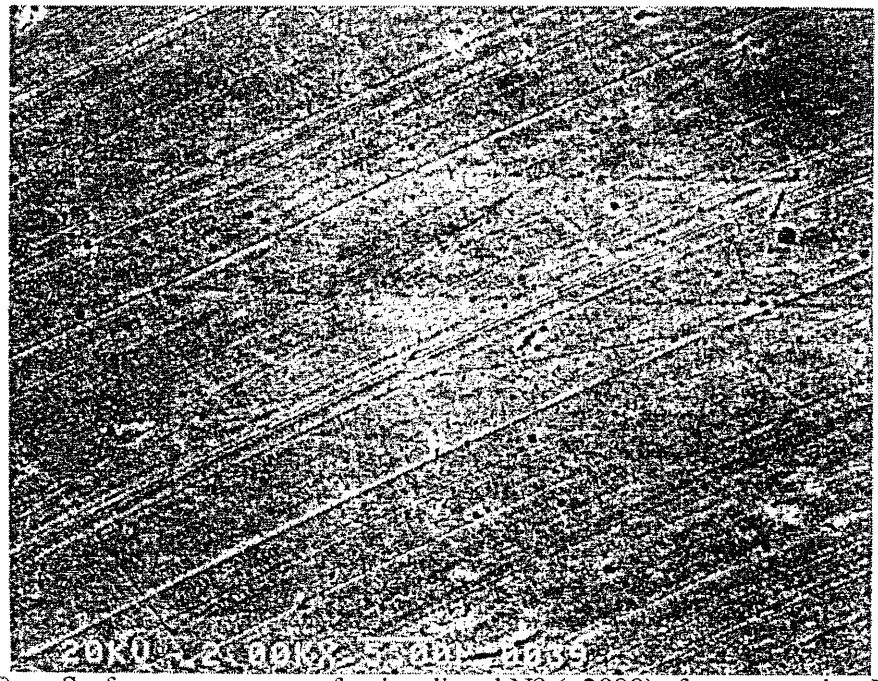

Fig.3.24(f). Surface appearance of unirradiated N9 (x2000) after exposed to Moc-EPR. The darker tone region as seen in the above lower-magnification micrographs is shown here.
[EPR ratio: 13.9% (first peak) and 37.9% (second peak)]

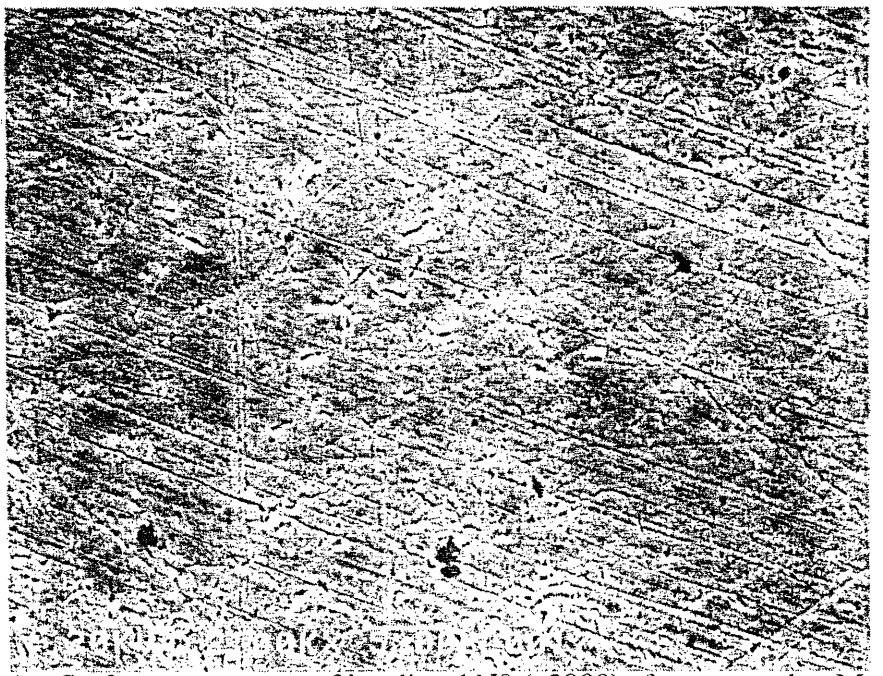

Fig. 3.24(g). Surface appearance of irradiated N9 (x2000) after exposed to Moc-EPR. The darker tone region as seen in the above lower-magnification micrographs is shown here.
[EPR ratio: 0.539%]

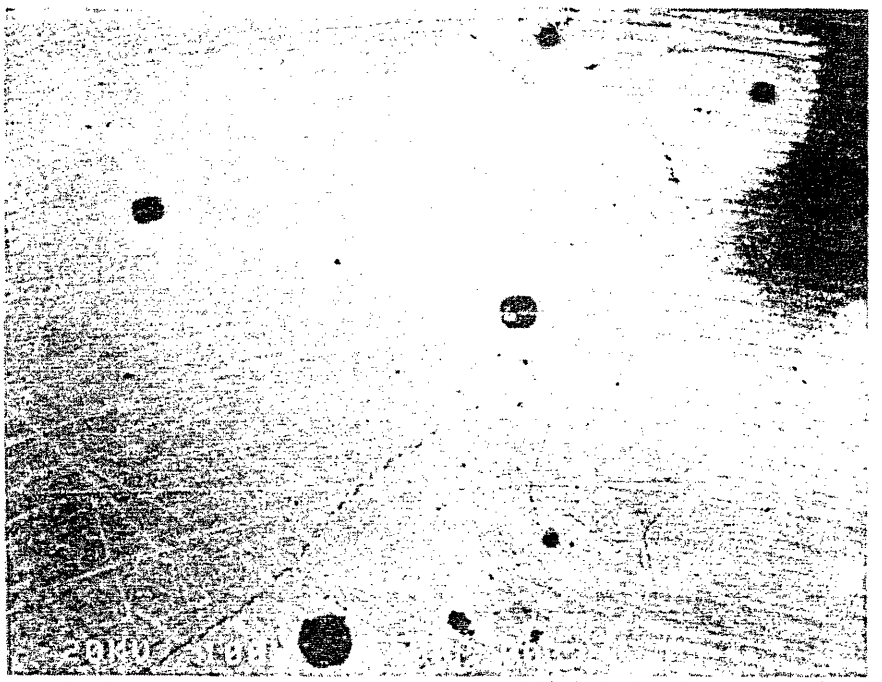

Fig. 3.25(a). Surface appearance of unirradiated N10 (x100) after exposed to Moc-EPR.
[EPR ratio: 0.0% (first peak) and 73.6% (second peak)]

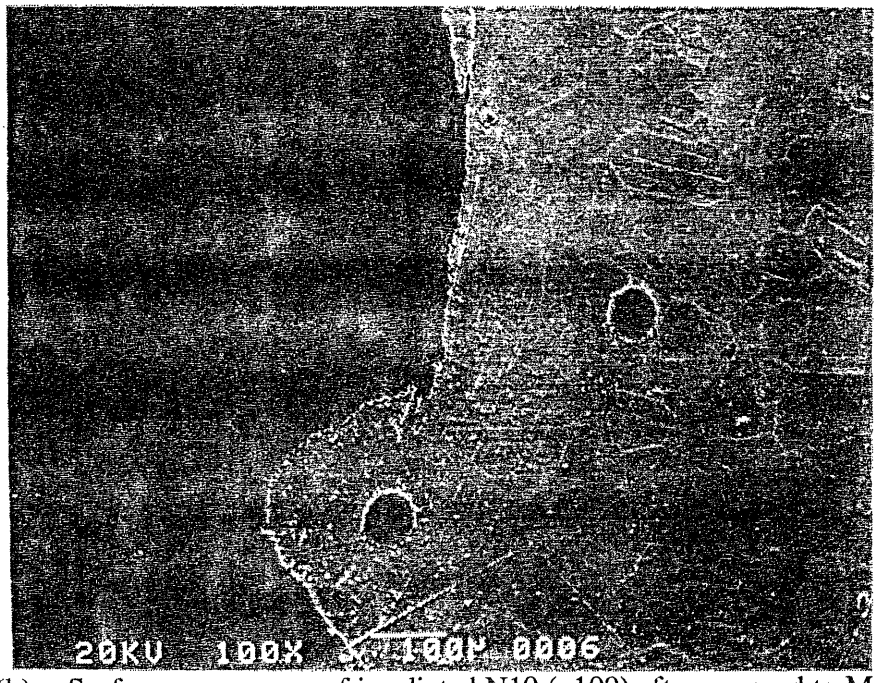

Fig. 3.25(b) Surface appearance of irradiated N10 (x100) after exposed to Moc-EPR.
[EPR ratio: 0.0% (first peak) and 70.1% (second peak)]

Fig. 3.25(c). Surface appearance of unirradiated N10 (x500) after exposed to Moc-EPR.
The lighter tone region as seen in the above lower-magnification micrographs is shown here.
[EPR ratio: 0.0% (first peak) and 73.6% (second peak)]

Fig. 3.25(d). Surface appearance of irradiated N10 (x500) after exposed to Moc-EPR. The lighter tone region as seen in the above lower-magnification micrographs is shown here.
[EPR ratio: 0.0% (first peak) and 70.1% (second peak)]

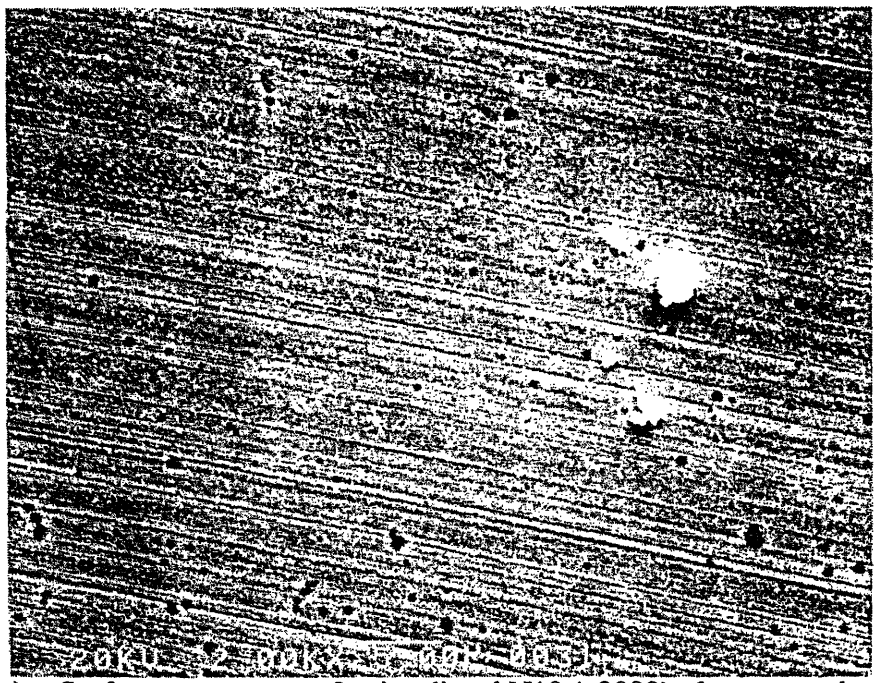

Fig. 3.25(e). Surface appearance of unirradiated N10 (x2000) after exposed to Moc-EPR. The darker tone region as seen in the above lower-magnification micrographs is shown here.
[EPR ratio: 0.0% (first peak) and 73.6% (second peak)]

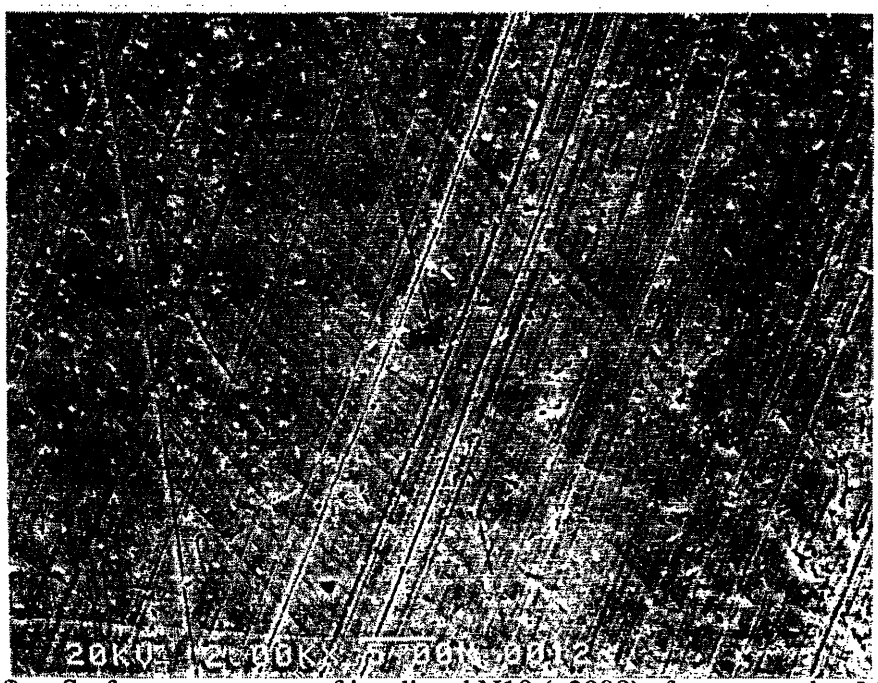

Fig. 3.25(f). Surface appearance of irradiated N10 (x2000) after exposed to Moc-EPR. The darker tone region as seen in the above lower-magnification micrographs is shown here.
[EPR ratio: 0.0% (first peak) and 70.1% (second peak)]

3.5. References:

1. Stephen T. Boerigter, "An Investigation of Neutron-Induced Segregation in Austenitic Stainless Steels", PhD Thesis, Dept. of Nucl Eng., M.I.T., (December 1992).

2. Boerigter, PhD Thesis, (December 1992).

3. Boerigter, PhD Thesis, (December 1992).

4. Boerigter, PhD Thesis, (December 1992).

5. Boerigter, PhD Thesis, (December 1992), pp. 56-57.

6. Majidi A.P. and Streicher, M.A. (1993) "Nondestructive Electrochemical Tests for Detecting Sensitization in AISI 304 and 304L Stainless Steels", pp. 217-228.

7. Petzow G., Metallographic Etching, American Society for Metals, Metals Park, Ohio, (1978).

8. Watanabe, Y.W., "Application of Electrochemical Methods for Characterization of Grain Boundary Microchemistry in Irradiated Austenitic Stainless Steels", Memo to IASCC Project Research Group, MIT, July, 1993.

9. Majidi A.P. and Streicher, M.A. (1984) "The Double Loop Reactivation Method for Detecting Sensitization in AISI 304 Stainless Steels", *Corrosion*, NACE, Vol. 40, No. 11, pp. 584-593, and Iwabuchi, Fujimoto, Watanabe, and Shoji, (1993) "Fundamental Research for Evaluation of IASCC Susceptibility", *Corrosion Engineering*, 42, 3-12.

10. Majidi A.P. and Streicher, M.A. (1984), p584.

11. Japanese Industrial Standards, JIS G 0580 (1986).

12. Yoshimasa Iwabuchi, Takahiro Fujimoto, Yutaka Watanabe, and Tetsuo Shoji: Zairyo-to-Kankyo (in Japanese), vol.42 (1993) p.2.

13. Watanabe, Memo to IASCC Group at MIT.

14. Watanabe, Memo to IASCC Group at MIT.

15. Watanabe, Memo to IASCC Group at MIT.

16. Watanabe, Memo to IASCC Group at MIT.

Chapter 4

4. Discussion of Results

4.1. Introduction

The results of the analysis served to quantify the degree of segregation in the model alloys. It was believed that a pattern due to material composition and irradiation would be revealed through STEM analysis and corresposding EPR results, and that this pattern would shed light upon the mechanisms of RIS.

4.2. Discussion of STEM Results

4.2.1. RIS Literature Search

For a comparison with other data available, an extensive literature search for data pertaining to neutron-irradiated austenitic stainless steels was done. It was found that very little data existed for materials irradiated to the relatively low total fluence of 1 dpa or less. Figure 4.1 shows some results of this literature search. The data points shown in this figure represent the average compositional change seen at the grain boundaries analyzed.

The data from Kenik [1] was obtained from materials irradiated to 1.7 dpa at 288°C. These specimens were made of a high purity Type-304 SS (HP) and a commercial purity Type-304 SS (CP). [2] The compositional change plotted below in Figure 4.1 is the result of averaging the maximum compositional change seen at six grain boundaries measured on each material. The data from Asano, Nakata, Fukuya, and Kodoma [3], was obtained from materials irradiated over a range of 0.21dpa to 9.2dpa at a nominal temperature of 288°C. These specimens were made of Type-304 SS and Type-316 SS, and the compositional change plotted below is the result of averaging the change seen at two grain boundaries

per material, each grain boundary measurement being taken four times at close locations and averaged. The elemental compositions of both sets of materials are shown in Tables 4.1 and 4.2.

Table 4.1. Elemental composition of Asano *et. al.* materials (wt%).

Steel	C	Si	Mn	P	S	Ni	Cr	Mo	Fe
SUS304A	0.05	0.53	1.64	0.026	0.006	9.20	18.60	--	bal.
SUS304B	0.05	0.51	1.69	0.029	0.007	10.20	18.65	--	bal.
SUS316	0.05	0.58	1.73	0.021	0.006	13.10	16.55	2.25	bal.

Table 4.2. Elemental composition of Kenik's materials (wt%).

Heat	C	Si	Mn	P	S	Ni	Cr	N	Fe
CP	0.08[b]	1.00[b]	2.00[b]	0.05[b]	0.03[b]	9.25[a]	19.00[a]	--	70.68[a]
HP	0.02	0.02	1.22	0.002	0.003	9.44	18.58	0.04	70.68

[a]Average composition
[b]Maximum permitted

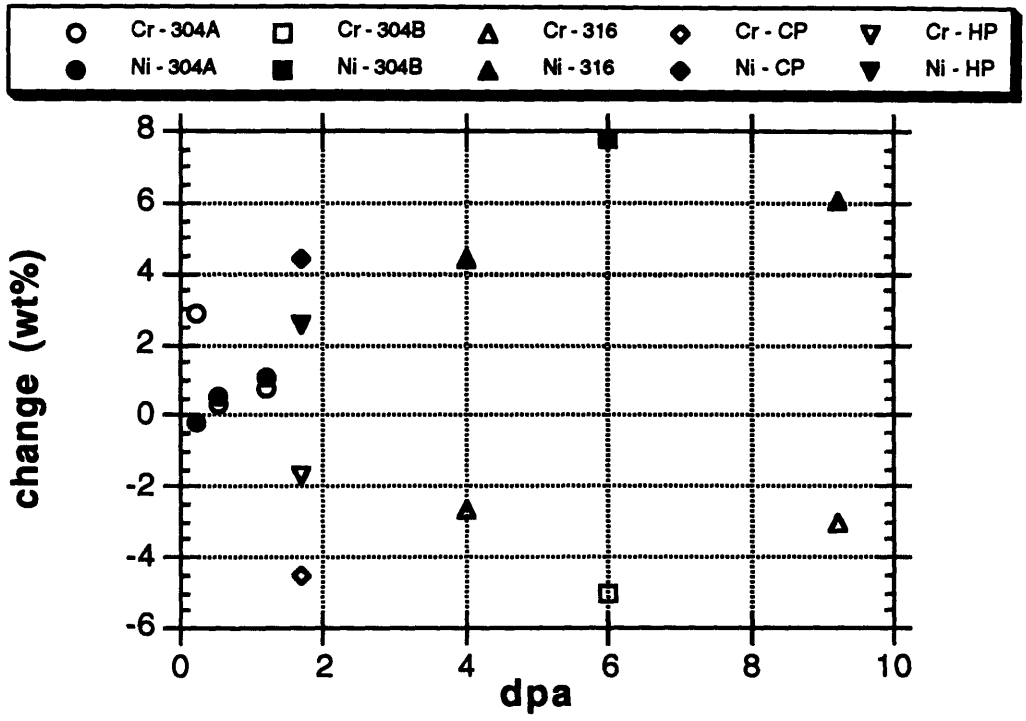

Figure 4.1. Compilation of literature search for Ni and Cr elemental composition changes at the grain boundary in relation to the bulk material. All data collected was for neutron-irradiated austenitic stainless steels.

In Figure 4.1., chromium enrichment at low dpa was noticed, but could not be verified since unirradiated blank material of the same heat was not obtained. Therefore, one can not know if this was due to irradiation effects or to thermal effects during manufacture. [4] It is seen, however that as the total fluence increases the chromium change approaches a more negative value, and the nickel change approaches a more positive value. It should also be noted that Kenik's data shows the high purity steel to be less affected by RIS.

4.2.2. Comparison with RIS Computer Simulation

Comparison of the STEM profiles with the RIS computer model results [5] are shown in Figures 4.2 through 4.6. RIS computer code input files were made

for each capsule according to the experimentally determined damage rate (dpa/s), nominal temperature (°K), and total fluence (dpa) (see Figure 2.4). The elemental composition input was that determined by Luvak, Inc. (see Table 2.1), and simulations were run for each of the experimentally acquired STEM profiles.

An important factor in the evaluation of RIS is the effect that grain boundary structure has upon the degree of segregation. Most current literature agrees with the statement that grain boundary orientation (which can be directly related to the grain boundary structure) or interfacial characteristics at the grain boundary affect the degree of sensitization [6] [7] [8] The RIS simulation code written by Boerigter makes use of a parameter designated as P_R (see Table 3.1), which is physically described as the percentage of grain boundary lattice points where recombination occurs. In simulating the theoretical RIS response of the analyzed TEM specimens, this parameter was varied so as to obtain a theoretical profile which matches the experimentally obtained one.

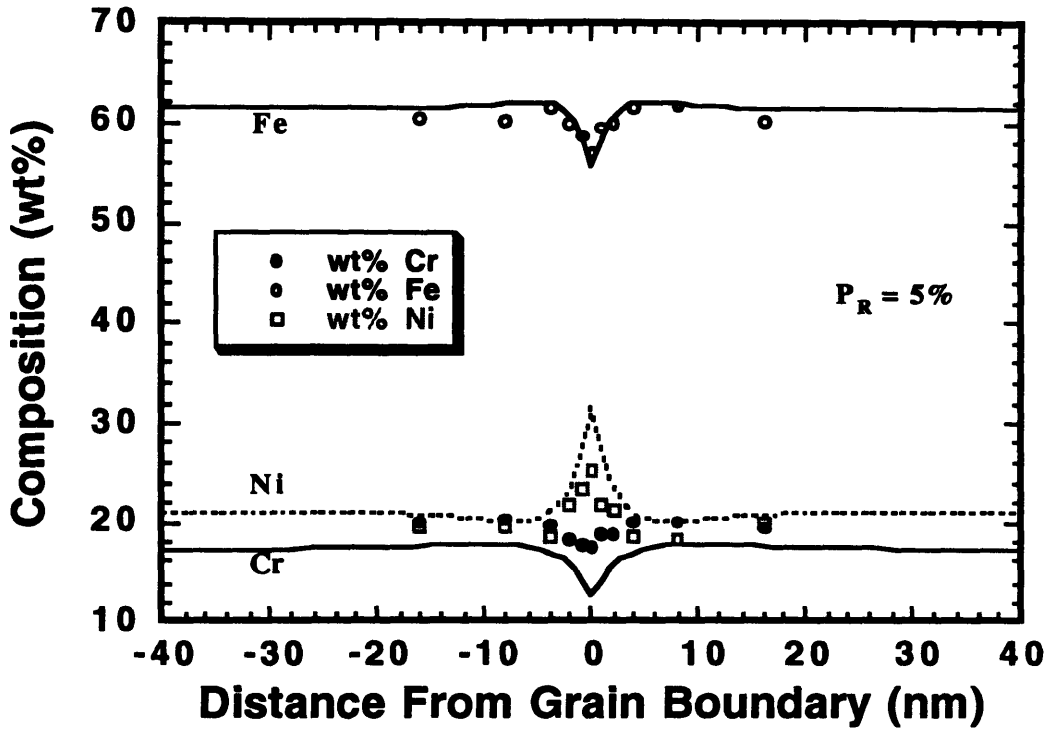

Fig. 4.2(a). STEM profile of a grain boundary in alloy N1 (from capsule #4, $0.8 \times 10^{21} n/cm^2$) and its corresponding RIS-code profile. STEM data corresponds with Figure 3.12(a).

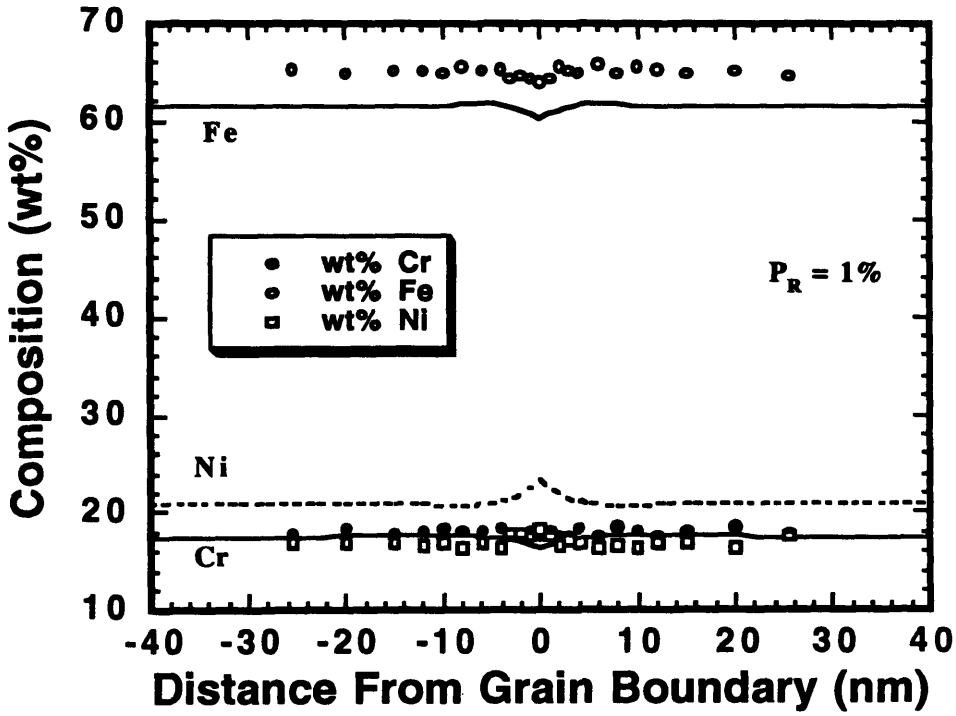

Fig. 4.2(b). STEM profile of a grain boundary in alloy N1 (from capsule #4, $0.8x10^{21}n/cm^2$) and its corresponding RIS-code profile. STEM data corresponds with Figure 3.12(b).

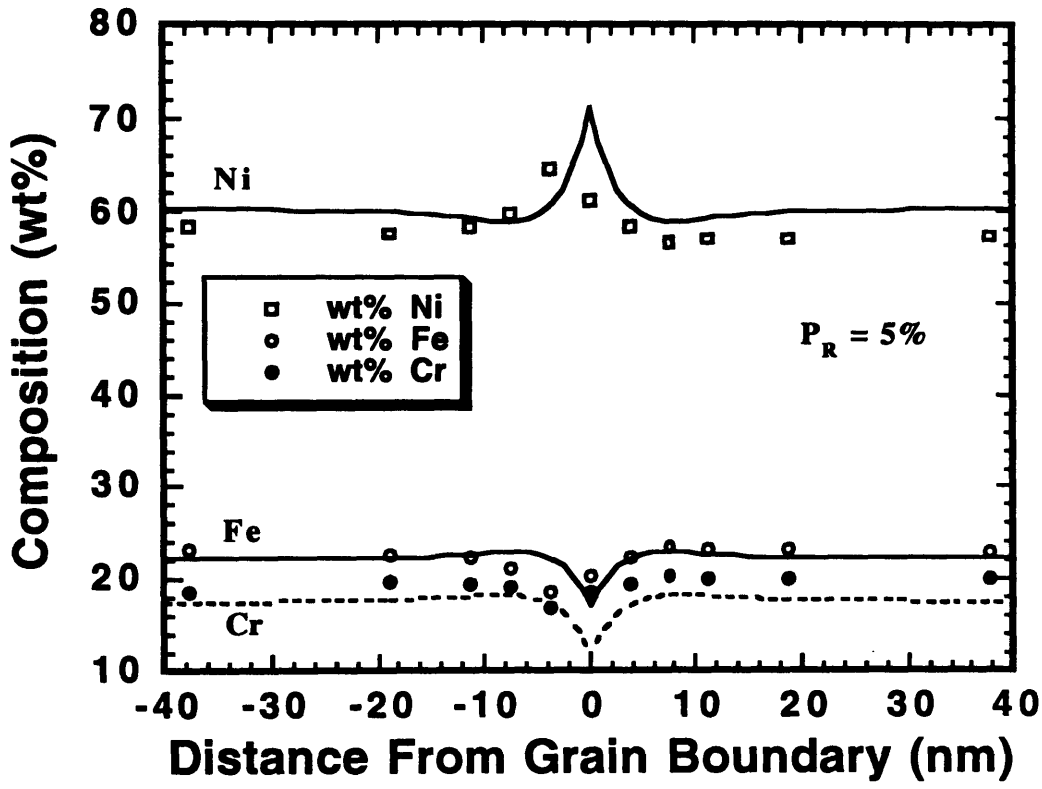

Fig. 4.3(a). STEM profile of a grain boundary in alloy N5 (from capsule #4, $0.8x10^{21}n/cm^2$) and its corresponding RIS-code profile. STEM data corresponds with Figure 3.13(a).

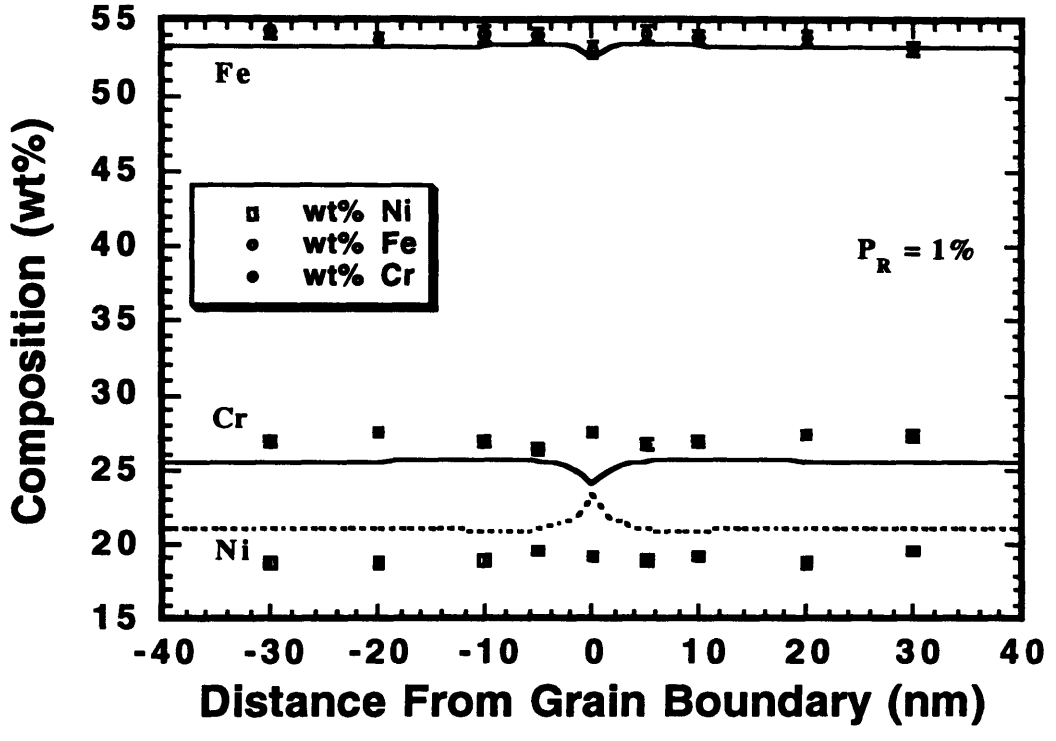

Fig. 4.4(a). STEM profile of a grain boundary in alloy N6 (from capsule #3. $0.74x10^{21}n/cm^2$) and its corresponding RIS-code profile. STEM data corresponds with Figure 3.14(a).

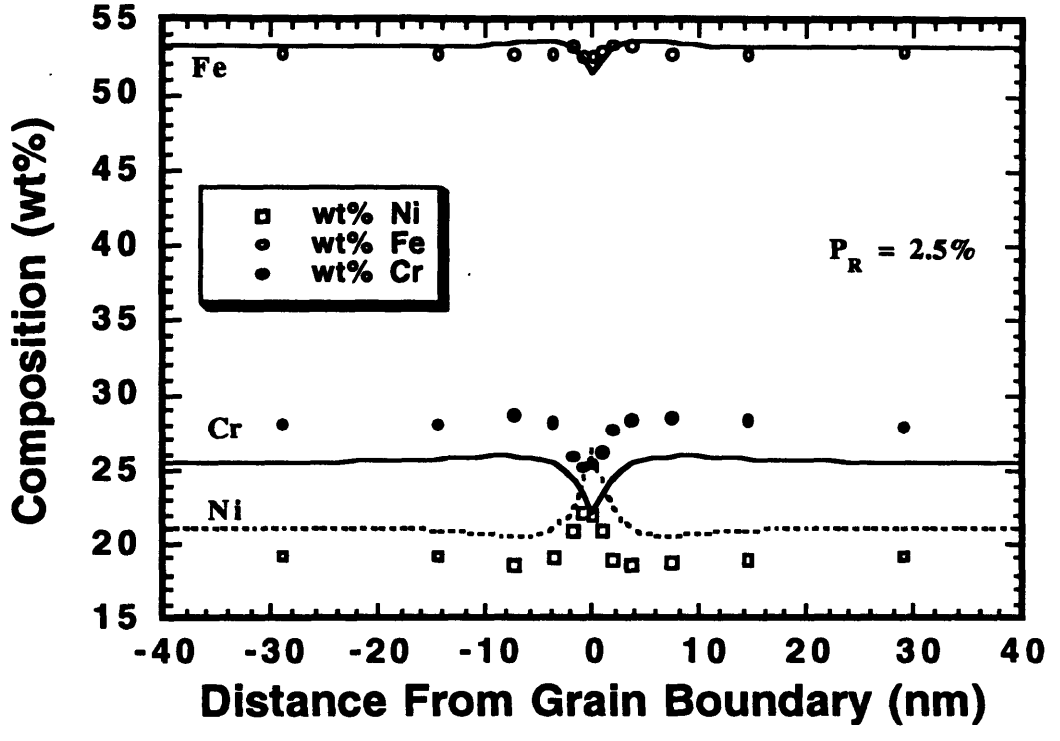

Fig. 4.4(b). STEM profile of a grain boundary in alloy N6 (from capsule #3, $0.74 \times 10^{21} n/cm^2$) and its corresponding RIS-code profile. STEM data corresponds with Figure 3.14(b).

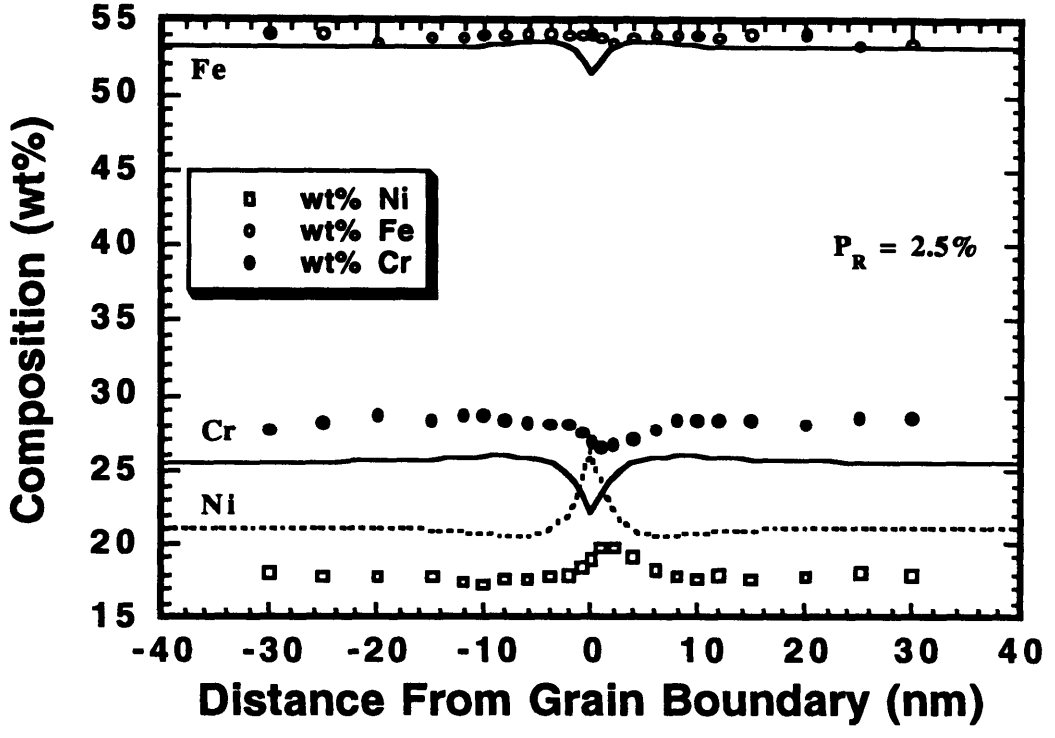

Fig. 4.4(c). STEM profile of a grain boundary in alloy N6 (from capsule #3, $0.74 \times 10^{21} n/cm^2$) and its corresponding RIS-code profile. STEM data corresponds with Figure 3.14(c).

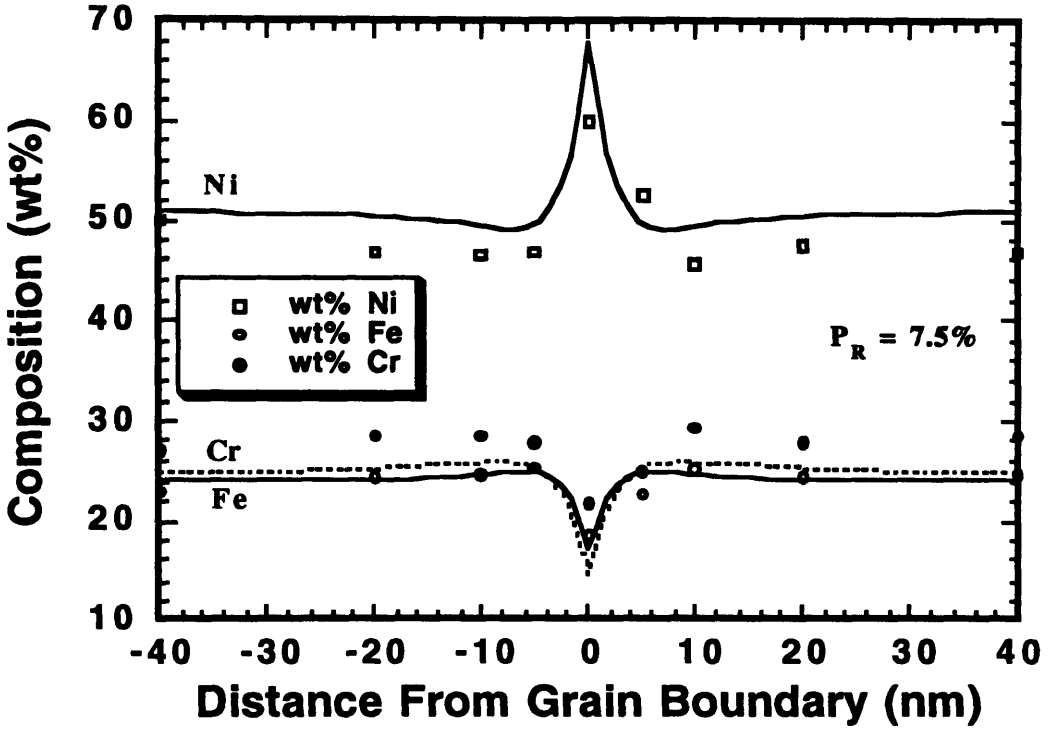

Fig. 4.5(a). STEM profile of a grain boundary in alloy N9 (from capsule #4, $0.8 \times 10^{21} n/cm^2$) and its corresponding RIS-code profile. STEM data corresponds with Figure 3.15(a).

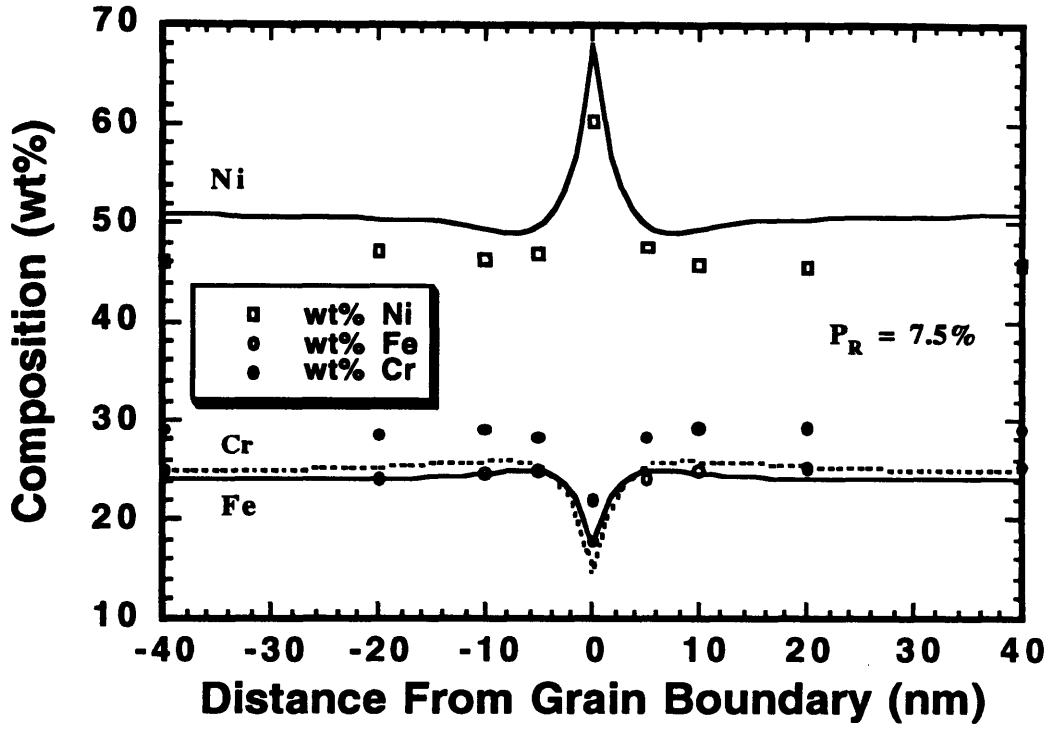

Fig. 4.5(b). STEM profile of a grain boundary in alloy N9 (from capsule #4, $0.8 \times 10^{21} n/cm^2$) and its corresponding RIS-code profile. STEM data corresponds with Figure 3.15(b).

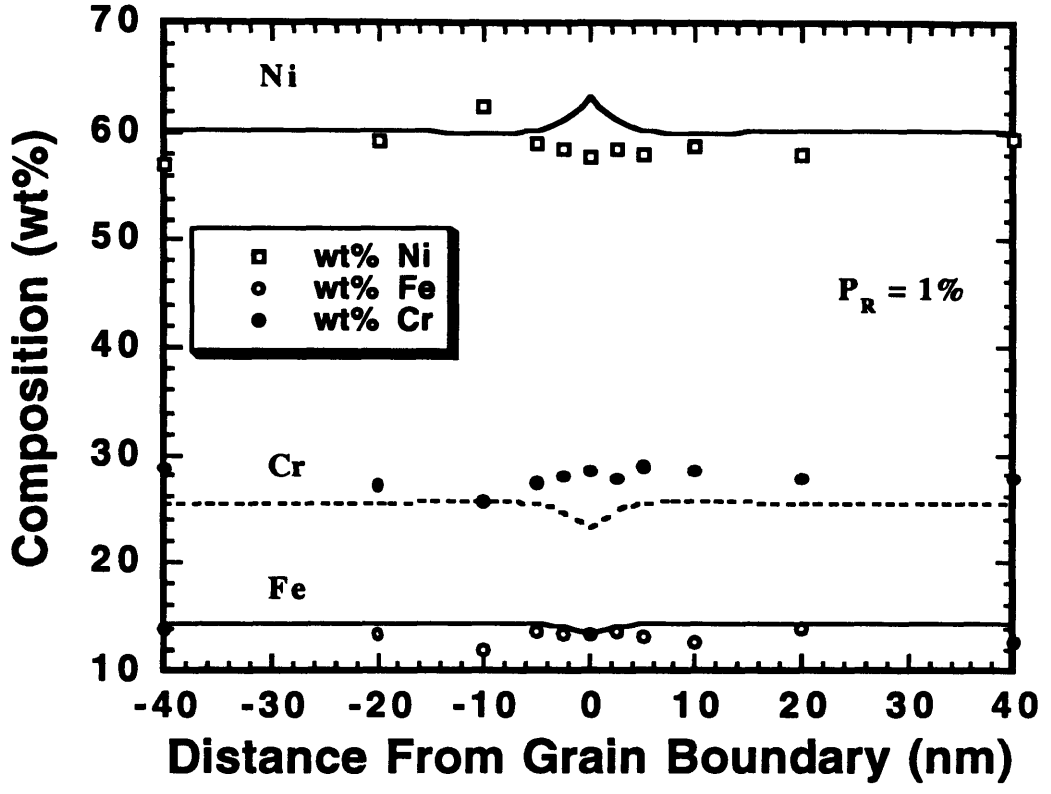

Fig. 4.6(a). STEM profile of a grain boundary in alloy N10 (from capsule #5, 0.86×10^{21} n/cm^2) and its corresponding RIS-code profile. STEM data corresponds with Figure 3.16(c).

The use of the STEM to measure a grain boundary profile was not an easy task. Due to diffraction characteristics at the grain boundary, and also due to tilting the specimen to achieve a very narrow view of the grain boundary, the visibility of the boundary was sometimes obscured. This made it difficult to decide upon the actual location of the boundary when taking profile measurements. For this reason, some of the experimental STEM profiles seem to be offset from the 'zero mark', the boundary position. This is clearly seen when the experimental profiles are compared to the theoretical profiles as evidenced in Figures 4.3(a), 4.4(a), and 4.6(a).

It should be noted that the RIS computer simulation generates compositional values for discrete nodal points at various distances from the grain boundary [9]. The experimental STEM profiles show compositional data which is obtained from an excited volume of the TEM foil being analyzed. This results in areas farther away from the grain boundary being analyzed, and due to the inherent narrowness of a RIS profile, causes the degree of chromium depletion seen at the grain boundary to be lower. This is only worsened by beam spreading and increasing thickness of TEM foils [10] [11]. For this reason, the simulated segregation at the grain boundary should be lower for chromium and iron and higher for nickel than is seen experimentally. The bulk concentrations in both the experimental and calculated data points should match, however. No attempt to account for the beam broadening effect is made here, but other research is being done to account for this, mostly through convolution techniques [12].

From the data presented in Figure 4.2 through 4.6, it is clear that in almost all of the comparisons made between the theoretical and the experimental data, there is a disparity between the bulk concentrations in the theoretical calculations and the bulk concentrations in the experimantal data. Consistently, the experimental chromium concentrations are higher and the experimental nickel concentrations are lower than the results of the wet chemistry analysis. Results by both Carter et. al. [13] and Kenik [14] show similar trends. Kenik attributes this to a surface film which forms during TEM jet polishing which is chromium rich. From the data presented above, this surface layer enhances the chromium enough to lower the iron and nickel concentrations. Relative changes in the alloying elements should still provide valuable data, however.

Figures 4.2 through 4.6 also shows the impact that grain boundary characteristics have on segregation at a grain boundary. In the case of alloys N1

and N6, different TEM specimens of the same alloy, exposed to the same conditions prior to STEM analysis, have varying degrees of segregation at different grain boundaries. All other conditions being kept constant, the grain boundary interfacial characteristics can account for the differences in the profiles analyzed, as evidenced by the calculated profiles. In calculating the segregation for these STEM profiles, P_R was varied in order to obtain matching theoretical profiles. This difference in P_R can be thought of as the factor which accounts for the different grain boundary orientations. Thus, different grain boundaries are either more or less favorable for the RIS phenomena depending upon their interfacial characteristics.

Due to the spatial resolution of the STEM in comparison to the RIS code, the degree of segregation at the grain boundary is difficult to compare. However, farther from the grain boundary, experimental and theoretical data support each other quite well. The RIS code predicts the formation of compositional "wells" on either side of the nickel enrichment peak. There are also compositional "hills" that form on either side of the chromium and iron depletion zones. Profiles seen in Figures 4.2(a), 4.2(b), 4.4(b), and 4.4(c) show a good correlation between the RIS code output and the experimental data at the "hill" and "well" regions.

Validation of the RIS code and the P_R variable is also evidenced at the "hill" and "well" regions. Profiles taken from the same materials exposed to the same conditions but having different degrees of segregation characteristics (e.g. their profiles are of markedly different shape) were matched by the RIS code by assigning a different value of P_R. These profiles show good correlation between theoretical and experimental data at the "hill" and "well" regions also.

An unexpected result in the STEM analysis, was the fluctuation seen in the profiles of the N10 alloys illistrated in Figure 4.7. Due to this fluctuation, the best

of the N10 STEM profiles was selected to compare the RIS simulation results with. A possible explanation for the compositional fluctuation is spinodal decomposition due to irradiation. Garner *et. al.* [15][16] have seen spinodal decomposition in irradiated Fe-35Ni and Fe-15Cr-35Ni alloys. In the latter alloy and in alloy N10 the Ni-Cr ratio is 43% and 42% respectively.

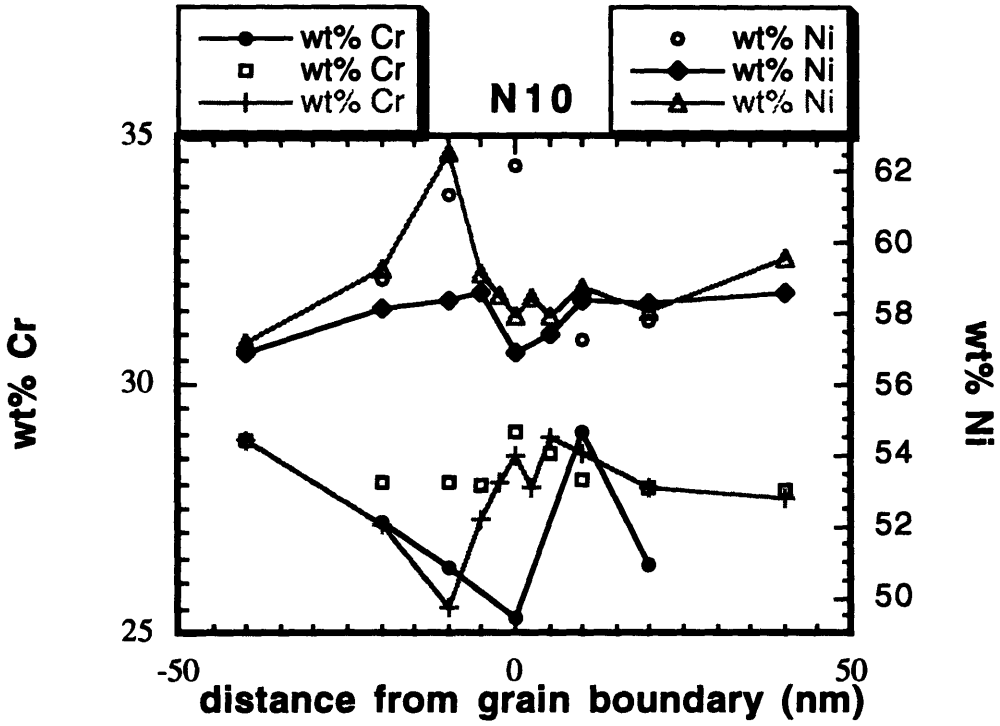

Figure 4.7. N10 STEM profiles for Ni and Cr.

To compare the unirradiated material with the irradiated material, the STEM was used to analyze several points both on and off the grain boundary in an unirradiated N10 TEM specimen. The results are summarized in Figure 4.8 and show that the compositional fluctuations seen in irradiated N10 alloys can be attributed to the irradiation.

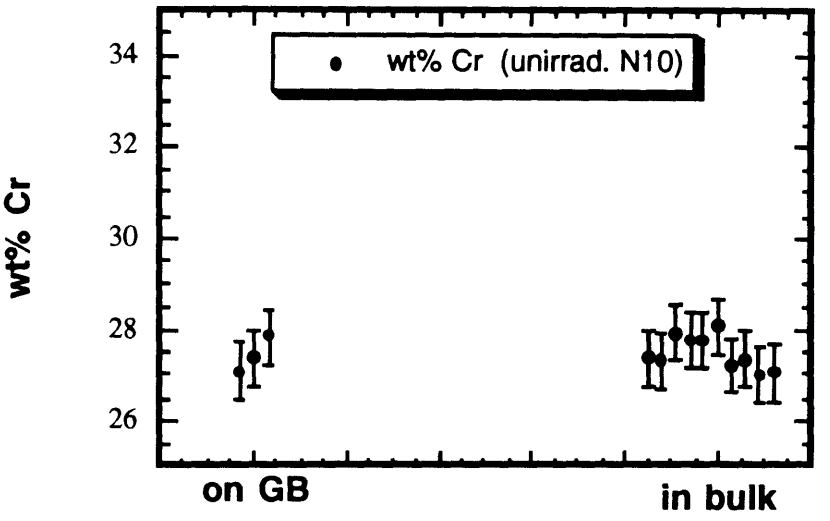

(a)

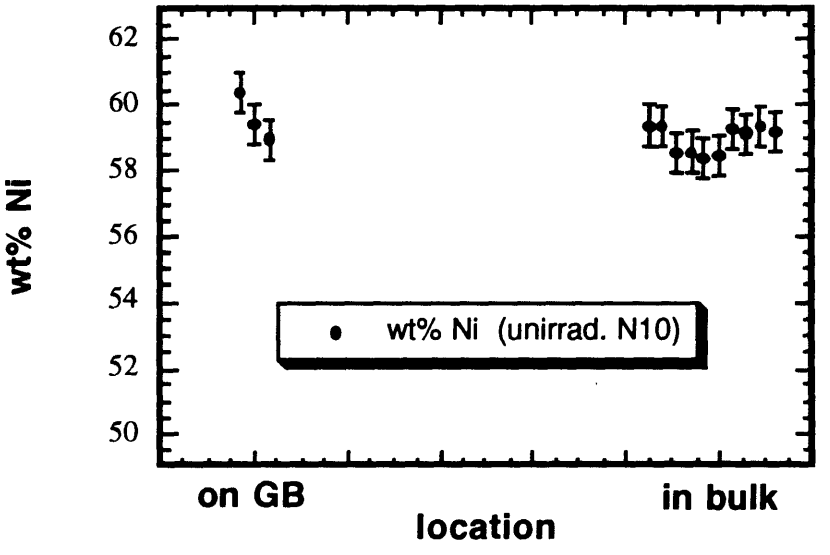

(b)

Figure 4.8. Unirradiated N10 STEM analysis. Data was taken at various points in the grain at least 100nm away from any grain boundary and on various adjacent locations on the same grain boundary.

4.2.3. Relationship of Major Alloying Elements to RIS

Due to the special selection of compositions of the model alloys, direct comparisons can be made between STEM profiles of different materials. As long as all else is held constant, except for a change in one elemental composition, these direct comparisons can lead to insight into the role that the major alloying elements play in the phenpmena of RIS.

With respect to the process of elemental diffusion, Boerigter's code accounts for differences in diffusion rates by careful selection of the migrational enthalpies of the major elements. The inherent difference between grain boundary profiles of the same material and of similar irradiation (all of the materials analyzed in this research are "high-dose" specimens with respect to irradiation) and thermal history but marked difference in the degree of segregation is due to the factor which is accounted for in the code by the P_R variable. In a physical sense, this computer code parameter accounts for the grain boundary orientation. Therefore, in comparisons of STEM profiles of different materials which were "matched" by computer simulations that used the same value of P_R, one can infer a similar grain boundary orientation also.

Figures 4.9 shows plots of the STEM profiles so as to allow direct comparison.

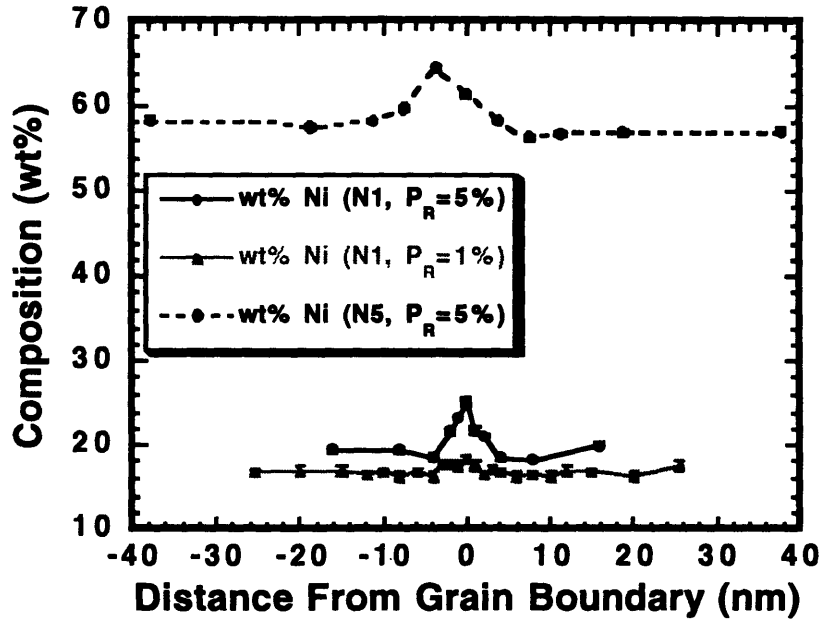

(a) Comparison of wt% nickel enrichment at grain boundaries in N1 and N5.

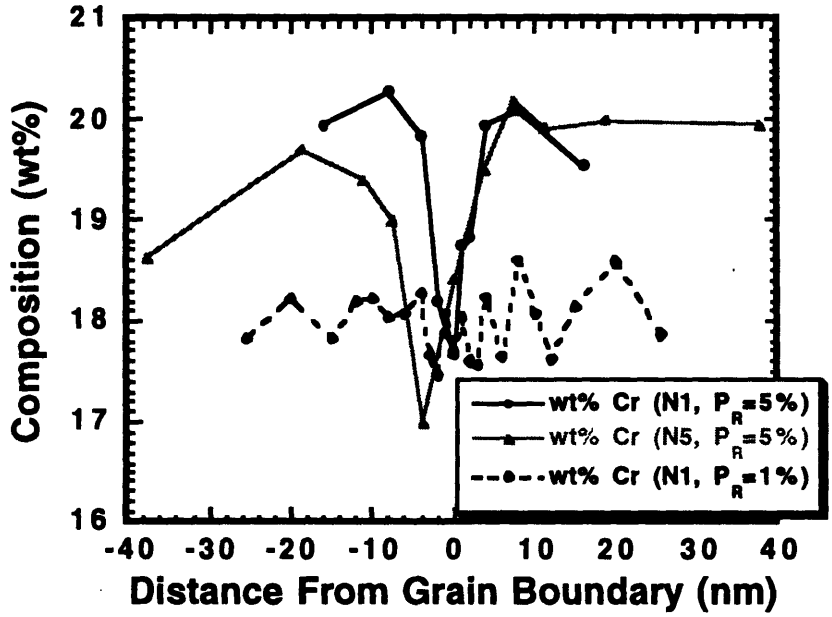

(b) Comparison of wt% chromium depletion at grain boundaries in N1 and N5.

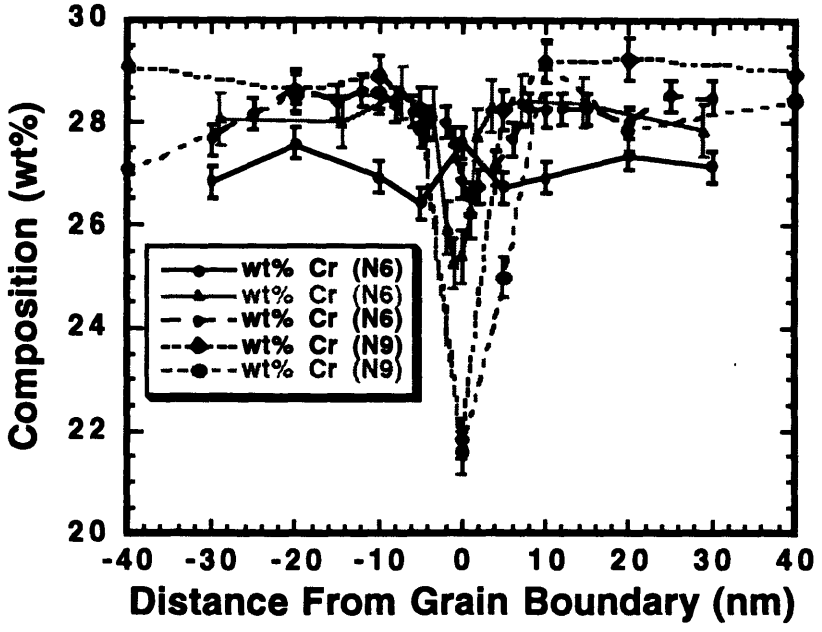

(c) Comparison of wt% chromium depletion at grain boundaries in N6 and N9.

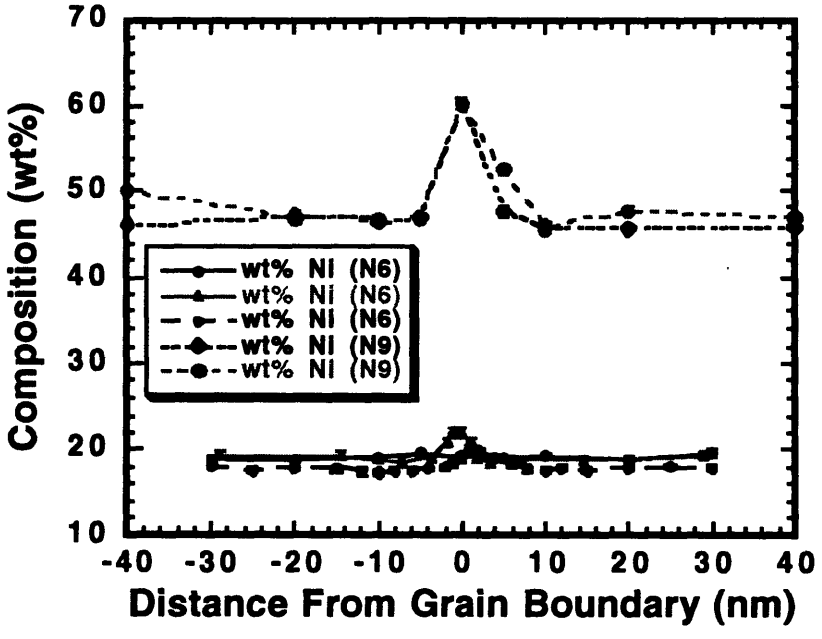

(d) Comparison of wt% nickel enrichment at grain boundaries in N6 and N9.

Figure 4.9. Comparisons of chromium depleted and nickel enriched grain boundaries via STEM-EDX analysis.

In comparing the STEM profiles, the difference between the average bulk composition and the highest enriched data point or lowest depleted data point was calculated. Due to the statistical methods used in EDX analysis, this calculation will carry with it an error of approximately $\pm$ 0.8wt%.

In comparing the change in wt% of nickel between alloy N1 and alloy N5, it is found that the two STEM profiles that were matched by the RIS computer code with a P_R of 5% have an enrichment of 6wt% and 6.5wt% respectively. This is not a statistically significant difference with respect to EDX STEM analysis.

In comparing the change in wt% of chromium between alloy N1 and alloy N5, it is found that the two STEM profiles that were matched by the RIS computer code with a P_R of 5% have a depletion of 2.2wt% and 2.9wt% respectively. Again, this is not statistically significant.

Comparison of the remaining profiles was performed by averaging the depletion or enrichment found at individual grain boundaries of the same material, and comparing between the different materials. This was done because there were no other profiles that had the same P_R for the simulation profile.

In comparing the differences between chromium enrichment and nickel depletion between alloys N6 and N9, the average chromium depletion seen in alloy N6 was approximately 1.7wt% whereas the average chromium depletion seen in alloy N9 was approximately 7wt%. The nickel enrichment was most pronounced in the N9 alloy, with the average enrichment being 13wt%. For N6 the average nickel enrichment was 2wt%. Due to the poor profiles obtained for alloy N10 no comparisons were done.

Comparing the average chromium depletions between N1 and N6, the results are a 1.2wt% and 1.7wt% depletion respectively. This difference is not statistically significant. Comparing the average nickel enrichments between N1

and N6, the results are a 4wt% and a 2wt% enrichment respectively. This lies on the edge of statistical significance.

4.3. Discussion of EPR Results

The results of the double-loop modified EPR testing with pre-conditioning were intended to provide an objective account of the degree of sensitization in a material. With this data, comparison between different materials and materials of the same composition but different irradiation histories could easily take place. This objective sense of comparison was not available, however, due to some unexpected results seen for alloys N9 and N10.

4.3.1. EPR Analysis of Alloys N9 and N10

The Mod-EPR results of alloys N9 and N10 are marked by the presence of secondary activation and reactivation peaks in both the irradiated and unirradiated specimens. These peaks occurred at a lower absolute value of potential and also had a lower associated current density. They are shown in Figure 3.21, and their presence is made known in the calculated EPR ratios seen in Table 3.4. Figure 4.10 shows an expanded view of the secondary activation peaks and reactivation peaks seen in the EPR data of these alloys.

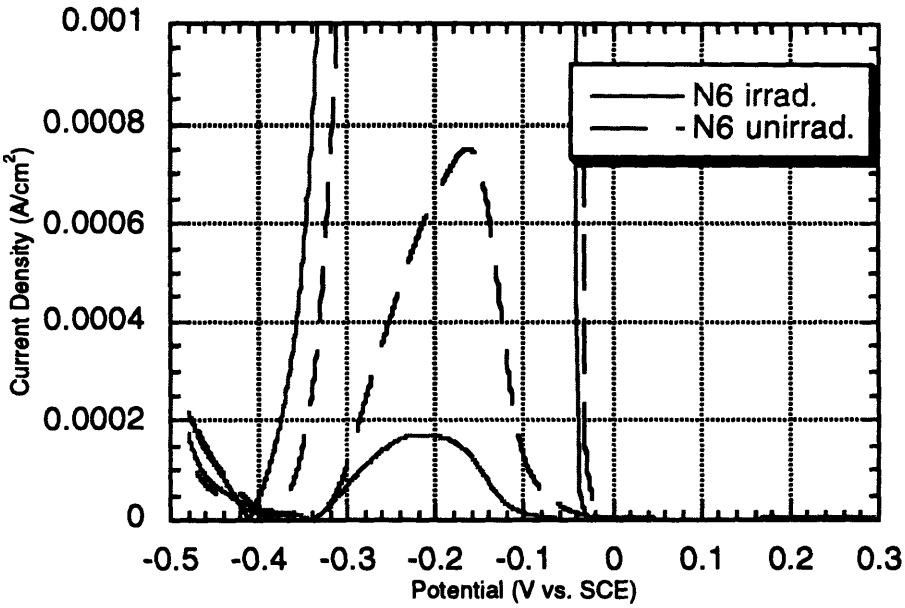

(a) N6 EPR Data. No Secondary activation peaks seen.

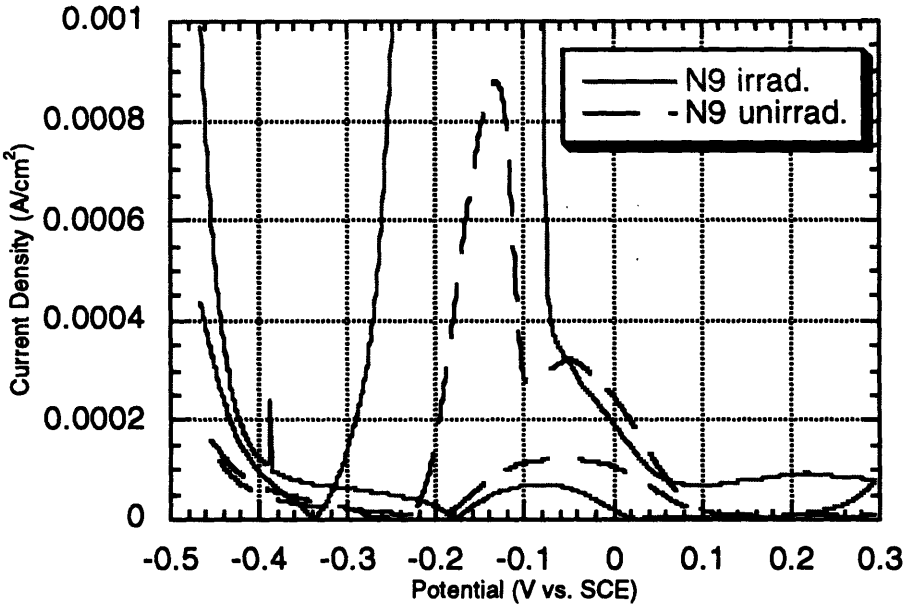

(b) N9 EPR Data.

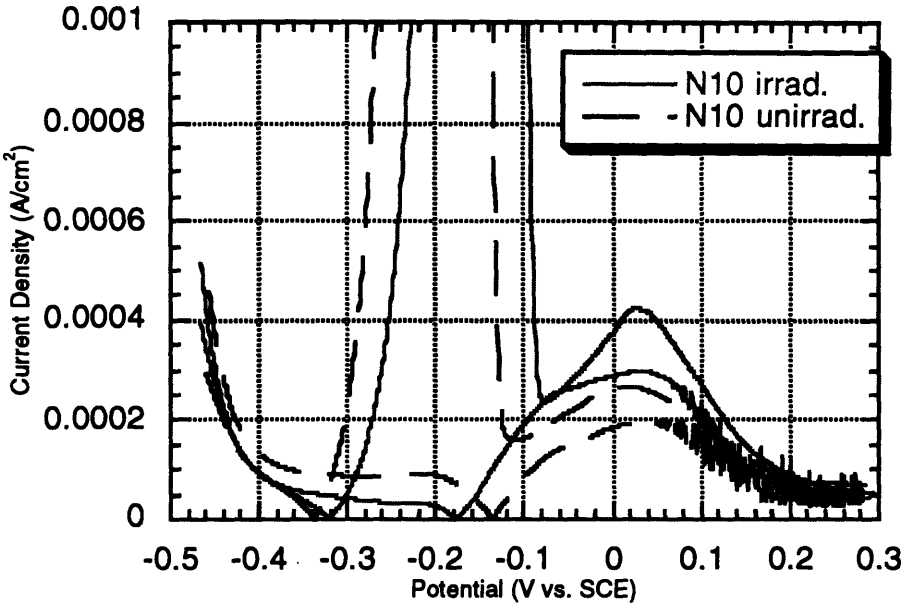

(c) N10 EPR Data.

Figure 4.10. Expanded view of EPR data. Note the secondary activation peaks.

Although the secondary peaks make comparison difficult when trying to determine how the degree of sensitization is affected by the presence of nickel, it does provide insight into the microchemistry and microstructure of the materials.

For alloy N9, only one EPR ratio was listed for the irradiated specimen. This was done due to the lack of a secondary activation peak, but in Figure 4.10 this can be attributed to the width of the primary activation peak. The expected secondary activation peak would be present at the same potential of the secondaty activation peak of the unirradiated specimen, however, in the above figure, this peak appears to be hidden, by the primary peak. The EPR trace does change its slope at this expected point to more closely match the trace of the unirradiated sample.

Figure 4.10 also shows that the reactivation peaks for alloy N10 occur at the same potential as the secondary activation peaks. In Table 3.4, the calculated EPR ratio for the first activation peak of the unirradiated N9 alloy was derived using the single reactivation peak seen. This reactivation peak may correspond to either the primary or secondary activation peak, but the potential that its peak is located at is between the peak potentials of the primary and secondary activation peak. Alloy N10, however, was seen to have no reactivation peaks corresponding to the primary activation peaks.

The potential separation between the primary and secondary activation peaks for alloy N10 is approximately 0.2V. For alloy N9 this separation is diminished, and from the EPR trace obtained by Watanabe for alloy N8, the presence of any secondary peaks can not be seen. It should be noted that the secondary peaks occur in both the irradiated and unirradiated materials, leaving one to suspect that irradiation was not the causal factor.

The surface morphology of the post-EPR N9 and N10 alloys corresponds well with the presence of the twin-peak EPR results. On all of the N9 and N10 post-EPR surfaces there appear two distinct areas of corrosion. The SEM micrographs in Figures 3.24 and 3.25 show these areas as lighter tone and a darker tone regions. To the unaided human eye, the actual appearance is that of an area which has a dark blue film (lighter tone area in the SEM) and a silver, polished surface that appears not to be affected by the EPR test (darker tone area in the SEM). In all micrographs taken, the darker tone region showed no sign of grain boundary attack and appeared relatively unharmed by the corrosive environment of the test. These regions are expected to correspond to the primary activation peak in the EPR traces of alloys N9 and N10, and this is supported by no reactivation peak being seen at the corresponding potential. There is a slight difference seen in the micrographs taken at a magnification of 2000X between the

dark tone regions of irradiated and unirradiated N10 and N9. Both the N9 and N10 irradiated dark-tone regions have small crack-like pits, whereas, their unirradiated counterparts do not.

All instances of grain boundary etching occur in the light-tone regions. For alloy N9 grain boundary etching is present in the irradiated as well as the unirradiated specimens. For alloy N10, grain boundary etching is present only in the irradiated specimens.

4.3.2. EPR for Alloy N6

The EPR analysis of alloy N6 provided results that behaved in a similar manner to what was expected.

Although the results obtained by Watanabe use the Mod-EPR technique, this method should not provide results which are incomparable. This was evidenced in practice tests done on the N6 material which show good repeatability between the Moc-EPR and Mod-EPR tests done on unirradiated specimens. Watanabe's N8 EPR data is also similar in appearance to the N6 data shown in the above figures in that there is only one activation and reactivation peak, and the current drops off quite suddenly after it reaches its activation peak.

Comparison of alloys N6 and N8 can be done through the EPR ratios obtained on these materials and seen in Table 3.4. The EPR ratios of the irradiated specimens show an increase in the degree of sensitization as nickel increases. Inconsistency in the expected degree of sensitization is seen, however, in the EPR ratio of the unirradiated N6 alloy. One would expect the degree of sensitization in this specimen to be less.

The post-EPR surface morphology for alloy N6 is seen in Figure 3.23. A higher degree of grain boundary attack and general surface corrosion is seen in the unirradiated specimen which corresponds well with its higher EPR ratio.

Figure 3.23(d) also shows a characteristic of surface morphology only seen in irradiated specimens. The etched pit seen in this figure is similar to results reported by Watanabe [17].

4.4. References:

1. Kenik E.A., (1992) "Radiation-induced segregation in irradiated Type 304 stainless steels", *J. Nucl. Mater.* 187, **239-246.**

2. Kenik, p.239.

3. Asano, Fukuya, Nakata, and Kodoma, "Changes in grain boundary composition induced by neutron irradiation", Proc. of 5th int. symp. on env. deg. of mat. in nuclear power systems-water, p.839.

4. Asano *et. al.*, p. 842.

5. Stephen T. Boerigter, "An Investigation of Neutron-Induced Segregation in Austenitic Stainless Steels", PhD Thesis, Dept. of Nucl Eng., M.I.T., (December 1992).

6. Boerigter, PhD Thesis, (December 1992).

7. Bruemmer S.M., Merz M.D., and Charlot L.A., (1991) "A method for evaluating radiation-induced grain boundary segregation using ion-irradiated microcrystalline stainless alloys", *J. Nucl. Mater.* 186, **13-19.**

8. Carter, Damcott, Atzmon, Was, and Kenik, (1993) "Effects of proton irradiation on the microstructure and microchemistry of type 304L stainless steel", *J. Nucl. Mater.* 205, **361-373,** p.363.

9. Boerigter, PhD Thesis, (December 1992).

10. Kenik, p.241.

11. Carter *et. al.*, p.363.

12. Carter *et. al.*, p.363.

13. Carter *et. al.*.

14. Kenik.

15. Garner, Brager, and McCarthy, (1987) "Neutron-Induced Spinodal-Like Decomposition of Fe-Ni and Fe-Ni-Cr Alloys", *Radiation Induced Changes in Micro-structure: 13th International Symposium (Part I)*, ASTM STP 955, **775-787**

16. Garner, McCarthy, Russell, and Hoyt, (1993) "Spinodal-like decomposition of Fe-35Ni and Fe-Cr-35Ni alloys during irradiation or thermal aging",. *Nucl. Mater.* 205, **411-425**.

17. Watanabe, Y.W., "Application of Electrochemical Methods for Characterization of Grain Boundary Microchemistry in Irradiated Austenitic Stainless Steels", Memo to IASCC Project Research Group, MIT, July, 1993.

Chapter 5

5. Conclusions

5.1. Introduction

Through the use of scanning transmission electron microscopy (STEM) and double-loop electrochemical potentiokinetic reactivation (DL-EPR) testing, several of the model alloys were analyzed. Priority was given to those alloys with the most extreme compositional differences expecting comparison of results to be easier due to more distinct differences. The systematic variation of the alloys' compositions could then be attributed to the differences seen. Analysis of results also contributed to conclusions about better methods which should be used to continue this research.

5.2. Summary and Conclusions of Experimental Work

5.2.1. Conclusions of STEM Analysis

In comparing only the average compositional changes at the grain boundaries, direct comparisons between alloys N1 and N5 show that increased concentrations of nickel slightly increase the nickel enrichment and the chromium depletion For comparison of alloys N6 and N9, increases in the nickel concentration result in a more enhanced nickel enrichment and chromium depletion. It is apparent that the decrease in bulk iron concentration and corresponding increase in bulk chromium concentration enhances the segregation seen at the grain boundary. This can be attributed to the faster diffusion rate of chromium.

In comparing Alloy N1 to alloy N6, one can conclude that increased chromium would inhibit nickel enrichment but enhance chromium depletion.

Verification of this would not seem to be true by comparing alloy N5 to alloy N9, however. Comparison of alloys N5 and N10 would be preferential, but the lack of good compositional profiles prohibits this.

It is apparent, however, that an alloy high in both nickel and chromium concentrations has large enrichments in nickel and large depletions in chromium at the grain boundary. Results also support the use of the chosen migrational enthalpies used in the RIS simulations.

The STEM analysis of the model alloys can not, at the present time, lead to any concrete conclusions about the effect that the major alloying elements have on RIS. The results of averaging the segregation effects at the grain boundaries require that many more boundaries be analyzed before any general conclusions can be drawn. This is evidenced by comparing only those grain boundaries in alloys N1 and N5 which were matched by the computer code using the same value for the probability of recombination. These results show only slight differences between these boundaries with respect to chromium depletion or nickel enhancement. If this is the case, and if the P_R factor accounts for the grain boundary orientation, this would lead one to conclude that the dominant factor affecting RIS is the orientation of the adjoining grains with respect to each other.

Comparison of the STEM profiles with the computer code output shows good correspondence between the two. This is especially seen at the "hill and well" regions of the profiles which are not only predicted but noticed as well by STEM analysis. This correspondence between experimental and theoretical, even in profiles of the same material but different degrees of segregation and different probabilities of recombination, also adds support to the factor which accounts for the different grain boundary orientations. Comparison also reveals the need for techniques to be developed which will diminish the disparity due to spatial resolution of STEM analysis at the grain boundary.

5.2.2. Conclusions of EPR Analysis

Comparison of EPR analysis between alloys N6 and N8 show an increased general degree of sensitization which can be attributed to the increased nickel concentration. Comparison with the irradiated N9 TEM specimen supports this statement as well. However, the reliability of the N9 data as well as the N10 data with respect to comparing the degree of sensitization is questionable, due to the presence of secondary activation and reactivation peaks.

The secondary activation and reactivation peaks seen in the EPR data of alloys N9 and N10 was thought to be accounted for by the presence of two regions in these materials with varying compositions of nickel and chromium. The region which corresponds to the primary peaks is also seen in the SEM micrographs as the darker tone region. No corrosion or grain boundary attack is seen in this region, and no primary reactivation peak is seen for the N9 or N10 samples. This would also suggest the presence of a higher chromium content. The region which corresponds with the secondary activation peaks is seen as the lighter tone regions in the SEM micrographs. These regions show a high degree of corrosion as well as grain boundary attack which corresponds well with the reactivation peaks seen in the EPR traces. This also suggests a lower chromium content and possibly enhanced chromium depletion at the grain boundaries in these regions. SEM mapping of the surface of the unirradiated N10 alloy was performed, but no compositional differences between the two regions were noted.

5.3. Recommendations for Future Work

Any future STEM analysis would have to include two major improvements. The first of these is simply to increase the number of grain boundaries in each material analyzed. This would greatly enhance any statistical analysis and allow for more concrete conclusions to be inferred. The second is much more difficult, but much more important from the standpoint of validating the RIS computer code. This second improvement is to determine the grain boundary orientation. This could possibly be done by diffraction techniques used in the STEM to determine the grain orientations on either side of the grain boundary, or more likely, to "mark" the grain boundary being analyzed in the STEM via contamination and then place the sample in a transmission electron microscope (TEM) to determine the orientation of the grains on either side of the boundary. In this fashion, the grain boundary orientation could be determined and assigned a qualitative value. This would allow for comparison between grain boundaries of similar orientation and also would allow for better determination of the validity of the P_R variable.

For comparative purposes, two other techniques should also be adopted for future research. Ion-milling should occur after jet-thinning of the TEM specimens to clean them of any chromium-rich surface film that may have formed during the thinning process, and convolution techniques should be used to improve comparison between the experimental and theoretical data at the grain boundary.

Appendix A

A. Elemental composition of materials in dry irradiation. [*1]

TYPE	HEAT	TEM Alloy #	SSRT	Auger	Mn	Ni	Cr	Mo	Nb	T	Co
304L	AJ9139	1	√	√	0.93	8.13	18.37	0.25			0.154
304L	V945	2	√	√	1.11	9.03	19.21	0.005			
316L	K5	3	√	√	0.83	12.15	16.70	2.15			0.004
347L	K12	4	√	√	0.84	9.38	17.55	0.16	0.3		0
304-Mod	BPV827	5	√	√	1.19	29.83	30.34	0.02			
304L	GAB1928	6		√		9.50	18.50				
Not Used		7									
304L	BPV603	8		√	1.15	9.02	19.06	0.005			
304L	BPV604	9		√	1.16	9.02	19.14	0.005			
304L	BPV605	10		√	1.15	9.00	19.03	0.005	0.47		
Special	1N	11			1.2	20.00	18.00				
Special	2N	12			1.2	30.00	18.00				
Special	3N	13			1.2	40.00	18.00				
Special	4N	14			1.2	50.00	18.00				
Special	5N	15			1.2	60.00	18.00				
Special	6N	16			1.2	20.00	26.00				
Special	7N	17			1.2	30.00	26.00				
Special	8N	18			1.2	40.00	26.00				
Special	9N	19			1.2	50.00	26.00				
Special	10N	20			1.2	60.00	26.00				
	NX10C1H	21									
	7	22									
	15	23									
	19	24									
	12	25									
	18	26									
	20	27									
IN-625		28			0.25	61.00	21.50	9	3.65	0.2	
IN-825		29			0.5	42.00	21.50	3		0.9	
304L	GAB1929	30			1.2	9.50	18.50				
316NG	D441103	31			1.74	12.90	17.15	2.48			
304L	V946	32			1.06	8.90	18.68	0.005			
304-Mod	BPV828	33			1.18	23.86	24.47	0.02			
	K5-10	34									
316L-Ti	S4	35			0.92	12.35	17.36	2.11	0.002	0.21	0.004
	K12-8	36									
347LPN	L3	37			0.93	9.51	17.61	0.35	0.3		0.01
316L-Nb	S3	38			0.93	12.34	17.38	2.13	0.3	0.006	0.004
321L	K15	39			0.87	9.36	17.54	0.16		0.23	
304L	K2	40			0.87	9.96	18.54	0.16			
347	C8	41			1.41	9.80	17.58		0.55		0.23
	R523										
316	C5	43			1.23	12.70	17.38	2.13			0.25

A. (continued) Elemental composition of materials in dry irradiation.

TYPE	HEAT	TEM Alloy #	SSRT	Auger	C	Si	P	S	N	Notes
304L	AJ9139	1	√	√	0.066	0.47	0.026	0.028	0.048	0.29 Cu
304L	V945	2	√	√	0.005	0.03	0.005	0.005	0.003	UHP
316L	K5	3	√	√	0.01	0.5	0.1	0.001	0.033	
347L	K12	4	√	√	0.011	0.12	0.012	0.001	0.036	
304-Mod	BPV827	5	√	√	0.019	0.02		0.004	0.005	
304L	GAB1928	6		√	0.003			0.136	0.002	UHP ++ S
Not Used		7								
304L	BPV603	8		√	0.002	0.02	0.05	0.006	0.002	UHP + P
304L	BPV604	9		√	0.001	0.46	0.005	0.004	0.002	UHP + Si
304L	BPV605	10		√	0.001	0.01	0.005	0.006	0.002	UHP + Nb
Special	1N	11								Bal Fe
Special	2N	12								Bal Fe
Special	3N	13								Bal Fe
Special	4N	14								Bal Fe
Special	5N	15								Bal Fe
Special	6N	16								Bal Fe
Special	7N	17								Bal Fe
Special	8N	18								Bal Fe
Special	9N	19								Bal Fe
Special	10N	20								Bal Fe
	NX10C1H	21								
	7	22								
	15	23								
	19	24								
	12	25								
	18	26								
	20	27								
IN-625		28			0.05	0.25		0.008		2.5 Fe
IN-825		29			0.03	0.25		0.015		2.25 Cu, 30 Fe
304L	GAB1929	30			0.003			0.211	0.003	UHP ++ S
316NG	D441103	31			0.018	0.5	0.02	0.001	0.083	Com LS
304L	V946	32			0.002	0.01	0.005	0.019	0.003	UHP + S
304-Mod	BPV828	33			0.011	0.02		0.004	0.004	
	K5-10	34								
316L-Ti	S4	35			0.017	0.51	0.026	0.001	0.009	
	K12-8	36								
347LPN	L3	37			0.017	0.47	0.012	0.002	0.076	
316L-Nb	S3	38			0.017	0.5	0.027	0.002	0.038	
321L	K15	39			0.014	0.48	0.012	0.001	0.037	
304L	K2	40			0.015	0.11	0.01	0.001	0.035	
347	C8	41			0.04	0.74	0.032	0.01		
	R523									
316	C5	43			0.019	0.061	0.034	0.002		

*1. Boerigter, PhD Thesis, (December 1992), pp. 90-91.

Appendix B

B. TEM Specimen Testing and Storage Summary

[Red Brick]

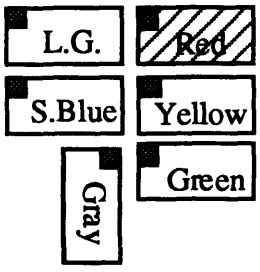

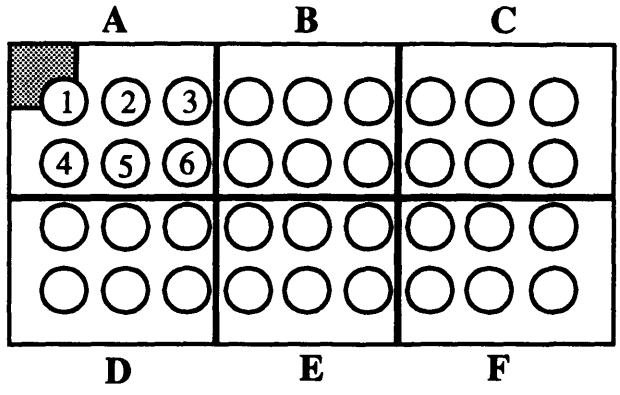

LEGEND

F-6 #10 (BPV605) / T-x-y
Location of storage hole *Material ID#* *Name of material* *# of TEM disks*

Capsule #7

A-1
#9(BPV604) / 3
#10(BPV605) / 1
#11(1N) / 2
#12(2N) / 5

Capsule #7

B-1
#34(K5-10) / 3
#35(S4) / 1
#38(S3) / 1
#39(K15) / 1

Capsule #4

C-1
#5(BPV827) / 8
#6(GAB1928) / 1
#9(BPV604) / 2
#10(BPV605) / 2

Capsule #7

A-2
#13(3N) / 1
#14(4N) / 1
#15(5N) / 1
#16(N9) / 1

Capsule #7

B-2
#40(K2-2) / 2
#41(C-8) / 3
#42(R583) / 2
#43(C5) / 2

Capsule #4

C-2
#11(1N) / 2-1-1
#12(2N) / 3
#13(3N) / 1
#14(4N) / 2

Capsule #7

A-3
#17(7N) / 2
#18(8N) / 2
#19(N6) / 2
#20(10N) / 3

Capsule #7

B-3
#5(BPV827/ 4-1

Capsule #4

C-3
#15(5N) / 3-1-1
#16(N9) / 3-1-1-1
#17(7N) / 2
#18(8N) / 2

Capsule #7

A-4
#21(NX10C1H) / 2
#22(7) / 1
#23(15) / 2
#24(19) / 1

B-4 —

Capsule #4

C-4
#19(N6) / 0
#20(10N) / 2-1
#21(NX10C1H) / 3
#22(7) / 0

Capsule #7

A-5 #25(12) / 1
#26(18) / 3
#28(IN-625) / 1
#29(IN-825) / 1

B-5 —

Capsule #4

C-5 #23(15) / 0
#24(19) / 2
#25(12) / 1
#26(18) / 1

Capsule #7

A-6 #30(GAB1929) / 1
#31(D441103) / 1
#32(V946) / 2
#33(BPV828) / 3

B-6 —

Capsule #4

C-6 #27(20) / 1
#28(IN-625) / 3
#29(IN-825) / 4
#30(GAB1929) / 2

Capsule #4

D-1 —

E-1 —

F-1 #31(D441103) / 3
#33(BPV828) / 1
#34(K5-10) / 2
#35(S4) / 3

Capsule #4

D-2 —

E-2 —

F-2 #36(K12-8) / 4
#37(L-3) / 5
#38(S-3) / 1
#39(K15) / 1
#40(K2) / 0

Capsule #4

D-3 —

E-3 —

F-3 #41(C8) / 2
#42(R583) / 2
#43(C5) / 4

Capsule #4

D-4 —
D-5 —
D-6 —

E-4 —
E-5 —
E-6 —

F-4 1#24*fe
F-5 Fe dosimeter / 1
F-6

Red brick Updated May 15, 1994

[Yellow Brick]

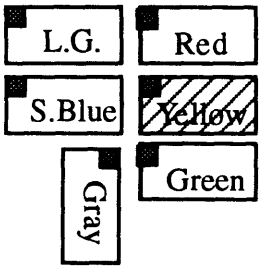

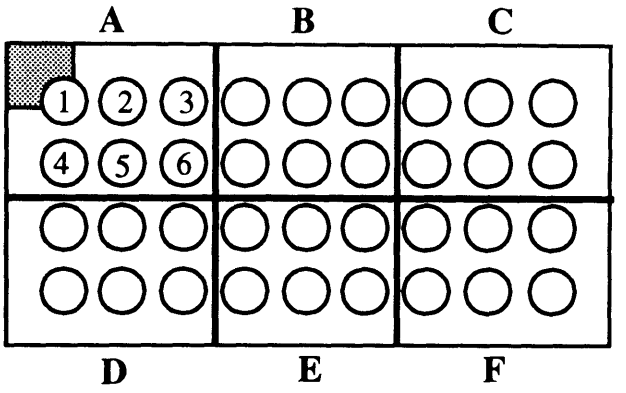

LEGEND

F-6 #10 (BPV605) / T-x-y
Location of storage hole *Material ID#* *Name of material* *# of TEM disks*

Capsule #7

A-1	#8(BPV603) / 3	B-1
A-2	#2S(V945Sens) / 5	B-2
A-3	#4(K12) / 4-4	B-3
A-4	#32(V946) / 2	B-4
A-5	#1S(AJ9139Sens) / 5	B-5
A-6	#3(K5) / 4-4	B-6

Capsule #5

C-1	#1S(AJ9139Sens) / 5
C-2	#2S(V945Sens) / 4 -1-1
C-3	#3(K5) / 3-2
C-4	#4(K12) / 5
C-5	#8(BPV603) / 1
C-6	

Capsule #4

D-1		E-1	#1(AJ9139) / 8-1-2-2
D-2		E-2	#2(V945) / 4-2
D-3		E-3	#3(K5) / 11-4
D-4		E-4	#4(K12) / 5-2-1
D-5		E-5	#8(BPV603) / 3-1-1
D-6		E-6	#32(V946) / 2

F-1
F-2
F-3
F-4
F-5
F-6

Updated May 15, 1994

[Sky Blue Brick]

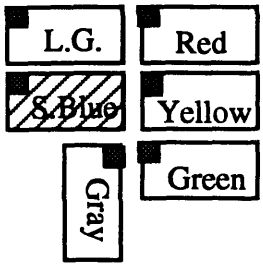

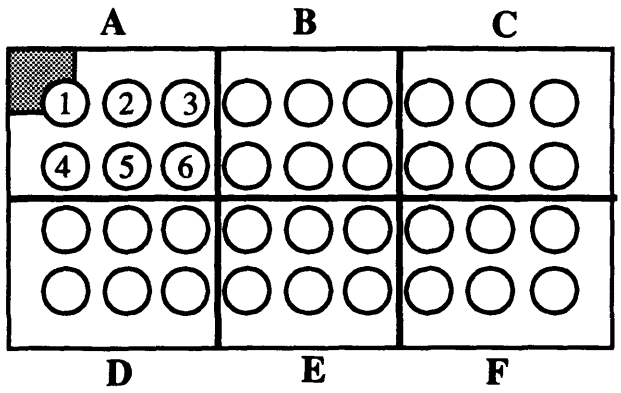

LEGEND

F-6 #10 (BPV605) / T-x-y
Location of storage hole *Material ID#* *Name of material* *# of TEM disks*

A-1 #23(15) / 3	B-1 #18(8N) / 4-1	C-1 #2(V945) / 9-4-1
A-2 #32(V946) / 6-4-2	B-2 #25(12) / 2	C-2 #31(D441103) / 4
A-3 #4(K12) / 5-3	B-3 #39(K15) / 3	C-3 #13(3N) / 4-1-2
A-4 #22(7) / 4	B-4 #28(IN-625) / 5	C-4 #5(BPV827) / 5
A-5 #10(BPV605) / 4-2	B-5 #30(GAB1929) / 4	C-5 #24(19) / 2
A-6 #21(NX10C1H) / 2	B-6 #8(BPV603) / 4-3-1	C-6 #38(S3) / 3-2
D-1 #26(18) / 3	E-1 #43(C5) / 1-1	F-1 #36(K12-8) / 1
D-2 #37(L-3) / 1	E-2 #1(AJ9139) / 6-4-1-1	F-2 #27(20) / 1
D-3 #29(IN-825) / 3	E-3 #9(BPV604) / 2-2	F-3 #3(K5) / 4-3-1
D-4 #19(6N) / 4-1-1-1	E-4 #42(R583) / 3	F-4 #12(2N) / 1-1
D-5 #35(S4) / 2	E-5 #6(GAB1928) / 3	F-5 #11(1N) / 1-1
D-6 #40(K2) / 4	E-6 #33(BPV828) / 4	F-6 #34(K5-10) / 2

All TEM Disks Came from Capsule #3

Updated May 15, 1994

[Green Brick]

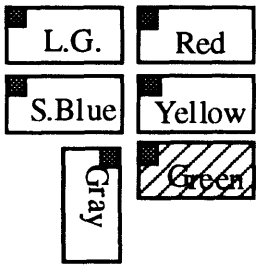

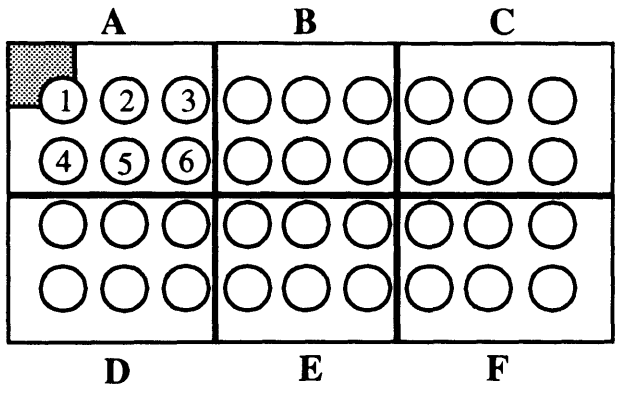

LEGEND

F-6 #10 (BPV605) / T-x-y
Location of storage hole *Material ID#* *Name of material* *# of TEM disks*

A-1	#16(N9) / 2	B-1	#30(GAB1929) / 3	C-1	#15(5N) / 3
A-2	#10(BPV605) / 4	B-2	#39(K15) / 3	C-2	#22(7) / 4
A-3	#11(1N) / 1	B-3	#29(IN-825) / 4	C-3	#2(V945) / 7
A-4	#4(K12) / 7 - 2	B-4	#3(K#5) / 8 -3	C-4	#20(10N) / 1
A-5	#35(S4) / 3	B-5	#9(BPV604) / 2	C-5	#1(AJ9139) / 5
A-6	#42(R583) / 2	B-6	#17(7N) / 4	C-6	#24(19) / 4
D-1	37(L-3) / 4	E-1	#19(N6) / 1	F-1	#26(18) / 1
D-2	#40(K2) / 2	E-2	#32(V946) / 4-3	F-2	#23(15) / 2(1Fe
D-3	#5(BPV827) / 4	E-3	#13(3N) / 3	F-3	#27(20) / 2
D-4	#18(8N) / 2	E-4	#28(IN-625) / 4	F-4	#41(C8) / 1
D-5	#43(C5) / 2	E-5	#38(S3) / 2	F-5	#36(K12-8) / 4
D-6	#8(BPV603) / 3	E-6	#31(D441103) / 1	F-6	#33(BPV828) / 1

All TEM Disks come from Capsule #1

Updated May 15, 1994

[Light Green Brick]

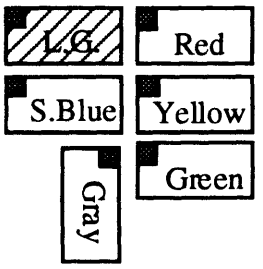

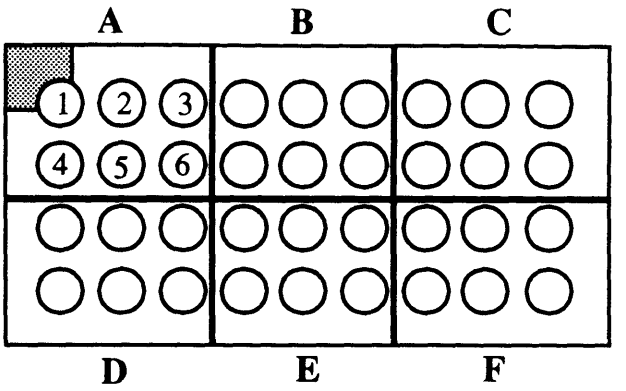

LEGEND

F-6 #10 (BPV605) / T-x-y

Location of storage hole *Material ID#* *Name of material* *# of TEM disks*

Capsule #5

A-1 —	B-1 —	C-1 #5(BPV827) / 6
		#9(BPV604) / 2
A-2 —	B-2 —	C-2 #11(1N) / 1
A-3 —	B-3 —	C-3 #15(5N) / 2-1
		#17(7N) / 2
		#18(8N) / 1
A-4 —	B-4 —	C-4 #20(10N) / 2-1
		#21(NX10C1H) / 1
		#22(7) / 2
A-5 —	B-5 —	C-5 #24(19) / 1
		#25(12) / 1
		#26(18) / 1
A-6 —	B-6 —	C-6 #30(GAB1929) / 2

Capsule #5

D-1 —	E-1 —	F-1 #33(BPV828) / 2
		#34(K5-10) / 1
		#35(S4) / 1
D-2 —	E-2 —	F-2 #38(L-3) / 1
		#39(K15) / 1
D-3 —	E-3 —	F-3 #40(K2) / 2
		#41(C8) / 2
		#42(R583) / 1
		#43(C5) / 1

D-4	——	E-4 ——	F-4
		Capsule #3	
D-5	——	E-5 #20(10N) / 1-1	F-5
D-6	——	E-6 #41(C8) / 1	F-6

Light Green Updated May 15, 1994

[Gray Brick]

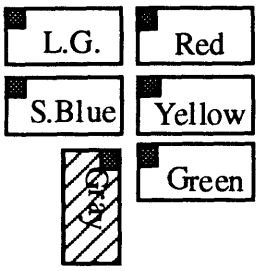

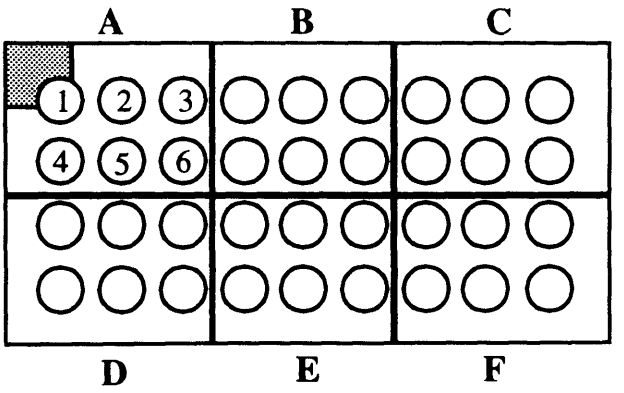

LEGEND

F-6 #10 (BPV605) / T-x-y
Location of storage hole *Material ID#* *Name of material* *# of TEM disks*

A-1	#X(B107) / 3 (1Fe?)	B-1	#G(B456) / 3	C-1	—
A-2	#B(B535) / 2	B-2	#C(B503) / 7	C-2	—
A-3	#D(B518) / 1	B-3	—	C-3	—
A-4	#L(B498) / 2	B-4	#H(B446) / 3(1Fe)	C-4	—
A-5	#P(B595) / 2	B-5	#O(B477) / 3	C-5	—
A-6	#S(13) / 1	B-6	—	C-6	—
D-1	Fe dosimeter / 1	E-1	#U(B067) / 4	F-1	—
D-2	#21(NX10C1H) / 2	E-2	#N(B553) / 3	F-2	—
D-3	#34(K5-10) / 1	E-3	—	F-3	—
D-4	#25(12) / 1	E-4	#A(B523) / 3	F-4	—
D-5	#R(B567) / 2	E-5	#M(B543) / 3	F-5	—
D-6	#K(B484) / 1	E-6	—	F-6	—

All TEM Disks come from Capsule #1

Updated May 15, 1994

TEM Samples from Capsule #1

Material	Number of Specimens Total	In Lead Bricks	
#1(AJ9139)	5	5(Green C-5)	
#2(V945)	7	7(Green C-3)	
#3(K5)	8	5(Green B-4)	*1 polished on 7/14 tube B, 2 pol. 8/11 tube B1 B2*
#4(K12)	7	5(Green A-4)	*1 polished on 7/14/93 tube C, 1 pol 8/11 tube C1*
#5(BPV827)	4	4(Green D-3)	
#6(GAB1928)	0		
#7			
#8(BPV603)	3	3(Green D-6)	
#9(BPV604)	2	2(Green B-5)	
#10(BPV605)	4	4(Green A-2)	
#11(1N)	1	1(Green A-3)	
#12(2N)	0		
#13(3N)	3	3(Green E-3)	
#14(4N)	0		
#15(5N)	3	3(Green C-1)	
#16(N9)	2	2(Green A-1)	
#17(7N)	4	4(Green B-6)	
#18(8N)	2	2(Green D-4)	
#19(N6)	1	1(Green E-1)	
#20(10N)	1	1(Green C-4)	
#21(NX10C1H)	1	1(Gray D-2)	

#22(7)	4	4(Green C-2)	
#23(15)	2(1Fe	2(Green F-2)	
#24(19)	4	4(Green C-6)	
#25(12)	1	1(Gray D-4)	
#26(18)	1	1(Green F-1)	
#27(20)	2	2(Green F-3)	
#28(IN-625)	4	4(Green E-4)	
#29(IN-825)	4	4(Green B-3)	
#30(GAB1929)	3	3(Green B-1)	
#31(D441103)	1	1(Green E-6)	
#32(V946)	4	1(Green E-2)	*3polished on 9/21/9393 tubes G1 G2 G3*
#33(BPV828)	1	1(Green F-6)	
#34(K5-10)	1	1(Gray D-3)	
#35(S4)	3	3(Green A-5)	
#36(K12-8)	4	4(Green F-6)	
#37(L-3)	4	4(Green D-1)	
#38(S3)	2	2(Green E-5)	
#39(K15)	3	3(Green B-2)	
#40(K2)	2	2(Green D-2)	
#41(C8)	1	1(Green F-4)	
#42(R583)	2	2(Green A-6)	
#43(C5)	2	2(Green D-5)	
#A(B523)	3	3(Gray E-4)	
#B(B535)	2	2(Gray A-2)	
#C(B503)	7	7(Gray B-2)	

TEM Samples from Capsule #1(page 3/3)

#D(B518)	1	1(Gray A-3)
#G(B456)	3	3(Gray B-1)
#H(B446)	3(1Fe	3(Gray B-4)
#K(B484)	1	1(Gray D-6)
#L(B498)	2	2(Gray A-4)
#M(B543)	3	3(Gray E-5)
#N(B553)	3	3(Gray E-2)
#O(B477)	3	3(Gray B-5)
#P(B595)	2	2(Gray A-5)
#R(B567)	2	2(Gray D-4)
#S(13)	1	1(Gray A-6)
#T(117)	0	
#U(B067)	4	4(Gray E-1)
#X(B107)	3	3(Gray A-1)
Fe dosimeter	1	1(Gray D-1)

TEM Samples from Capsule #1: Updated May 15, 1994

TEM Samples from Capsule #3

Material	Number of Specimens Total	In Lead Bricks	Temporary Storage Hole	EPR Storage	Jet polishing
#1(AJ9139)	6	0(Sky Blue E-2)		5	*1 pol 10/14/93 tube H1*
#2(V945)	9	4(Sky Blue C-1)		5	
#3(K5)	4	0(Sky Blue F-3)		4	
#4(K12)	5	2(Sky Blue A-3)		3	
#5(BPV827)	5	5(Sky Blue C-4)			
#6(GAB1928)	3	3(Sky Blue E-5)			
#7					
#8(BPV603)	4	0(Sky Blue B-6)		3	*pol 8/24 tube D1*
#9(BPV604)	2	0(Sky Blue E-3)		2	
#10(BPV605)	5	3(Sky Blue A-5)		2	
#11(1N)	1	0(Sky Blue F-5)		1	
#12(2N)	1	0(Sky Blue F-4)			*pol 8/24 tube E1*
#13(3N)	4	1(Sky Blue C-3)		1(Not Tested)	*2 pol 8/24 tube F1,F2*
#14(4N)	0				
#15(5N)	0				
#16(N9)	0				
#17(7N)	0				
#18(8N)	3	2(Sky Blue B-1)		1	
#19(N6)	4	1(Sky Blue D-4)		1 CF	*1 pol on 1/27/94 1 pol on 3/10/94*
#20(10N)	1	0(L.Green E-5)		1 CF	
#21(NX10C1H)	2	2(Sky Blue A-6)			

TEM Samples from Capsule #3 (page 2/3)

#22(7)	4	4(Sky Blue A-4)		
#23(15)	3	3(Sky Blue A-1)		
#24(19)	2	2(Sky Blue C-5)		
#25(12)	2	2(Sky Blue B-2)		
#26(18)	3	3(Sky Blue D-1)		
#27(20)	1	1(Sky Blue F-2)		
#28(IN-625)	5	5(Sky Blue B-4)		
#29(IN-825)	3	3(Sky Blue D-3)		
#30(GAB1929)	4	4(Sky Blue B-5)		
#31(D441103)	4	4(Sky Blue C-2)		
#32(V946)	6	0(Sky Blue A-2)	4	*2 polished on 9/21/9393 tubes G4 G5*
#33(BPV828)	4	4(Sky Blue E-6)		
#34(K5-10)	2	2(Sky Blue F-6)		
#35(S4)	2	2(Sky Blue D-5)		
#36(K12-8)	1	1(Sky Blue F-1)		
#37(L-3)	1	1(Sky Blue D-2)		
#38(S3)	3	1(Sky Blue C-6)	2	
#39(K15)	3	3(Sky Blue B-3)		
#40(K2)	4	4(Sky Blue D-6)		
#41(C8)	1	1(L.Green E-6)		
#42(R583)	3	3(Sky Blue E-4)		
#43(C5)	1	0(Sky Blue E-1)	1	
#A(B523)	2	2		
#B(B535)	3	3		
#C(B503)	2	2		

TEM Samples from Capsule #3 (page 3/3)

#D(B518)	3	3
#G(B456)	4	4
#H(B446)	1	1
#K(B484)	2	2
#L(B498)	2	2
#M(B543)	2	2
#N(B553)	3	3
#O(B477)	1	1
#P(B595)	1	1
#R(B567)	5	5
#S(13)	4	4
#T(117)	5	5
#U(B067)	1	1
#X(B107)	1	1

TEM Samples from Capsule #3: Updated May 15, 1994

TEM Samples from Capsule #4

Material	Number of Specimens		
	Total	In Lead Bricks	Jet polishing
#1(AJ9139)	8	3(Yellow E-1)	*1 jet pol on 3/17/94 (H2) 1 jet pol on 3/30/94 1 jet pol on 4/0694 1 jet pol on 4/12/94 1 jet pol on 4/24/94*
#2(V945)	4	2(Yellow E-2)	*2 jet pol on 05/3/94*
#3(K5)	11	7(Yellow E-3)	*1 jet pol on 10/29 1 jet pol on 11/3 1 jet pol on 11/4 1 jet pol on 3/2/94*
#4(K12)	5	2(Yellow E-4)	*1 jet pol on 1/12/94 1 jet pol on 1/18/94 1 jet pol on 4/0694*
#5(BPV827)	8	8(Red C-1)	
#6(GAB1928)	1	1(Red C-1)	
#8(BPV603)	3	1(Yellow E-5)	*1 jet pol on 2/09/94 1 jet pol on 2/17/94*
#9(BPV604)	2	2(Red C-1)	
#10(BPV605)	2	2(Red C-1)	
#11(1N)	2	0(Red C-2)	*1 jet pol on 3/2/94 1 jet pol on 3/30/94*
#12(2N)	3	3(Red C-2)	
#13(3N)	1	1(Red C-2)	
#14(4N)	2	2(Red C-2)	
#15(5N)	3	1(Red C-3)	*1 jet pol on 4/12/94 1 jet pol on 5/03/94*
#16(N9)	3	0(Red C-3)	1 for EPR CF *1 jet pol on 1/18/94 1 jet pol on 5/3/94*
#17(7N)	2	2(Red C-3)	
#18(8N)	2	2(Red C-3)	
#19(N6)	0		
#20(10N)	2	1(Red C-4)	*1 jet polished on 11/10/93*
#21(NX10C1H)	3	3(Red C-4)	

TEM Samples from Capsule #4 (page 2/3)

#22(7)	0	
#23(15)	0	
#24(19)	2	2(Red C-5)
#25(12)	1	1(Red C-5)
#26(18)	1	1(Red C-5)
#27(20)	1	1(Red C-6)
#28(IN-625)	3	3(Red C-6)
#29(IN-825)	4	4(Red C-6)
#30(GAB1929)	2	2(Red C-6)
#31(D441103)	3	3(Red F-1)
#32(V946)	2	2(Yellow E-6)
#33(BPV828)	1	1(Red F-1)
#34(K5-10)	2	2(Red F-1)
#35(S4)	3	3(Red F-1)
#36(K12-8)	4	4(Red F-2)
#37(L-3)	5	5(Red F-2)
#38(S-3)	1	1(Red F-2)
#39(K15)	1	1(Red F-2)
#40(K2)	0	
#41(C8)	2	2(Red F-3)
#42(R583)	2	2(Red F-3)
#43(C5)	4	4(Red F-3)
#A(B523)	Not counted (in temporary storage hole #4)	
#B(B535)	Not counted (in temporary storage hole #4)	
#C(B503)	Not counted (in temporary storage hole #4)	

TEM Samples from Capsule #4(page 3/3)

#D(B518)	Not counted (in temporary storage hole #4)
#G(B456)	Not counted (in temporary storage hole #4)
#H(B446)	Not counted (in temporary storage hole #4)
#K(B484)	Not counted (in temporary storage hole #4)
#L(B498)	Not counted (in temporary storage hole #4)
#M(B543)	Not counted (in temporary storage hole #4)
#N(B553)	Not counted (in temporary storage hole #4)
#O(B477)	Not counted (in temporary storage hole #4)
#P(B595)	Not counted (in temporary storage hole #4)
#R(B567)	Not counted (in temporary storage hole #4)
#S(13)	Not counted (in temporary storage hole #4)
#T(117)	Not counted (in temporary storage hole #4)
#U(B067)	Not counted (in temporary storage hole #4)
#X(B107)	Not counted (in temporary storage hole #4)
Fe dosimeter	1 in Red F5

TEM Samples from Capsule #4: Updated May 15, 1994

TEM Samples from Capsule #5

Material	Number of Specimens		
	Total	In Lead Bricks	Jet polishing
#1S(AJ9139Sens)	5	5(Yellow C-1)	
#2S(V945Sens)	4	2(Yellow C-2)	*1 jet pol on 12/2/93 1 jet pol on 12/9/93*
#3(K5)	3	1(Yellow C-3)	*2 jet pol on 11/18/93*
#4(K12)	5	5(Yellow C-4)	
#5(BPV827)	6	6(Light Green C-1)	
#6(GAB1928)			
#8(BPV603)	1	1(Yellow C-5)	
#9(BPV604)	2	2(Light Green C-1)	
#10(BPV605)	0		
#11(1N)	1	1(Light Green C-2)	
#12(2N)	0		
#13(3N)	0		
#14(4N)	0		
#15(5N)	2	1(Light Green C-3)	*1 jet pol on 2/17/94*
#16(N9)	0		
#17(7N)	2	2(Light Green C-3)	
#18(8N)	1	1(Light Green C-3)	
#19(N6)	0		
#20(10N)	2	1(Light Green C-4)	*1 jet pol on 2/09/94*
#21(NX10C1H)	1	1(Light Green C-4)	

TEM Samples from Capsule #5 (page 2/3)

#22(7)	2	2(Light Green C-4)
#23(15)	0	
#24(19)	1	1(Light Green C-5)
#25(12)	1	1(Light Green C-5)
#26(18)	1	1(Light Green C-5)
#27(20)	0	
#28(IN-625)	0	
#29(IN-825)	0	
#30(GAB1929)	2	2(Light Green C-6)
#31(D441103)	0	
#32(V946)	0	
#33(BPV828)	2	2(Light Green F-1)
#34(K5-10)	1	1(Light Green F-1)
#35(S4)	1	1(Light Green F-1)
#36(K12-8)	0	
#37(L-3)	0	
#38(L-3)	1	1(Light Green F-2)
#39(K15)	1	1(Light Green F-2)
#40(K2)	2	2(Light Green F-3)
#41(C8)	2	2(Light Green F-3)
#42(R583)	1	1(Light Green F-3)
#43(C5)	1	1(Light Green F-3)
#A(B523)	Not counted (in temporary storage hole #5)	
#B(B535)	Not counted (in temporary storage hole #5	
#C(B503)	Not counted (in temporary storage hole #5)	

#D(B518)	Not counted (in temporary storage hole #5)
#G(B456)	Not counted (in temporary storage hole #5)
#H(B446)	Not counted (in temporary storage hole #5)
#K(B484)	Not counted (in temporary storage hole #5)
#L(B498)	Not counted (in temporary storage hole #5)
#M(B543)	Not counted (in temporary storage hole #5)
#N(B553)	Not counted (in temporary storage hole #5)
#O(B477)	Not counted (in temporary storage hole #5)
#P(B595)	Not counted (in temporary storage hole #5)
#R(B567)	Not counted (in temporary storage hole #5)
#S(13)	Not counted (in temporary storage hole #5)
#T(117)	Not counted (in temporary storage hole #5)
#U(B067)	Not counted (in temporary storage hole #5)
#X(B107)	Not counted (in temporary storage hole #5)

UNIDENTIFIED TEMS IN TEMPORARY STORAGE HOLE #2

TEM Samples from Capsule #5: Updated May 15, 1994

TEM Samples from Capsule #7

Material	Number of Specimens			
	Total	In Lead Bricks	Temporary Storage Hole	EPR Specimen Storage
#1S(AJ9139Sens)	5	5(Yellow A-5)		
#2S(V945Sens)	5	5(Yellow A-2)		
#3(K5)	4	0(Yellow A-6)		4(of 2 Not Tested)
#4(K12)	4	0(Yellow A-3)		4
#5(BPV827)	4	3(Red B-3)		*1 jet polished on 6/25/93 tube A*
#6(GAB1928)	0			
#7				
#8(BPV603)	3	3(Yellow A-1)		
#9(BPV604)	3	3(Red A-1)		
#10(BPV605)	1	1(Red A-1)		
#11(1N)	2	2(Red A-1)		
#12(2N)	5	5(Red A-1)		
#13(3N)	1	1(Red A-2)		
#14(4N)	1	1(Red A-2)		
#15(5N)	1	1(Red A-2)		
#16(N9)	1	1(Red A-2)		
#17(7N)	2	2(Red A-3)		
#18(8N)	2	2(Red A-3)		
#19(N6)	2	2(Red A-3)		
#20(10N)	3	3(Red A-3)		
#21(NX10C1H)	2	2(Red A-4)		

TEM Samples from Capsule #7 (page 2)

#22(7)	1	1(Red A-4)
#23(15)	2	2(Red A-4)
#24(19)	1	1(Red A-4)
#25(12)	1	1(Red A-5)
#26(18)	3	3(Red A-5)
#27(20)	0	
#28(IN-625)	1	1(Red A-5)
#29(IN-825)	1	1(Red A-5)
#30(GAB1929)	1	1(Red A-6)
#31(D441103)	1	1(Red A-6)
#32(V946)	2	2(Yellow A-4)
#33(BPV828)	3	3(Red A-6)
#34(K5-10)	3	3(Red B-1)
#35(S4)	1	1(Red B-1)
#36(K12-8)	0	
#37(L-3)	0	
#38(S3)	1	1(Red B-1)
#39(K15)	1	1(Red B-1)
#40(K2)	2	2(Red B-2)
#41(C8)	3	3(Red B-2)
#42(R583)	2	2(Red B-2)
#43(C5)	2	2(Red B-2)
#A(B523)	Not Counted, in temporary storage hole #6, in temporary storage hole #6	
#B(B535)	Not Counted, in temporary storage hole #6	
#C(B503)	Not Counted, in temporary storage hole #6	

TEM Samples from Capsule #7 (page 3)

#D(B518)	Not Counted, in temporary storage hole #6
#G(B456)	Not Counted, in temporary storage hole #6
#H(B446)	Not Counted, in temporary storage hole #6
#K(B484)	Not Counted, in temporary storage hole #6
#L(B498)	Not Counted, in temporary storage hole #6
#M(B543)	Not Counted, in temporary storage hole #6
#N(B553)	Not Counted, in temporary storage hole #6
#O(B477)	Not Counted, in temporary storage hole #6
#P(B595)	Not Counted, in temporary storage hole #6
#R(B567)	Not Counted, in temporary storage hole #6
#S(13)	Not Counted, in temporary storage hole #6
#T(117)	Not Counted, in temporary storage hole #6
#U(B067)	Not Counted, in temporary storage hole #6
#X(B107)	Not Counted, in temporary storage hole #6

TEM Samples from Capsule #7: Updated May 15, 1994